Technische Universität München
TUM School of Natural Sciences

Gas Phase Studies of the Reactivity of Small Molecules on Tantalum(-Oxide) and Platinum(-Oxide) Clusters

Flora Siegele

Vollständiger Abdruck der von der TUM School of Natural Sciences der Technischen Universität München zur Erlangung einer

Doktorin der Naturwissenschaften (Dr. rer. nat.)

genehmigten Dissertation.

Vorsitz: Prof. Dr. Dominik Bucher

Prüfende der Dissertation:

1. Priv.-Doz. Dr. Martin Tschurl
2. Prof. Dr. Jennifer Strunk

Die Dissertation wurde am 16.09.2025 bei der Technischen Universität München eingereicht und durch die TUM School of Natural Sciences am 22.10.2025 angenommen.

Abstract

The activation of small molecules such as methane and ammonia is a challenging goal with the underlying reaction mechanisms and knowledge about the active sites on catalysts often unknown. This work aims to demonstrate the strength of model systems, such as gas phase reactivity studies, for identifying important reaction parameters. In the presented studies, clusters are generated using a laser vaporization cluster source and are analyzed either directly ($Pt_x^{+/-}$ studies) or after mass selection in a quadrupole mass filter and their reaction in a ring electrode ion trap (Ta_x^+ studies). Identification of the species present is carried out using a time-of-flight mass spectrometer. For the system [$Ta_2O_x^+$], DFT calculations are performed to facilitate the kinetic and mechanistic discussion of the experimental data. Literature results already show that tantalum(-oxide) clusters have a great potential in the activation of small molecules like CH_4, NH_3, and N_2. However, the underlying reaction mechanism is strongly dependent on the cluster size and the oxidation state. For methane, possible reaction mechanisms include the adsorption of molecular methane and its dehydrogenation, which results in the addition of a CH_2 moiety to the cluster. For ammonia, the activation of the molecule can also result in a dehydrogenation reaction, leading to the formation of imines. Nitrogen is only activated by small tantalum clusters, while clusters consisting of more than five tantalum atoms only enable molecular adsorption. Different possible reaction mechanisms are also observed when changing the oxidation state of Ta_2^+. As shown in this work, the bare metal cluster and the low oxidized species $Ta_2O_2^+$ enable the dehydrogenation of methane, while higher oxidized clusters only enable molecular adsorption. An exception is $Ta_2O_5^+$, on which a HAT reaction is observed. This is, aided by DFT calculations, attributed to the high spin density on oxygen in $Ta_2O_5^+$. DFT studies further identify the formation of CH_2 bridges as a source for energy gains and thus a possible driving force. Finally, first studies using platinum show the possibility to investigate cationic and anionic clusters in the same system by reversing the voltages of the einzel lenses and the extraction stage. Moreover, experiments performed at room temperature reveal the addition of ammonia to the platinum cation, which is a first step toward exploring relevant properties of platinum in ammonia slip catalysis.

Zusammenfassung

Die Aktivierung kleiner Moleküle wie Methan und Ammoniak stellen eine große Herausforderung dar, weil häufig weder zu Grunde liegende Mechansimen, noch das aktive Zentrum des Katalysators genauer bekannt sind. Ziel dieser Arbeit ist es, die Stärke von Modellsystemen, wie z.B. Gasphasensysteme, zur Untersuchung und Aufklärung dieser Schlüsselinformationen zu zeigen. Dafür werden Metallcluster in einer Laserverdampfungsquelle erzeugt und entweder direkt in einem Flugzeitmassenspektrometer analysiert ($Pt_x^{+/-}$) oder aber in einem Quadrupolmassenfilter größenselektiert und in einer Ringelektrodenionenfalle zur Reaktion gebracht (Ta_x^+). Die entstehenden Produkte werden ebenfalls in einem Flugzeitmassenspektrometer bestimmt. Um die experimentellen Daten in Hinblick auf kinetische und mechanistische Fragestellungen besser disktutieren zu können, werden DFT Berechnungen für das System [$Ta_2O_x^+$] durchgeführt. Unterschiedlichste Studien zeigen bereits das große Potential von Tantal(-oxid)clustern in der Aktivierung kleiner Moleküle (CH_4, NH_3 und N_2). Der Rekationsmechanismus ist stark von der Clustergröße und dem Oxidationszustand abhängig. Methan kann entweder molekular adsorbieren oder aktiviert werden, wobei CH_2 an den Cluster bindet und H_2 freigesetzt wird. Bei der Aktivierung von Ammoniak kommt es unter Wasserstoffabspaltung zur Iminbildung. Wenn Stickstoff mit Tantalclustern interagiert, spielt die Clustergröße eine wichtige Rolle. Die N≡N Dreifachbindung kann nur von kleinen Clustern aktiviert werden, an Clustern mit mehr als fünf Atomen findet molekulare Adsorption statt. Für das System [$Ta_2O_x^+$] wurden abhängig vom Oxidationsgrad unterschiedliche Reaktivitäten beobachtet. Hier wird gezeigt, dass für metalisches Ta_2^+ und schwach oxidiertes $Ta_2O_2^+$ eine Dehydrierung von Methan via Metallinsertion stattfindet. Bei stärker oxidierten Verbindungen wird molekulare Adsorption beobachtet. Eine Ausnahme ist $Ta_2O_5^+$, bei dem es zum Transfer eines Wasserstoffatoms kommt. Mittels DFT Rechnungen konnte die Bildung von CH_2-Brücken als mögliche Triebkraft der Dehydrierung auf $Ta_2O_2^+$ identifiziert werden, während für den Transfer eines Wasserstoffatoms die hohe Spindichte auf Sauerstoff an $Ta_2O_5^+$ ausschlaggebend ist. Zuletzt wurde mit ersten Experimenten gezeigt, dass sich das vorliegende System eignet, Platinkationen sowie -anionen zu untersuchen. Für den Wechsel muss die Polarität der Einzellinsenspannungen und die der Extraktionsplatten geändert werden. Außerdem scheint Platin ein vielversprechender Kanditat für die Aktivierung von Ammoniak zu sein, da eine Interaktion zwischen dem Kation und Ammoniak bei Raumtemperatur beobachtet werden konnte.

Contents

1 Introduction **1**

2 Theoretical Background **3**

2.1 Why Gas Phase Studies? 3

2.2 Conditions 4

2.3 Reactivity Studies 5

2.4 Spectroscopic Measurements 6

2.5 Theoretical Modeling 8

3 Experimental **11**

3.1 Experimental Setup 11

3.1.1 Cluster Source 12

3.1.2 Ion Guides, Quadrupole Bender, and Quadrupole Mass Filter . 13

3.1.3 Ring Electrode Ion Trap 14

3.1.4 Reflectron Time of Flight Mass Spectrometer 15

3.1.5 Additions and Changes to the Setup 17

3.2 Data Evaluation 22

3.3 Computational Methods 25

4 Activation of CH_4, NH_3, and N_2 by Tantalum Ions, Clusters and Their Oxides: What Can Be Learnt from Studies of Ions in the Gas Phase [14] **26**

4.1 Reactivity with Methane 26

4.2 Reactivity with Ammonia 29

4.3 Reactivity with Nitrogen 32

5 Reactivity of $Ta_2O_x^+$ ($0 \leq x \leq 6$) Clusters with Methane [15] **34**

5.1 Methane Dehydrogenation on $Ta_2O_2^+$ 36

5.2 The Unique Reactivity of $Ta_2O_5^+$ toward Methane 48

5.3 Origins of Reactivity 52

6 Studies of Platinum Clusters **55**

6.1 Switching from Cations to Anions and Vice Versa 55

6.2 Pt_x^+ Clusters in the Linear ToF 57

6.3 Initial Operation of the New MCP Detector 60

6.4 Calibration of the Linear ToF-MS 62

6.5 Platinum Cations and Their Interaction with NH_3 65

7 Conclusion and Outlook **71**

Nomenclature

$(re-)ToF-MS$ (reflectron-)time-of-flight mass spectrometer

BNC bayonet Neill Concelman

CCD charge coupled device

DC direct current

DFT density functional theory

GS ground state

HAT hydrogen atom transfer

HV high voltage

IR infrared

LRZ Leibniz-Rechenzentrum

$m-GGA$ meta generalized gradient

MCP microchannel plate

$PCET$ proton-coupled electron transfer

PES potential energy surface

QMF quadrupole mass filter

$REIT$ ring electrode ion trap

RF radio frequency

RIJ resolution of identity approximation

SHV safe high voltage

$TIED$ trapped ion electron diffraction

TS transition state

List of Figures

1 Overview of the three abstraction regimes in heterogeneous catalysis. 3
2 TIED results exemplary shown for Pt_6^-. 7
3 Principles of IR depletion/dissociation spectroscopy. 8
4 Potential energy surface determined via DFT exemplary shown for the transformation of ozone into isoozone. 10
5 Overview over the used apparatus. 11
6 Overview of the used laser vaporization cluster source. 12
7 Overview over the re-ToF-MS setup. 16
8 CAD drawing of the new *Faraday* cup. 18
9 Overview over possible working principles of MCP detectors. 19
10 CAD drawing of the MCP mounting. 20
11 Circuit diagram of the installed z-stack MCP detector. 21
12 Schematic of the trigger pulses used for the extraction of anionic and cationic clusters, respectively. 22
13 Broadband spectrum of Ta_4^+ – Ta_{10}^+ clusters and their oxides, used for the scale conversion from time of flight to m/z units. 23
14 Re-ToF mass spectra for different storage times in the REIT for $Ta_2O_2^+$ and $Ta_2O_5^+$, respectively, and the associated kinetic fits of the reaction progresses. 24
15 Summary of possible interaction pathways of methane with metal(-oxide) clusters. 27
16 Activation mechanism of methane on Ta^+. 28
17 Possible interactions of NH_3 with metal cations. 30
18 Possible pathways in the reaction of NH_3 with tantalum clusters. 31
19 Possible interactions of tantalum clusters with N_2. 33
20 Mass spectra of the products in the reaction of $Ta_2O_x^+$ with CH_4. 35
21 Kinetic fits obtained for $Ta_2O_2^+$ + CH_4 and the respective reaction mechanism. 37
22 Structure of transition states of hypothetical methane dehydrogenation reactions after molecular methane adsorption. 39
23 a) Alternative tested reaction mechanism for $Ta_2O_2^+$ + CH_4. 40
24 Overview over the *Gibbs* free energies during the course of the first dehydrogenation of CH_4 on $Ta_2O_2^+$. 41

25 Overview over the *Gibbs* free energies during the transformation of $Ta_2O_2(CH_2)^+$ into a more stable isomer. 42
26 Overview over *Gibbs* free energies in the dehydrogenation of CH_4 on $Ta_2O_2(CH_2)^+$. 43
27 Comparison of the present normalized *Gibbs* free energies in the first and second dehydrogenation reaction of methane. 44
28 Examples of tested candidate structures exhibiting C−C bond formation. 45
29 Overview of *Gibbs* free energies for all adsorption reactions on species present in the reaction network $Ta_2O_2^+$ + CH_4. 45
30 Comparison of the mass spectra recorded after the interaction of $Ta_2O_2^+$ with CH_4 and CD_4. 46
31 Kinetic fits obtained for $Ta_2O_5^+$ + CH_4 and the respective reaction mechanism. 49
32 Mass spectrum recorded for the reaction of $Ta_2O_5^+$ with CD_4. 50
33 Overview over the *Gibbs* free energies during the reaction of $Ta_2O_5^+$ with two methane molecules. 51
34 Comparison of the spin densities of $Ta_2O_2^+$ and $Ta_2O_5^+$. 53
35 Change of the spin density of $Ta_2O_5^+$ during the reaction with two methane molecules. 54
36 Cluster current for anionic and cationic clusters measured on the *Faraday* cup. 56
37 Determination of the kinetic energies of anionic clusters present. . . . 56
38 ToF mass spectra of cationic platinum clusters after the ion trap. 58
39 ToF mass spectra of Pt_{40}^+ after the interaction with NH_3 in the ion trap. . 59
40 Comparison of the single-particle signals recorded at different amplification voltages in the MCP detector. 62
41 Calibration of the new ToF-MS using Ag^+ clusters. 63
42 Mass spectrum showing the peaks of Ag_1^+ - Ag_5^+ with its isotopes. . . . 64
43 Mass spectra of oxidized Ag^+ clusters. 65
44 Mass spectrum of Pt_1^+ - Pt_{25}^+ recorded directly after the cluster source. . 66
45 Detectable cluster size in dependence to the ToF-MS extraction timing. 67
46 Mass spectra showing the removal of carbon contamination on the platinum target. 68
47 Mass spectra of the interaction of Pt_1^+ - Pt_3 with NH_3. 69
48 Mass spectrum of anionic platinum clusters. 70

List of Tables

1 Determined rate coefficients and literature values for the interaction of $Ta_2O_n^+$ with CH_4. 36
2 Rate coefficients for $Ta_2O_2^+$ + CH_4/CD_4. 38
3 Rate coefficients and the respective KIEs for the first two dehydrogenation reactions of CH_4/CD_4 on $Ta_2O_2^+$. 47
4 Rate coefficients for possible HATs from CH_4/CD_4 to $Ta_2O_5^+$ and the respective KIEs. 49
5 Comparison of anionic and cationic clusters produced under the same conditions. 57

1 Introduction

With the concern of climate change being more topical now than ever, preventing the emission of green house gases is the focus of various approaches in science and technology. Methane is a prominent representative of these gases. Due to its high stability caused by intrinsic molecular properties like the strong sp^3-hybridization of the C-H bonds, the small pK_a-value and the small polarizability, a conversion of methane to higher-valued chemicals is very challenging [1]. Presently, this is usually achieved indirectly by partial oxidation of CH_4 to syngas, which is then converted into the chemical of choice (e.g., hydrocarbons or alcohols) [2, 3]. While this indirect conversion of methane is energy- and cost-inefficient, another disadvantage is the release of CO_2 as a side product in the steam reforming process [4]. Research is therefore attempting to find reaction pathways in which methane can be converted directly in an economically competitive manner. One possibility is to pursue a trial-and-error approach, while another strategy is based on a fundamental understanding of the catalyst. The aim of this knowledge-based approach is to understand the reaction system so well that the chosen catalyst can be specifically tuned to achieve the desired reactivity and selectivity. Highly abstracted model systems can thereby help to gain such a fundamental understanding. One example of such an approach is the investigation of the reaction of isolated clusters in the gas phase, which allows the intrinsic reaction properties of possible catalytic materials to be elucidated in the absence of a support. This type of model system was previously used by *Eckhard* et al. to get a deeper insight into the activation and dehydrogenation of methane on $[Ta_xO]^+$ (x = 4,5) [5] and into the cluster size dependencies of the reactivity toward methane on $[Ta_x^+]$ ($1 \leq$ x $\leq$ 10) [6]. Furthermore, *Levin* et al. showed the possibility of a subsequent C-C coupling on the activated methane molecule on $[Ta_8O_2^+]$ [7]. On the one hand, this activation of methane and a subsequent formation of e.g., methanol could open new pathways in synthesis of value-added chemicals from methane. On the other hand, the elucidation of reaction mechanisms together with relevant structural and electronic properties of the clusters in the activation of methane can help developing and improving catalysts for C$-$H bond activation.

Another approach toward preventing the emission of green house gases is the introduction of alternative, carbon free fuels. NH_3 could thereby play an important role in the future. While the reaction products nitrogen and hydrogen are harmless, the main problem when using ammonia besides a possible overoxidation to NO_x gases,

is its toxicity. Therefore, it has to be ensured that ammonia does not leave the system in significant amounts, which is why a catalyst with high conversion rates has to be used. *Marchuk* et al. studied the desired selective ammonia oxidation on platinum based catalysts, showing the great potential of platinum for the activation of NH_3 [8, 9]. In these rather complex systems, platinum is deposited on alumina- and zeolite supports. There, a multitude of parameters is unknown, such as e.g., the exact size of the platinum particles, their distribution within the coating, their geometry and changes during the course of the reactions. This makes it difficult to perform a detailed investigation of the underlying reaction mechanism, even when highly-demanding operando methods are applied [10]. On cluster model systems, however, mainly theoretical studies by *Daramola* and *Botte* [11, 12] investigating the adsorption mechanisms exist. Additionally, *Koszinowski* et al. showed the release of molecular hydrogen from NH_3 on the platinum cation under single-collision conditions [13].

This thesis deals with both aspects. First, current research findings on the activation of small molecules on the conversion of methane and ammonia on tantalum(-oxide) clusters are discussed. The aim is to show which kind of information can be gained from gas phase studies, to compare results, and highlight similarities, trends, and differences in the reactivity on various investigated systems. Secondly, this is followed by the investigation of reactivity trends in dependence of the oxidation state on $Ta_2O_x^+$ clusters ($0 \leq x \leq 6$). Measurements performed by *Jan F. Eckhard* are re-evaluated and complemented by DFT calculations within this work. Experiments are performed using CH_4 and the isotopically labled gas CD_4, allowing for the determination of underlying reaction mechanisms and the identification of the respective driving forces. As a last project, cationic and anionic platinum clusters are characterized and their interaction with NH_3 is investigated in preliminary reactivity studies.

As a result, this thesis is structured as follows. After the introduction of a theoretical background, required for the evaluation and discussion of the obtained data, the experimental setup and used methods are presented. This is followed by a section about changes that have been made to the setup during the course of this dissertation, including the installation of new components such as a Faraday cup and a new MCP detector. Subsequently, a literature review on the activation of CH_4, NH_3, and N_2 on tantalum(-oxide) clusters is given, which has also been published by us [14]. Finally, the data on $Ta_2O_x^+$ clusters, issued in a corresponding article [15], and the generation and reaction of $Pt_x^\pm$ clusters with ammonia is evaluated and interpreted.

2 Theoretical Background

2.1 Why Gas Phase Studies?

In industry, reactions are usually catalyzed using heterogeneous catalysts [16, 17]. Here, the catalyst is in a different phase than the reactants, whereby the best-known examples involve a solid catalyst and either gaseous or liquid reactants [17]. This makes it easier to separate the product species from the catalyst, which simplifies its recovery and reuse, resulting in a more cost-efficient and environmentally friendly process compared to homogeneously catalyzed processes. However, heterogeneous catalysis also has significant disadvantages. Deactivation and poisoning of the catalyst by chemical impurities, thermal instability, or the reaction with by-products, as well as mass transfer limitations due to diffusion barriers and an inefficient product removal, play an important role in the interaction with the catalyst [18]. The main problem is the lack of knowledge about the active site. Without this expertise, studies elucidating the underlying reaction mechanism are hardly possible and a targeted catalyst design for e.g., high reactivity and selectivity is difficult to achieve [19]. One step toward elucidating the active sites is to characterize model systems and then gradually increase the complexity of the system in order to "track" the active sites through different abstraction gaps and size regimes.

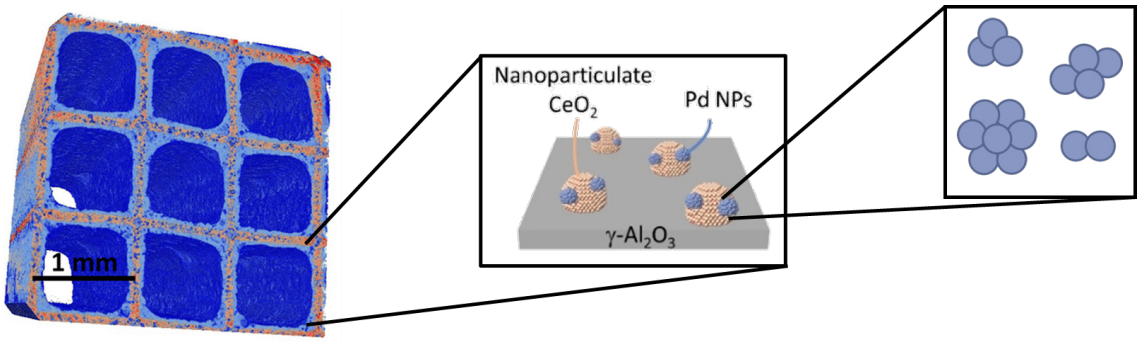

Figure 1: The three typical size regimes of heterogeneous catalysts. The applied catalyst (left) often consists of a honeycomb-structured support (red lines) covered in a reactive catalyst coating (blue). It features a porous catalysts of defined sizes (e.g., Pd nanoparticles) on support oxides with oriented surfaces (middle). Lastly, the system comprises individual nanoparticles as the actual catalytic material (right). Taken and modified from [20, 21]. Used with permission of *John Wiley & Sons - Books* from [21]; permission conveyed through *Copyright Clearance Center, Inc*.

A heterogeneous, industrial catalyst can typically be considered on three different size scales (compare Figure 1). Looking at the big picture, a realistic catalytic system involves hierarchically structured catalysts at reactor level. These usually consist of a honeycomb-structured support covered in a reactive catalyst coating. Selectivity and reactivity influences of different coatings, honeycomb geometries and reaction conditions as well as catalyst poisoning and deactivation processes are typically studied under applied conditions. In addition, this system can be abstracted in order to get a better understanding of underlying reaction pathways. In the first abstraction stage, noble metal particles of defined sizes are deposited on support oxides with oriented surfaces. This stage enables the identification of catalyst-support-interactions under realistic conditions, while providing a well defined system that allows for precise description and modeling. In a second step, the system can be even further abstracted, e.g., by conducting gas phase studies of ion-molecule reactions under (ultra-) high vacuum conditions. This allows the active sites to be isolated and studied in detail, making it possible to answer questions such as: Which cluster sizes of which elements are reactive? How is reactivity influenced by charge and oxidation states? How is reactivity changed with geometric motifs? An aim to study all three different size regimes is done in the SFB *TrackAct*, funded by the *Deutsche Forschungsgemeinschaft*, whereby the presented work functions as a highly abstracted model system with the goal of identifying the active sites and finding out which important factors influence reactivity. As illustrated in this work, the interaction of charged metal clusters with reactant gases in an ion trap (e.g., ring-electrode ion trap - further denoted as REIT) can here yield information about e.g., cluster size and oxidation effects, underlying reaction mechanisms and kinetic properties.

2.2 Conditions

In order to have a highly defined system, external influences are eliminated by performing the experiments under high and ultra-high vacuum conditions. It is thus ensured that all detected reactivity stems from the investigated system and no contaminants influence the reactivity or poison the catalyst. Moreover, high- and ultra-high vacuum conditions are necessary for certain analytical techniques. In order to further abstract the system, the reaction can be studied on clusters in the gas phase. This eliminates effects of support interactions and allows the system to have a de-

fined charge and oxidation state, which would otherwise be modified by the interaction with the support. The system present is simple enough that it can be efficiently modeled using theoretical tools such as density functional theory (further denoted as DFT) [22]. Depending on the number of collisions and whether a buffer gas is present during the reaction or not, different reaction conditions are achieved [23, 24]. Generally, it is distinguished between single- and multi-collision conditions. In single collision-conditions, the reactive cluster only collides with the reactant molecule once. Released energy leaves the system via radiative cooling, which is, however, extremely slow for isolated clusters in the gas phase [25, 26]. Therefore, it is more likely that subsequent reactions are initiated or fragmentation of the as-formed products takes place [24]. From a thermodynamic point of view, this isolated system can be considered adiabatic, meaning that the total energy is conserved [27]. In contrast, under multi-collision conditions, relaxation is achieved several orders of magnitude faster, allowing the cluster ions to interact several times with the buffer gas (usually a noble gas) as well as with the neutral reactants. This allows energy to be transferred between the components and released energy is distributed almost immediately over the present buffer gas [23]. These collisions therefore lead to a quick thermalization of the system, opening up the possibility of stabilizing reaction intermediates that would otherwise be unstable under single-collision conditions. Thermodynamically, this process can be modeled as isothermal [27]. Besides the thermalization, another difference is the possibility to activate a molecule under multi-collision conditions by providing it with additional energy [28]. The thermal excitation corresponds to the sum of all collisions and binding energies [27]. In general, different reaction pathways can be observed under these different reaction conditions [24], with multi-collision conditions usually being closer to realistic systems.

2.3 Reactivity Studies

In this work, ion-molecule reactions carried out under multi-collision conditions are investigated. The concept of ions driving reactions in the gas phase is already present since the early 20^{th} century [29, 30]. Initially, however, they were mainly used for so-called chemical ionization. This is a softer ionization method compared to electron ionization, which often leads to intense fragmentation [31, 32]. It was shown that the isolated ions in the gas phase have long-ranged interactions [33]. The collisional cross

section of ions interacting with neutral atoms or molecules exceeds the one of neutral species interacting with each other [34]. Nowadays, ion-molecule reactions are widely used to gain deeper insights into the underlying reaction mechanisms. Depending on the charge of the ion, different investigation possibilities arise. For cation-molecule reactions, charge transfer reactions occur predominantly [35]. An example for anion-molecule reactions is the nucleophilic substitution (S_N2) [35]. Furthermore, by adding a defined amount of solvent molecules to the ion-molecule reaction, the influence of the solvent on the reaction can be studied in the gas phase [35]. These so-called micro-solvent experiments demonstrate that gas phase ion-molecule reactions can be utilized in many ways to meet the requirements of the desired model system. Charged metal clusters are also often used in ion-molecule reactions to study the active sites of catalysts, which primarily allows reaction intermediates and products as well as kinetic information to be determined. In all of the systems described, it is advantageous to store the ions when they interact with neutral reactant gases [36]. Therefore, so-called ion traps are used, confining the ions radially and axially [37]. The storage time is then equivalent to the reaction time so that the ion trap acts as a batch reactor. In order to analyze the reaction products, mass spectrometry is widely used [31, 33, 35], as it enables a fast detection of the charged species with high sensitivity.

2.4 Spectroscopic Measurements

While ion trap studies give information about reaction products, intermediates and therefore the underlying reaction mechanism, spectroscopic methods like trapped ion electron diffraction (further denoted as TIED) or infrared depletion/dissociation spectroscopy can provide geometric information about the metal(-oxide) clusters, possible stable intermediates, and reaction products. TIED combines ion trap mass spectrometry with electron diffraction [38]. Size selected clusters are thereby stored within an ion trap and bombarded by electrons from a high-energy electron beam [39]. These electrons are scattered by both the atomic nuclei and the surrounding electrons due to *Coulomb* interaction [38]. This results in a diffraction pattern, which is recorded by a CCD camera. Using DFT, the theoretical diffraction patterns stemming from possible candidate geometries are calculated and compared with the experimental data to identify the structure(s) present (shown for Pt_6^- in Figure 2) [39, 40]. The clusters can be chemically modified in the cluster source prior to performing TIED by introducing

a reactant gas. With this, not only the structure of the bare metal clusters, but also chemically modified reaction products can be analyzed, as it was shown by *Gojare* et al. for $Pt_{12}H_{24}^-$ [40].

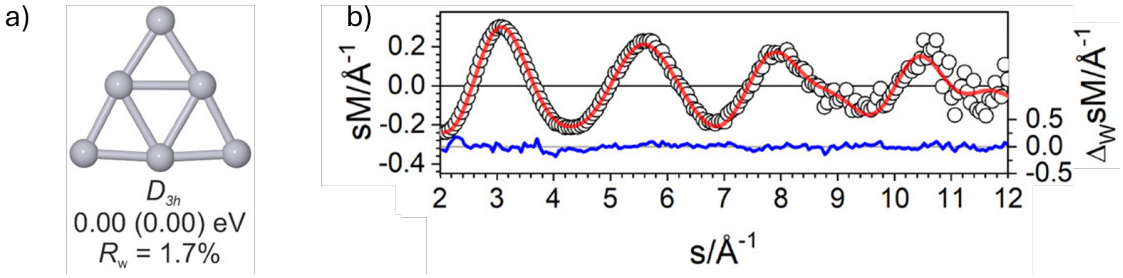

Figure 2: a) Possible isotope structure of Pt_6^-. b) The circles show the experimental scattering data of Pt_6^- in comparison to the calculated modified molecular scattering intensities SM for the structure shown in a). Blue shows the weighted residuals. The strong agreement of theoretical and experimental data (R_w = 1.7%) confirms the presence of this geometry of Pt_6^-. Reproduced in part with permission from [39]. Copyright 2022 *American Chemical Society*.

Structural analysis of clusters using infrared depletion/dissociation spectroscopy is based on the dissociation of species upon the absorption of photons. Experiments are often conducted using free-electron-lasers [41], but table-top systems are also applied [42]. The molecular cluster beam interacts with an often counter-propagating IR laser beam of tunable wavelengths. When the photon energy equals an IR active absorption band of the cluster, vibrational modes of the species can be excited (see Figure 3). This excitation can lead to the dissociation of the compound if the absorbed energy exceeds its binding energy. As a result, the clusters in the beam become depleted. In infrared depletion spectroscopy, the ion intensity of the parent species is recorded in dependence of the irradiation wavelength using mass spectrometry [43]. Another option is the investigation of the as-formed fragments, which is then referred to as action spectroscopy. Comparing the observed resonance IR frequencies with the theoretically calculated vibrational spectra of candidate structures allows the identification of geometries present [43–45]. Combining these approaches of structure identification with ion trap reactivity studies can enable the identification of reactivity determining motifs, geometry changes during the reaction, and possible driving forces.

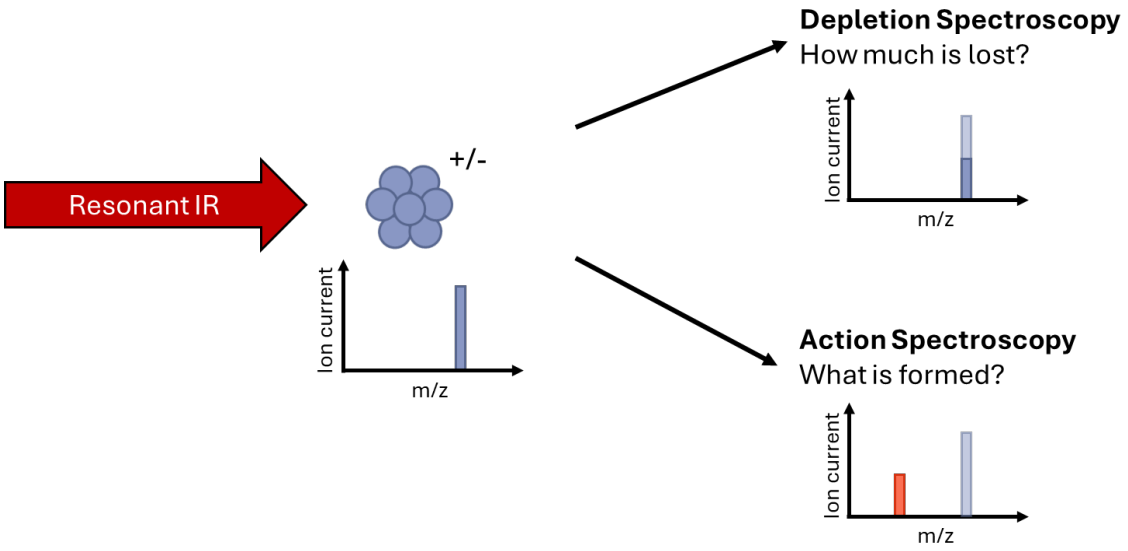

Figure 3: Resonant IR radiation interacts with the cluster, leading to its excitation. When the loss of the parent ion is investigated, it is referred to as depletion spectroscopy, while in action spectroscopy, the formed fragments are studied.

2.5 Theoretical Modeling

In addition to interpreting spectroscopic data, theoretical modeling can be used to complement experimentally obtained reactivity and structure information. It functions as an essential tool for predicting and analyzing features like electronic structures, molecular interactions, and material characteristics. A polyatomic system, such as a molecule or a cluster, is defined by structural properties related to the shell structure, electric and magnetic moments, and the geometry of the system, such as bond angles, bond lengths, and possibly symmetry arrangements [46–48]. In order to model such a system, the electronic ground state must be known, from which all of the above mentioned information can be derived. According to the *Hohenberg-Kohn* theorem [49], these ground state electrons can be described by the electron density of the system. In the second part of the theorem, it is stated that by varying the electron density of the ground state, only states of higher energy are generated. Therefore, by optimizing this energy using a systematic variation of the electron density, the ground state and its energy can be determined. This forms the basis for DFT [48]. DFT was supplemented by the *Kohn-Sham* formalism, which introduces a system of

non-interacting electrons that yields the same electron density as the real system. It reduces the complexity drastically by transforming the many-particle *Schrödinger* equation into a set of single-particle equations [46]. Separating the electronic and nuclear terms of the *Hamiltonian* operator of a chemical system according to the *Born-Oppenheimer* approximation results in the corresponding *Schrödinger* equation of the electronic system, which is given as [47]:

$$\hat{H}_{el}(\overrightarrow{r};\overrightarrow{R})\Psi_e(\overrightarrow{r}) = E(\overrightarrow{R})\Psi_e(\overrightarrow{r}) \tag{1}$$

where $\hat{H}_{el}$ is the *Hamiltonian* operator including the kinetic energy of the electrons and the repulsive energy between electrons as well as the attractive energy between nuclei and electrons, $\overrightarrow{r}$ describes the electronic degrees of freedom, $\overrightarrow{R}$ the nuclear degrees of freedom, Ψ_e is the wave function of the electrons and E($\overrightarrow{R}$) - the eigenvalue of the *Schrödinger* equation - is the potential energy. By solving the *Schrödinger* equation for this potential energy, a 3N - 6 dimensional potential energy hypersurface (further denoted as PES) can be determined, where N equals the number of nuclei in the system (see Figure 4). In the theoretical modeling of a system, specific points on this PES are of special interest [50]. Local minima correspond to ground state structures of reactants, intermediates, and products while local maxima may reflect transition states during the reaction. Following the reaction coordinates on the determined PES, the energy progression during the course of a reaction, known as the reaction path, can be observed. This is exemplified for the transformation of ozone to isoozone in Figure 4.

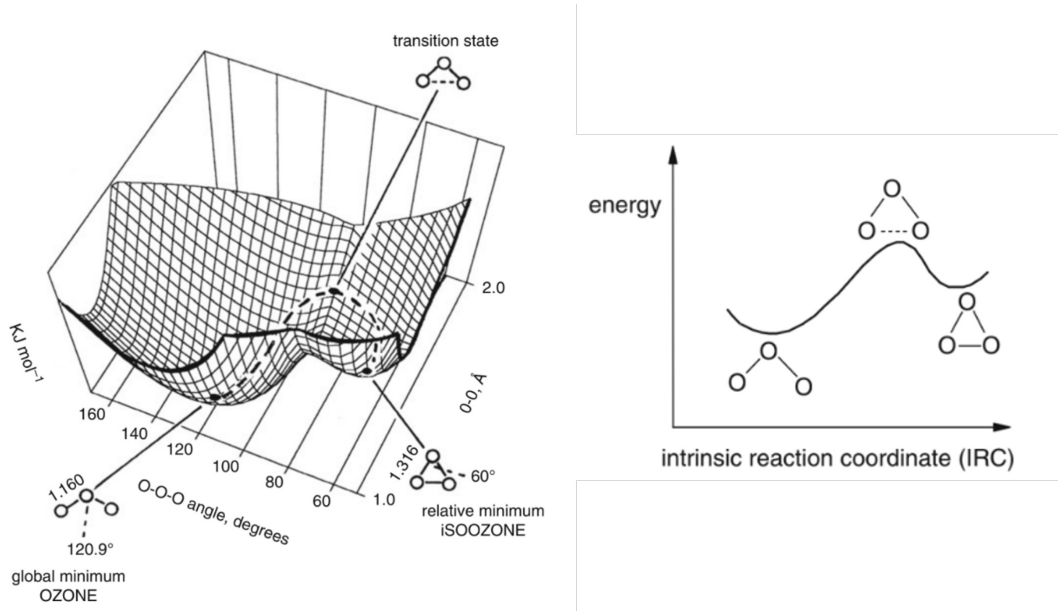

Figure 4: PES for the transformation of ozone to isoozone. While the ground states of ozone and isoozone are local minima, the transition state is located on a local maximum (left). Following the reaction coordinates, the 2D reaction path (right) can be determined. Taken and modified from [50]. Reproduced with permission from *Springer Nature*.

3 Experimental

3.1 Experimental Setup

All experiments evaluated and performed within this work have been measured in a high-vacuum chamber (shown in Figure 5) with base pressures ranging from below $5 \cdot 10^{-6}$ mbar (in the cluster source) to $< 2 \cdot 10^{-9}$ mbar (in the cluster reactivity part). The clusters of interest are generated in the cluster source, mass selected in the quadrupole mass filter (further denoted as QMF) and can then react with the desired gas(es) in the REIT. The analysis of all charged reaction products is thereafter done in a (reflectron) time of flight mass spectrometer (further denoted as (re-)ToF-MS).

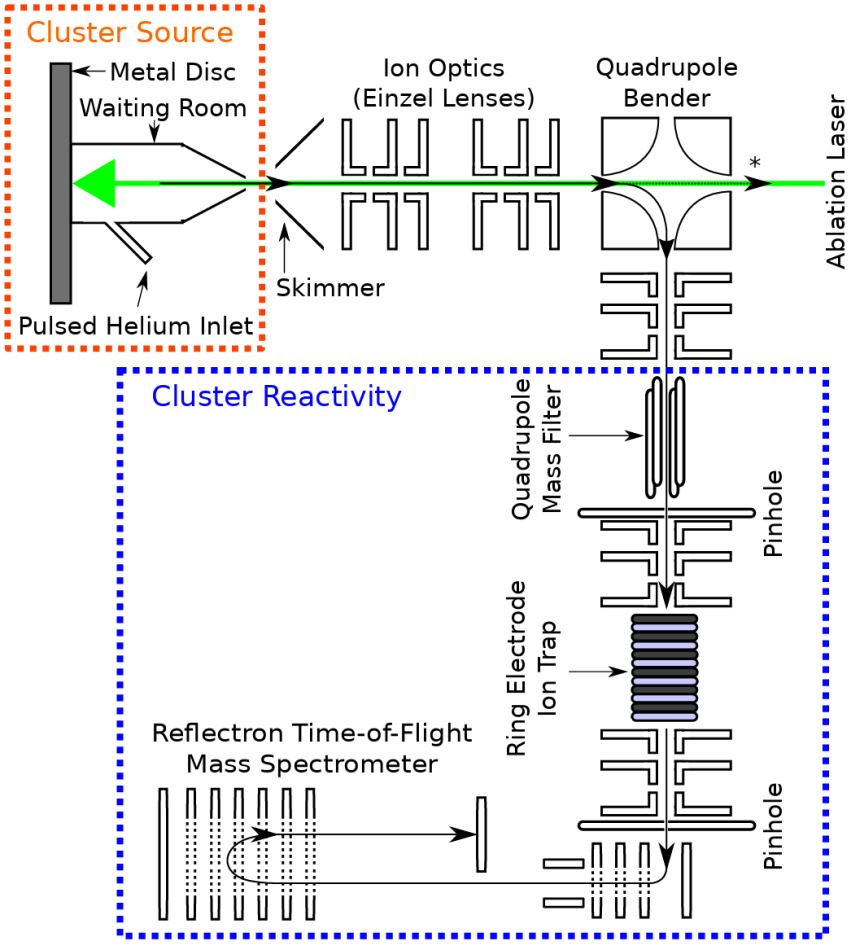

Figure 5: Scheme of the apparatus used, which can be divided into a cluster source (orange) and the cluster reactivity part (blue), in which the reaction and the analysis of the reaction products take place. Taken from [36].

3.1.1 Cluster Source

The cluster generation takes place in a laser vaporization cluster source, originally designed by *Smalley* et al. [51], later adapted and modified by *Heiz* et al. [52] This cluster source consists mainly of a rotating metal disc target and a first waiting room, which is periodically filled with the buffer gas helium (He 5.0, Westfalen). The source used within this setup was further modified by *Masubuchi et al.* [53] to include a second waiting room (see Figure 6) for the chemical modification of the as-formed clusters, e.g., by their oxidation (with oxygen O_2 5.5, Air Liquide) or the interaction with ammonia (NH_3 6.0, Linde).

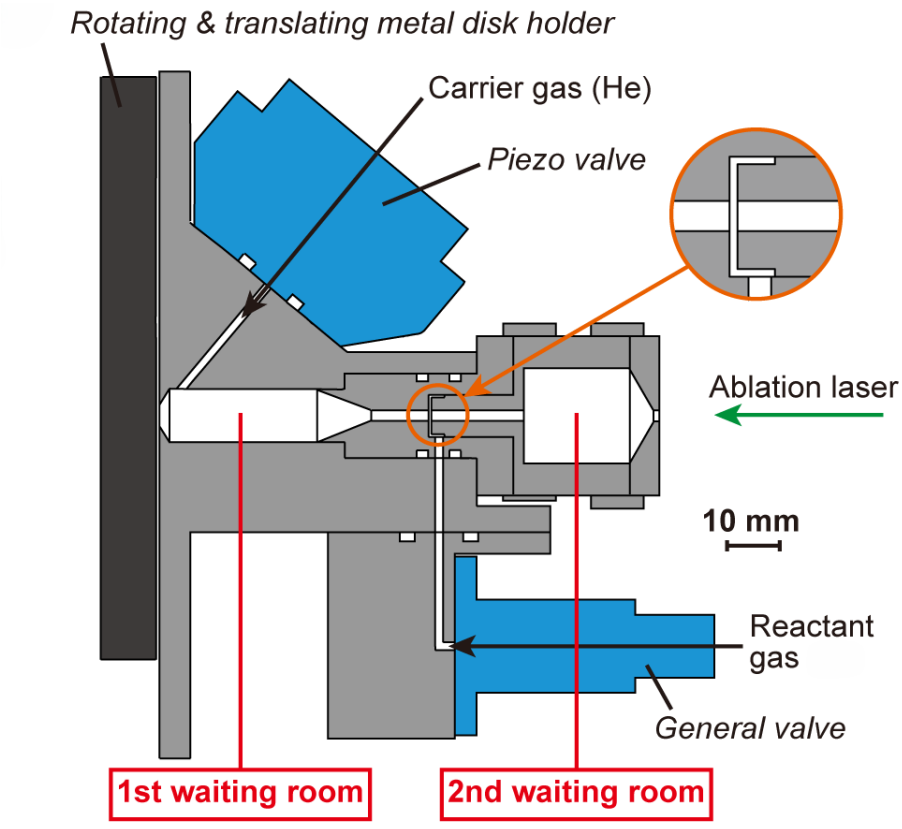

Figure 6: Scheme of the used laser vaporization cluster source consisting of a rotating metal disc target, a first, and a second waiting room. Used with permission of *American Institute of Physics*, from [53]; permission conveyed through *Copyright Clearance Center, Inc*.

The beam pulses of the second harmonics of a Nd:YAG laser (532 nm, Innolas Spitlight DPSS, 60 mJ/pulse, 10 ns pulse width, 100 Hz repetition rate) hit the metal disc target rotating within a hypocycloid gear. This emits hot atoms and ions into the first waiting room, into which helium is introduced using a piezo valve (typically 6 bar stagnation pressure, $\approx$ 400 μs pulse width, 100 Hz repetition rate). The added buffer gas acts as a carrier gas and enables quick thermalization of the formed gaseous mixture through multiple collisions, which leads to the generation of clusters. Thereafter, they are migrated into the second waiting room, pre-filled with the desired reaction gas via a solenoid pulsed valve (2 bar stagnation pressure, $\approx$ 100 μs pulse width, 100 Hz repetition rate). In order to push the ions and any remaining reactant gas out of the second waiting room, it is important that the pressure of the buffer gas (He) is greater than the one of the reaction gas. Due to this pressure gradient, the clusters leave the second waiting room through the nozzle, undergoing fast expansion, which results in an efficient cooling of the clusters [54]. In order to handle the high gas load, a rotary vane pump (Ruvac WS 1001 with the pre-pump Busch R5 RA 0205) is used to remove the gas from the vacuum chamber. One advantage of this method of generating clusters is that they can be produced in a wide size range, which can be influenced by the He pulse width, pressure, and timing. Furthermore, it enables cluster-adsorbate reactions, such as the oxidation of the clusters, to be carried out within the cluster source under thermalized conditions. This way, more complex reaction mechanisms (e.g., the interaction with CO_2 and CH_4) can be disentangled by first only examining the reaction of the clusters with CO_2 in the ion trap and then pre-oxidizing the clusters in the cluster source and only introducing CH_4 into the ion trap. Finally, both reactant gases can be added to the ion trap simultaneously [55].

3.1.2 Ion Guides, Quadrupole Bender, and Quadrupole Mass Filter

Controllable electrostatic lenses, known as einzel lenses, are used to guide the resulting clusters from the cluster source into the reaction and detection area of the setup [56–58]. One set of einzel lenses consists of three individually adjustable metal plates. This enables modifiable and focusable trajectories of the ions without changing their kinetic energy within the cluster beam. The einzel lenses are also used to monitor the transmission throughout the setup. By connecting a picoammeter (Keithley) to an einzel lense and applying an attraction voltage of +/- 20 V to it, while putting a repelling voltage of 250 V of the opposite polarity on the following einzel lens, the re-

spective fraction of the cluster beam hits the lens and the cluster current is measured. Since the formation of multiply charged clusters is negligible, it can be assumed that the measured current corresponds to the amount of clusters striking the lens. This way, the ion optics of the setup can be tuned for an optimized cluster beam transmission. As observed in this work, the main losses of cluster beam occur at the bender ($\approx$ 75% transmission), at the QMF ($\approx$ 10 - 15% transmission) and at the REIT ($\approx$ 80% transmission in ion-guide mode). After the first three sets of einzel lenses, the cluster beam enters the quadrupole bender. The quadrupole bender uses a two-dimensional electrostatic field to deflect the ion beam, in this setup by 90° [59, 60]. This allows for the separation of neutral (undeflected) species, including clusters and the He buffer gas, from the cationic or anionic clusters. Depending on the desired cluster species, ions in this charge state enter the second part of the setup.

A variety of cluster sizes arrives at the QMF. This consists of four rods, to which a high direct current U and a high-frequency alternating current V $\cdot$ cos(ωt) is applied, whereby opposite pairs of rods are electrically connected. Two of the rods have the potential (U + V $\cdot$ cos(ωt)) applied, while the other two have a potential of -(U + V $\cdot$ cos(ωt)) [61]. Thereby, an electric field is induced inside the quadrupole, which is oscillating over time. Hence, ions within the QMF are also stimulated to oscillate. It is observed that for stable ("resonant") m/z ratios, the amplitude of this oscillation stays the same and the clusters can leave the mass filter. Whereas for unstable ("non-resonant") ions, the amplitude of the oscillation increases as they pass through the QMF until the clusters hit the rods or the housing of the mass filter and are thereby removed from the cluster beam. In this apparatus, the QMF Model 5221 (Extrel) is used, which enables the mass selection of ions with masses up to 1.600 amu and a transmission of up to $\approx$15% according to the manufacturer.

3.1.3 Ring Electrode Ion Trap

The mass-selected clusters are then guided into a home-built REIT [62], which is based on the designs of *Gerlich* [63] and *Goebbert* et al. [64]. The ion trap consists of 24 ring electrodes, insulated by sapphire discs, and two bigger plate electrodes located at the entrance and the exit of the trap. With this trap, a wide size-range of clusters can be stored for up to several seconds, followed by a controlled ejection of the ions into the adjacent re-ToF-MS. The trap is filled with helium (He 6.0, Westfalen)

as a buffer gas. Within the set pressure regime (here: 0.7 - 0.8 Pa), ion-molecule reactions take place under multi-collision conditions, leading to a quick collisional thermalization of the clusters within 1 ms [65]. Moreover, the kinetic energy of the ion beam is quickly dispersed. By applying suitable potentials to the electrodes, the low-energetic ions can be stored efficiently. For the annular electrodes, a RF-potential is applied, whereby the phase of two neighboring electrodes is shifted by 180°. This results in a radial confinement of the ion movement. Additionally, a DC voltage in the range of 10 - 20 V on the entrance and the exit electrodes confine the ion movement in axial direction. While the clusters are trapped for a defined storage time, reactant gases are introduced via a mass flow controller (179C Mass Flow Meter, 500 sccm range, MKS). The pressure during the reaction is monitored using a capacitance manometer (Baratron model 722B, MKS) and set to 0.77 Pa using a flow rate of 170 sccm. To realize a reaction with a defined amount of reactant gas in the ion trap, the desired gas (CH_4 5.5, Rießner Gase; CD_4 99.9% isotope enrichment, Eurisotop; and NH_3 1% in N_2, Linde; respectively) is first diluted in the buffer gas He inside the mixing chamber. The mixing chamber is connected to the apparatus via a mass flow controller, enabling a defined and continuous flow into the ion trap. Typical values for the concentration do not exceed the percentage range, ensuring a slow enough reaction to determine the reaction kinetics of thermalized reactants.

3.1.4 Reflectron Time of Flight Mass Spectrometer

The characterization of the charged reaction products from the REIT and the determination of their abundancies takes place in the home-built *Wiley-McLaren* type re-ToF-MS (see Figure 7) [66]. First, clusters enter the acceleration stage, which consists of the repeller plate (with the applied potential U1) and the extractor plates (with an applied voltage gradient from U2 to ground). Two additional deflector plates allow for a correction of the extraction direction. To achieve higher mass resolution, the cluster beam is deflected by 90° from its original direction in this stage. Because the difference in initial velocities of the clusters in extraction direction is negligibly small, the final velocity of the clusters is only dependent on their mass when accelerated by a constant voltage, assuming that all species have a charge of ± 1. The extraction into the spectrometer is achieved by applying a short HV pulse (50 - 150 μs) to the repeller and extractor plates. The voltage ratio U1/U2 determines the space focus of the ions [66, 67]. There, clusters with the same m/z ratio, which differed in space ini-

tially, arrive at the same time. For the present re-ToF-MS, the space focus is chosen to be in the reflectron stage, which acts as an ion mirror, the purpose of which will be explained later in this section. In this setup (see Figure 7), the desired space focus is achieved using a U1/U2 ratio of 1.30 (e.g., 4.32 kV/3.31 kV). For a linear ToF, the space focus is supposed to be on the microchannel plate detector (further denoted as MCP) in order to achieve maximum mass resolution.

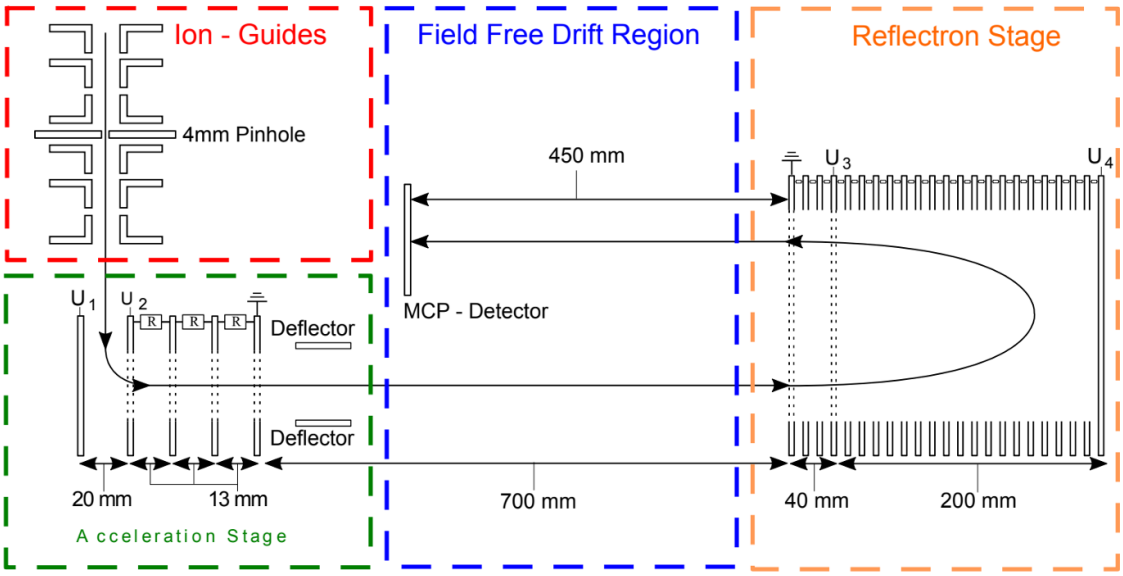

Figure 7: Schematic representation of the re-ToF-MS compartment. Clusters are guided into the re-ToF-MS via the ion guides (einzel lenses), deflected by 90° and accelerated in the acceleration stage, pass through the field free drift region, and get reflected in the reflectron stage. After crossing the field free drift region again, they are detected by an MCP detector. Taken from [36].

After the acceleration stage, ions enter the field free drift region, where mass separation takes place. Since all ions with the charge q (here, either a single positive or negative charge) are accelerated by the same voltage U, the final kinetic energy E_{Kin} is given by:

$$U \cdot q = E_{Kin} = \frac{m \cdot v^2}{2} \tag{2}$$

with m being the mass of the ions and v their velocity in z-direction.

As U · q is constant, ions with higher masses are slower. Since the time of flight is related to the ions' velocity as:

$$v = \frac{s}{t} \tag{3}$$

with s being the distance traveled, in this case the field free drift region, and t the time of flight, the following proportionality between mass and flight time can be derived:

$$m \propto \sqrt{t} \tag{4}$$

After the field free drift region, the ions enter the reflectron stage. This stage compensates changes in the kinetic energy of ions with the same mass [68]. Here, two voltage gradients are applied, one that decreases from the repeller plate U4 to the extractor plate U3 and a second one from U3 further to ground. Ions with a higher kinetic energy can penetrate this electric field deeper and. Therefore, they spend more time in the reflectron stage, which cancels out the potential differences in flight times of ions with same m/z ratios. For the highest mass resolution, the ratio U4/U3 has to be chosen so that the space focus is on the MCP detector. In this setup, this ratio is 2.19 (e.g., by applying 4.64 kV/2.12 kV). With the present setup, a mass resolution $\frac{m}{\Delta m}$ of up to ≈3.000 can be achieved [36].

3.1.5 Additions and Changes to the Setup

As mentioned in Section 3.1.2, the einzel lenses are used not only for ion focusing, but also for measuring the cluster current at specific positions within the setup, which facilitates its optimization. However, a problem arises once the last stack of einzel lenses is passed. Since the clusters still have to pass through the relatively large

extraction area of the re-ToF-MS, the last einzel lenses have to be optimized without the possibility of measuring the cluster current as usual. Instead, voltages can only be optimized efficiently once a signal in the re-ToF-MS is obtained successfully. In order to improve this process, a *Faraday* cup (see Figure 8) was added to the setup. The *Faraday* cup consists of a stainless steel plate, which is electrically insulated from its mounting. A connection from this plate to the non-vacuum side of the chamber is achieved by a BNC feedthrough with a bayonet plug-in connection (Vacom). Detailed technical drawings including dimensioning are given in the Appendix. The *Faraday* cup is positioned in such a way that, by optimizing the cluster current onto it, it is ensured that the clusters pass through the center of the extraction area.

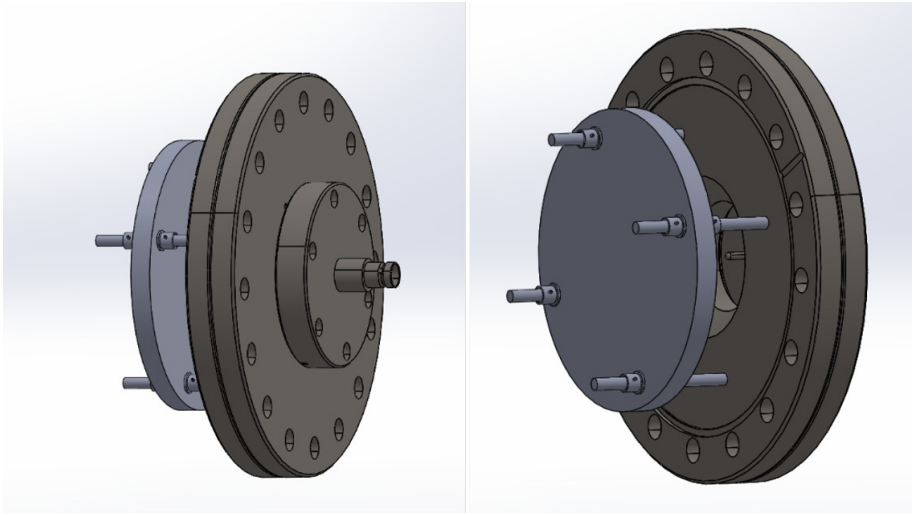

Figure 8: CAD drawing of the newly installed *Faraday* cup, used for the optimization of the cluster current through the extraction area of the re-ToF-MS.

To further facilitate the detection of the ions in the mass spectrometer, the re-ToF-MS was converted into a linear ToF-MS with a field-free drift region of 30 cm. A space focus on the MCP detector is achieved using a U1/U2 ratio of 2.43 kV/2.10 kV = 1.16. This short, linear ToF-MS does not provide the mass resolution necessary for the identification of reaction products from the REIT, but comes with a high ion transmission. Once this transmission is optimized, the re-ToF-MS with an improved resolution can be re-installed. Moreover, a second linear ToF-MS was put back into operation. To enter this ToF-MS, clusters are not deflected within the bender, but are guided straight through the setup until they enter the extraction region of the new ToF-MS.

Since no main components are passed, which is always connected to cluster loss, a high transmission of clusters is achieved, allowing for a simple and fast evaluation of the species formed in the cluster source. This linear ToF-MS has, similarly to the original re-ToF-MS described in Section 3.1.4, a *Wiley-McLaren* extraction stage [66]. The ions are space-focused onto the MCP detector and the m/z separation takes place within a ≈65 cm long field-free drift region. Space focusing is achieved by choosing a voltage ratio of the repeller plate to the extractor plate U_{rep}/U_{extr} = 1.15. With this ToF-MS, a mass resolution $\frac{m}{\Delta m}$ of approximately 400 - 500 is obtained, which is discussed in more detail within Section 6.

For the linear ToF-MS, an already mounted MCP was used during first experiments. However, this detector only allowed the detection of cationic species. Therefore, a new z-stack MCP detector was installed. It is manufactured in a configuration in which both, cationic and anionic species, can be detected and its geometry allows for a much higher signal amplification in comparison to the original detector with a Chevron geometry. In general, there are two types of operation modes of MCPs, both following the same idea of generating an electron cascade from the impact of the initial species by accelerating the thereby produced electrons toward the detection plate using a voltage gradient. Therefore, MCP detectors usually consist of at least two plates, as shown in Figure 9.

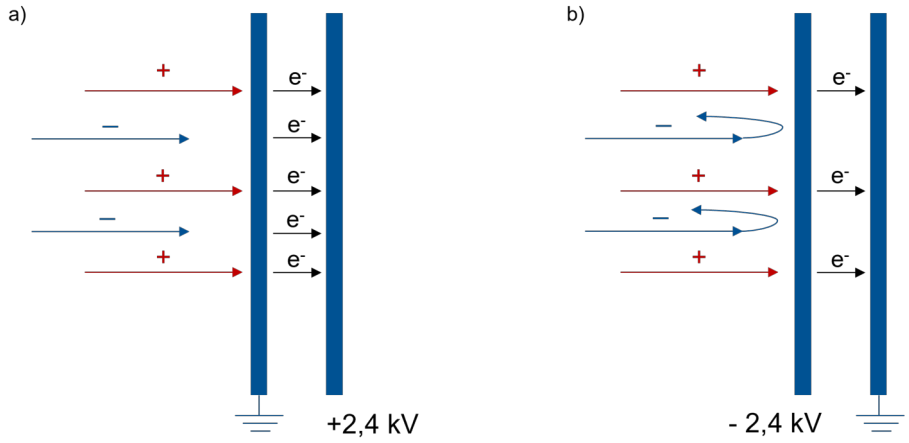

Figure 9: Schemes showing the two different working principles of MCP detectors. While a) allows for the detection of both, anionic and cationic species, only cations can be detected using the setup depicted in b).

The voltage gradient is either achieved by grounding the first plate (see Figure 9.a) and putting a high positive voltage onto the detection plate or by applying a high negative voltage to the first plate (compare Figure 9.b) and grounding the detection plate. While an additional capacitive decoupling is needed for the signal readout in option a, this setup allows for the detection of anionic, cationic, and neutral species. In contrast, option b allows direct signal readout, but at the expense of anion detection, as these are deflected by the high negative voltage of the first plate.

The new z-stack MCP detector MCP-050-Z-L-A (tectra) works according to the principle shown in Figure 9.a, but uses an additional acceleration stage, which is another difference to the previously used Chevron detector. The mounting is shown in Figure 10.

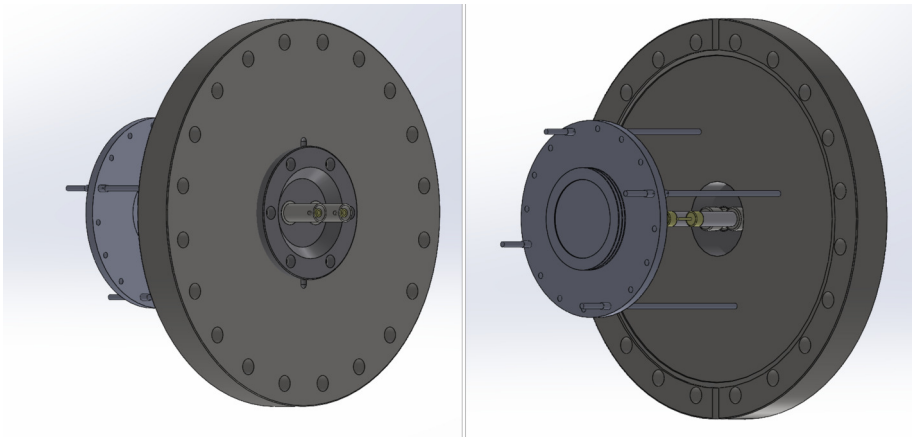

Figure 10: Mounting of the MCP onto a CF160 to CF40 reduction flange. 10 kV SHV feedthroughs are connected using a CF40 flange.

The detector must not have any electrical contact to the mounting, which is achieved by electrically insulating ceramic discs (tectra). It is mounted onto a CF160 to CF40 reduction flange (Vacom) using threaded rods and fixing screws. In order to apply the high voltages to the detector plates, a 10 kV SHV feedthrough is connected via a CF40 flange (Vacom) to the mounting flange. To achieve the desired voltage gradient, a voltage divider was connected to the MCP by the in-house electronics workshop, using resistors following the scheme shown in Figure 11. The resistors were selected so that a maximum voltage difference of 3 kV occurs between MCP_in and MCP_out, while the anode deviates by a maximum of 0.5 kV from MCP_out. At room

temperature, MCP_in and MCP_out are separated by a total resistance in the range of 100 - 150 MΩ, with the resistance distributed evenly across the three individual plates, resulting in a continuous voltage gradient within the MCP detector. According to literature, the internal resistance is expected to decrease with increasing temperature and voltage [69]. For the signal readout, an additional 10 kV SHV feedthrough is added. A capacitative decoupling of the signal is achieved by adding a 235 pF capacitor according to Figure 11. A 10 kV SHV to SHV connector for HV application and a 10 kV SHV to BNC connector for the signal readout were manufactured in the in-house electronics workshop. Detailed technical drawings of this detector setup including all dimensions are given in the Appendix.

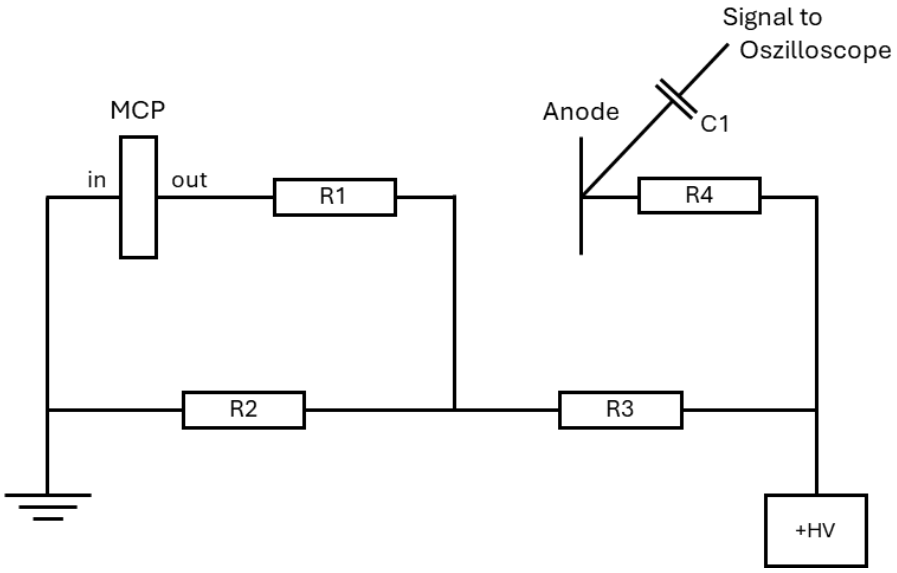

Figure 11: Circuit diagram of the installed z-stack MCP detector, whereby R1 = 2 MΩ, R2 = 5 MΩ, R3 = 0.5 MΩ, R4 = 10 MΩ and C1 = 235 pF.

During the course of this thesis, anionic and cationic clusters are analyzed using the ToF-MS. Therefore, the polarity of the pulses in the acceleration stage is changed. The HV pulses are generated with an HV pulser build in the electronics workshop using a HTS 61-03-GSM MOSFET push-pull switch (Belke) as a fast HV transition switch. When changing the polarity of the voltage, the trigger pulse has to be adjusted accordingly. For positive voltage pulses, any rising flank with a voltage difference of 5 V triggers the pulser (compare Figure 12 red pulse), while for negative voltages, a falling flank with a difference of -5 V is needed (compare Figure 12 blue pulse). The

trigger pulse has to be adjusted for the desired polarity before applying the voltage. Otherwise, the current flowing will exceed the limit value for the components and the high-voltage transition switch may be destroyed.

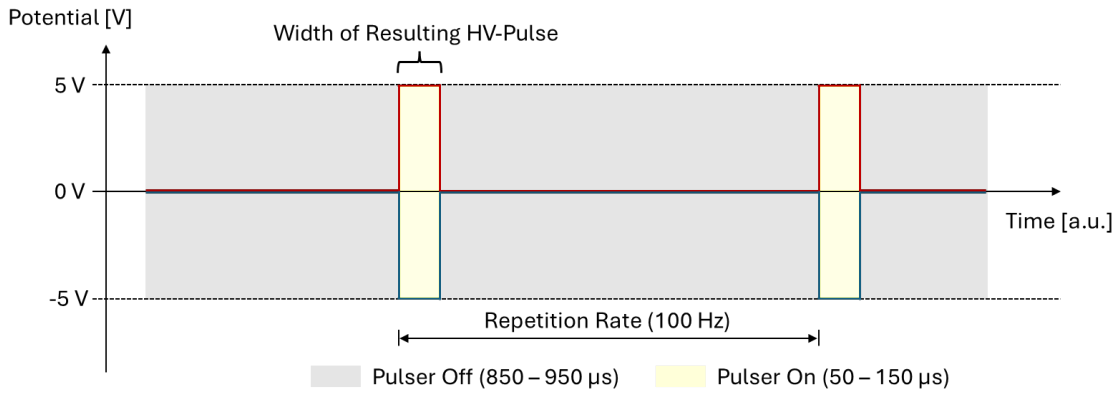

Figure 12: Trigger pulses for positive (red) and negative (blue) HV pulses used in the acceleration stage of the ToF-MS. The repetition rate is matched to the 100 Hz laser. Depending on the experiment, the pulser is switched on for 50 - 150 μs, which corresponds to the length of the resulting HV pulse.

3.2 Data Evaluation

When evaluating the data recorded in the re-ToF-MS, a first step includes the transformation of the time of flight axis into m/z units. Exemplary, this procedure is shown for the data of cationic tantalum oxide clusters in the following. The general mass range of the present clusters is known from the QMF. With this knowledge, a broadband spectrum (see Figure 13) is recorded in the re-ToF-MS. Here, peaks of Ta_4^+ – Ta_{10}^+ and their oxides are shown. By assigning the m/z values to the respective tantalum species and their flight times, a linear equation with $\sqrt{m} \propto t$ (t being the time of flight) can be obtained. This enables the transformation of the x-axis. Additionally, oxide peaks are visible in the spectrum. The mass difference of such an oxide peak to the neighboring lighter species, shown exemplary for Ta_5O^+ and Ta_5^+, corresponds to an m/z ratio of +16, which confirms a correct conversion.

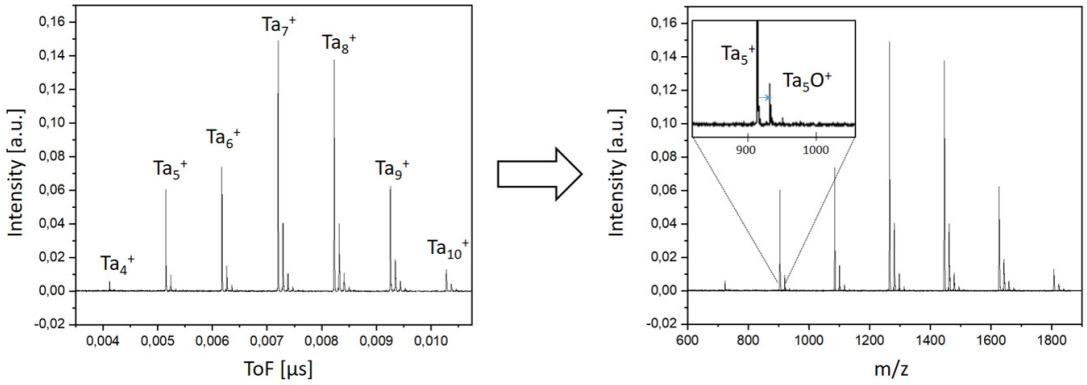

Figure 13: Broadband spectrum of Ta_4^+ – Ta_{10}^+ clusters and their oxides, used for the scale conversion from time of flight (left) to m/z (right).

The resulting linear equation is used to transform the x-axes of all obtained mass spectra recorded using the same re-ToF-MS settings. After the axis conversion, the species present are assigned for all investigated reaction times. The area under the mass peaks is obtained by integration, which corresponds to the abundance of each species. By plotting these abundances of every compound against the respective reaction time, a plot of the reaction progress is acquired. This extraction from the mass spectra is exemplarily shown for the reaction times 0.005 s, 0.010 s, and 0.100 s for $Ta_2O_2^+$ in Figure 14.a. The corresponding kinetic plot is displayed in Figure 14.b. Analogously, for $Ta_2O_5^+$, the reaction times 0.005 s, 0.020 s, and 0.200 s are given in Figure 14.c with the corresponding kinetic plot in Figure 14.d.

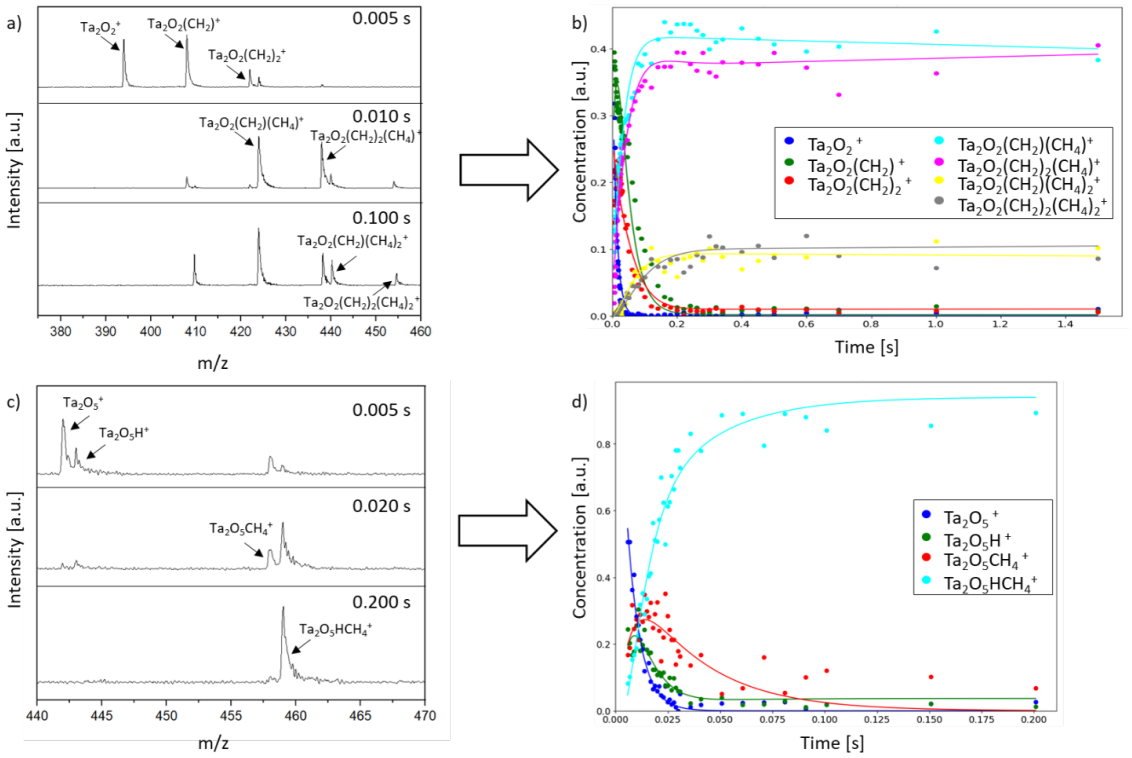

Figure 14: Re-ToF mass spectra for different storage times in the REIT for a) $Ta_2O_2^+$ and c) $Ta_2O_5^+$ and the respective kinetic fits of the reaction progresses, shown in b) and d).

3.3 Computational Methods

DFT calculations have been performed for $Ta_2O_x^+$ (with $0 \leq x \leq 6$) (discussed in Section 5) to gain deeper insights into underlying reaction mechanisms and to strengthen the assumptions derived from experimental data. *Orca 5.0.3* was used as the general-purpose quantum chemistry package and all calculations have been performed on the LRZ Linux-Cluster *CoolMUC-2*. The good agreement between the theoretical work on $Ta_xO_y^+$ clusters (with $6 \leq x \leq 11$ and $0 \leq y \leq 2$) and the IR spectra measured by *Fielicke* et al. [45] served as the basis for the chosen approach. A functional of *Tao, Perdew, Staroverov,* and *Scuseria* (TPSS) [70] was applied for the correlation energy, which is located on the meta generalized gradient (m-GGA) level. As a basis set, a balanced triple ζ valence basis set is applied, which includes polarization functions (def2TZVP) [71]. Moreover, *van der Waals* forces are considered by adding the dispersion correction of *Grimme* et al. (DFT-D3) [72]. The resolution of identity approximation (RIJ) was used for all calculations [73]. Analytical IR spectra are employed to characterize calculated structures either as ground states (GS) or transition states (TS). Thereby, only positive vibrational frequencies are attributed to GS structures, while one negative frequency suggests the presence of a TS structure. Zero-point energy (zpe) corrections have been performed for all reported energies, as well as the correction by thermal and entropic contributions, leading to the final *Gibbs* free energies calculated at a temperature of 298.15 K and a pressure of 1 atm ($1.013 \cdot 10^5$ Pa). Within an optimization process, the number of electrons with up and down spins is kept fixed so that the multiplicity of the species is given by 2S + 1. However, in order to check the present multiplicity and multiplicity changes during the reaction, potential energy calculations have been carried out for the lowest three multiplicities for all calculated structures. The general approach for identifying TS structures involved the determination of the reaction paths using relaxed surface scans, whereby the reaction coordinates are altered in small increments. Following such a reaction path enables the determination of local minima and possible barrier configurations, whereby structures with maximum energy on this potential energy surface are suggested as TS structures and further optimized with respect to the negative vibrational frequencies.

4 Activation of CH_4, NH_3, and N_2 by Tantalum Ions, Clusters and Their Oxides: What Can Be Learnt from Studies of Ions in the Gas Phase [14]

In order to get an overview of how gas phase studies can provide information about a system, a first part of this dissertation project was collecting, comparing and discussing recent research results on the interaction of tantalum ions, clusters and their oxides with CH_4, NH_3, and N_2. This section provides a general overview of the reactivity of these species, while a more detailed review of relevant literature can be found in our published review article [14].

4.1 Reactivity with Methane

The adsorption of reactants on catalysts plays an important role in the activation of a compound. Dependent on the present metal, cluster size and oxidation state, different reaction pathways are observed. In the case of methane, its activation occurs predominantly according to one of the following three ways (see Figure 15): i) The first activation mechanism shows a hydrogen atom transfer (further denoted as HAT), in which the catalyst mainly interacts with one hydrogen atom. This leads to a stretching and thus weakening of the respective C−H bond, which ultimately results in its cleavage and the release of a CH_3 radical into the gas phase [74]. This process was first described by *Wang* and *Lundsford* on Li-doped MgO [74], but was also found on $[V_4O_{10}]^+$ [75]. This type of reactivity is mainly attributed to the presence of a high spin density on the interacting oxygen atoms [76]. ii) The second activation mechanism involves the insertion of a metal atom of the catalyst into the C−H bond of methane, again leading to its elongation, weakening, and possibly to its cleavage. The process can be repeated for several C−H bonds, enabling the evolution of H_2. A strong interaction between carbon and an atom of the catalyst leads to an energy gain as soon as a bond is formed, and is the driving force of the reaction [77]. iii) As a third option, methane can interact with the catalyst via a proton-coupled electron transfer (further denoted as PCET). This requires the presence of a *Lewis* acid-base pair on the catalyst [78], which means that the catalyst has to consist of at least two different atoms, both of which are involved in the reaction. Metal-oxides are an example for possible catalysts, which means that the PCET and HAT reactions may be competing

processes if the oxygen atoms have significant spin density [79]. A fourth, less prominent, option involves the formation of η_2-complexes and has been found in the interaction of methane with neutral Pd [80], but since this process has otherwise not been observed, it is not discussed in detail here. When interacting with further methane molecules, the attack of (possibly hidden) hydrides is another activation possibility. Furthermore, in contrast to the metal insertion, a strongly electrophilic carbon atom inserts itself into a C−H bond of the methane, as found e.g., in a stepwise process on AuC^+ [81], and in a concerted process on CuC^+ [82]. This interaction leads to the formation of C−C bonds.

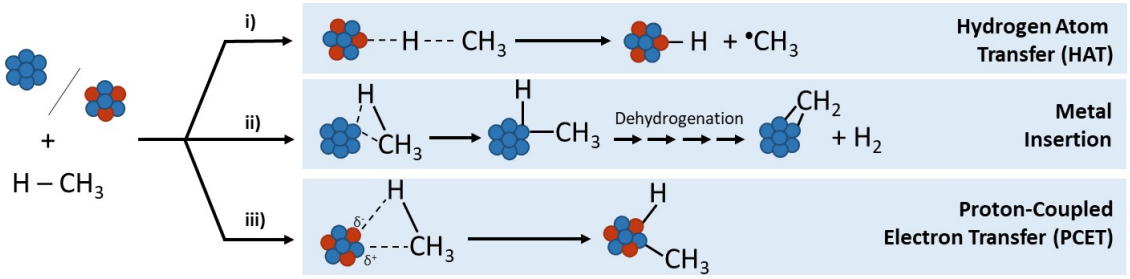

Figure 15: Possible interaction pathways of methane with a metal(-oxide) catalyst. A HAT reaction is shown in i). Thereby, one hydrogen atom interacts with an oxygen atom of the catalyst, resulting in the transfer of a single hydrogen atom and the release of a CH_3 radical. In ii), a metal atom of the catalyst inserts into the C−H bond, resulting in its cleavage. Consecutive metal insertions can thereby result in the dehydrogenation of methane and the release of H_2 into the gas phase. In mechanism iii), two atoms of the cluster act as a *Lewis* acid-base pair. The cleavage of the C−H bond results from a proton-coupled electron transfer. Oxygen atoms are given in red, tantalum ones in blue. Taken from [14].

One element for which several studies have reported the activation of methane and the resulting evolution of H_2 is tantalum. While relativistic effects explain why especially heavier elements like tantalum catalyze this reaction [83], the main driving force for the interaction with methane might be the strong formed metal-carbon bond [77]. The underlying activation mechanism of the cationic tantalum atom, following the metal insertion process, was thoroughly studied [84–88]. The tantalum cation inserts into one of the C−H bonds of the methane molecule, leading to its elongation and eventually its cleavage (see Figure 16) [87, 88]. Thereafter, one of two different pathways can lead to the cleavage of the second C−H bond. Either another, mechanistically identical, metal insertion takes place or the as-formed hydride attacks a

hydrogen atom of the CH_3-moiety. In the case of the metal insertion, an intermediate is formed in which both cleaved hydrogen atoms and the CH_2-group are bound to the tantalum cluster and then form $H_{2(ads)}$ before evolving a free hydrogen molecule [87, 88]. In the case of a hydride attack, $H_{2(ads)}$ is directly formed and released without a preceding cleavage of H from the CH_3-group. For the tantalum cation, DFT calculations by *Parke* et al. showed that the hydride attack in energetically favored [88].

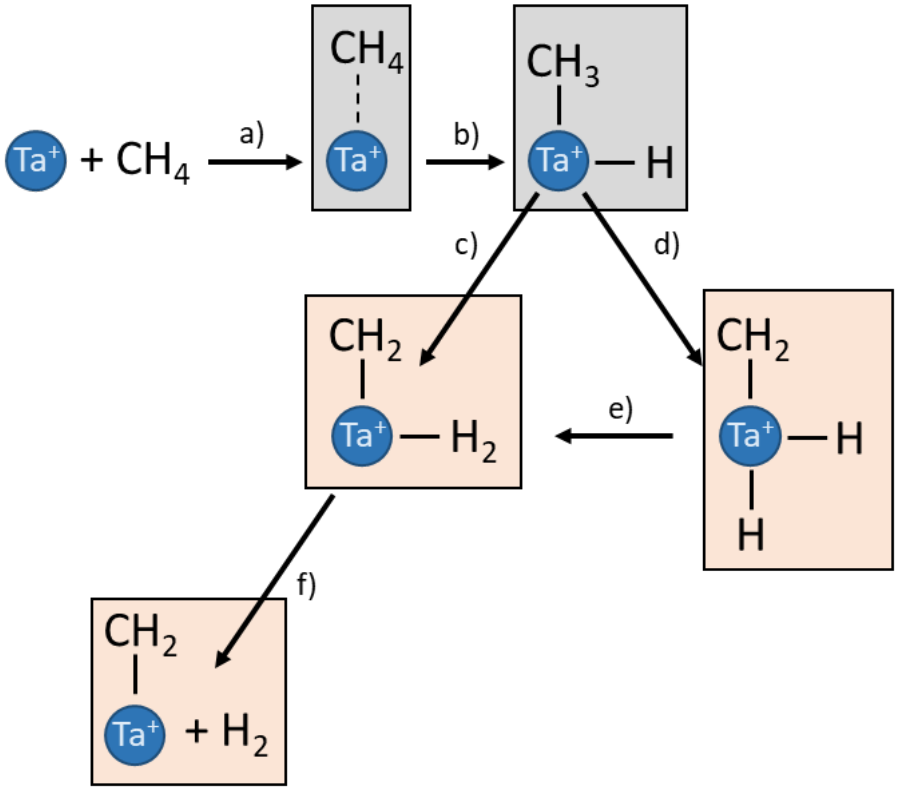

Figure 16: The stepwise activation of CH_4 on Ta^+ follows the mechanism of a metal insertion. In a first step (a), methane adsorbs to the cation, after which Ta^+ inserts into the C−H bond (b), resulting in its cleavage. This hydride can then either attack another hydrogen atom of the formed CH_3-moiety, resulting in the formation of H_2 (c), or the tantalum cation can insert again into a second C−H bond (d). Thereby, dihydrogen is formed once both hydrides interact with each other (e), after which H_2 can desorb from the cation (f), leaving behind a cationic tantalum carbene. Taken from [14].

A similar reaction mechanism was observed for larger tantalum clusters. Here, reactivity decreases as cluster size increases and vanishes at Ta_5^+ [5]. By oxidizing these cationic tantalum clusters, the reactivity can be altered. E.g., for the nonreactive Ta_5^+, oxidation leads to the highly reactive Ta_5O^+, which enables methane dehydrogenation [5]. Additional reaction pathways in the reactivity with methane are obtained for other tantalum species. For example, when the Ta^+ cation is oxidized to TaO_3^+, reaction schemes leading to the formation of neutral products with formaldehyde and methanol stoichiometry occur [89]. For these low oxidation states, it was shown by *Li* et al. that the oxygen atoms modify the σ-orbitals of the metal bonds, but do not actively take part in the reaction itself [90], as it has also been reported previously [5]. With the right oxidation of the cluster, a catalytic behavior can be achieved, which was shown by *Levin* et al. for $Ta_2O_8^+$ [7]. There, two methane molecules are combined, releasing hydrogen and ethane. These examples show that by changing the cluster size and degree of oxidation, the reactivity toward methane can be influenced and optimized for a certain application. The goal of these gas phase studies is to elucidate the origin of the specific reactivity, which will be discussed within more detail when evaluating the reactivity of different oxidation states of $Ta_2O_x^+$ clusters ($0 \leq x \leq 6$) in Section 5.

4.2 Reactivity with Ammonia

While ammonia is seen as a promising candidate for an alternative fuel that only releases harmless N_2 as a by-product of H_2 evolution, ammonia itself is highly toxic to the environment, especially to aquatic life. Therefore, in order to be able to use ammonia as a carbon-free energy source, research is focusing on an efficient way of converting ammonia into non-toxic substances. This opens the field of ammonia slip catalysis (= converting any ammonia "slipping" by the actual catalyst used for H_2 evolution). In this conversion of ammonia, NH_3 can be oxidized to N_2, N_2O and NO_x, depending on the pathway [91]. While N_2 does not pollute the environment and should be produced selectively when using ammonia as a fuel source [92], a high selectivity toward NO could be advantageous for synthetic purposes [93]. For an efficient ammonia slip catalyst, an effective activation of the NH_3 molecule is necessary. On atomic cations throughout the periodic table, it has been observed that this activation comes in the form of an imine formation and is the predominant process for the interaction of

early transition metals with the first ammonia molecule. It is found that the probability of imine formation increases for heavier elements within a group [94, 95]. The other option, shown in Figure 17, is the ligation of NH_3, which does not necessarily lead to an activation of the molecule. This is also referred to as molecular adsorption.

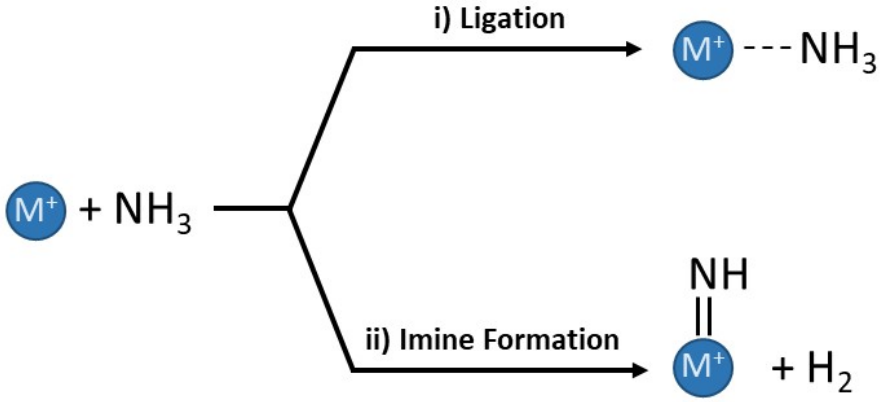

Figure 17: Possible interactions of NH_3 with metal cations. i) shows the ligation of NH_3, while ii) involves the activation of the molecule via imine formation. This results in the release of H_2. Taken from [14].

As for the activation of methane, cationic tantalum ions and clusters have been reported to activate ammonia [96]. For the tantalum cation, two NH_3 molecules are activated before the ligation regime is entered. In clusters, the amount of activated NH_3 molecules depends on the size of the cluster and the charge state. Since the electrons of NH_3 preferentially interact with the d-orbitals of the cluster, reactivity slows down once these are filled. Electrons from the lone pair of additional NH_3 molecules can then bind to the p-orbitals of the metal cluster. After this, further NH_3 molecules can only adsorb on the cluster [94, 97]. Mechanistically, the N−H bond cleavage and hydrogen formation take place analogously to the methane activation process [94, 96]. This results in the formation of an imine on the cluster [98]. However, when interacting with further NH_3 molecules, an additional H_2 evolution can take place by cleaving the residual N−H bonds of the imine groups, releasing hydrogen and forming dinitrides [96]. The type of the final product of the interaction with NH_3 therefore depends on the amount of NH_3 molecules present, as it is shown in Figure 18.

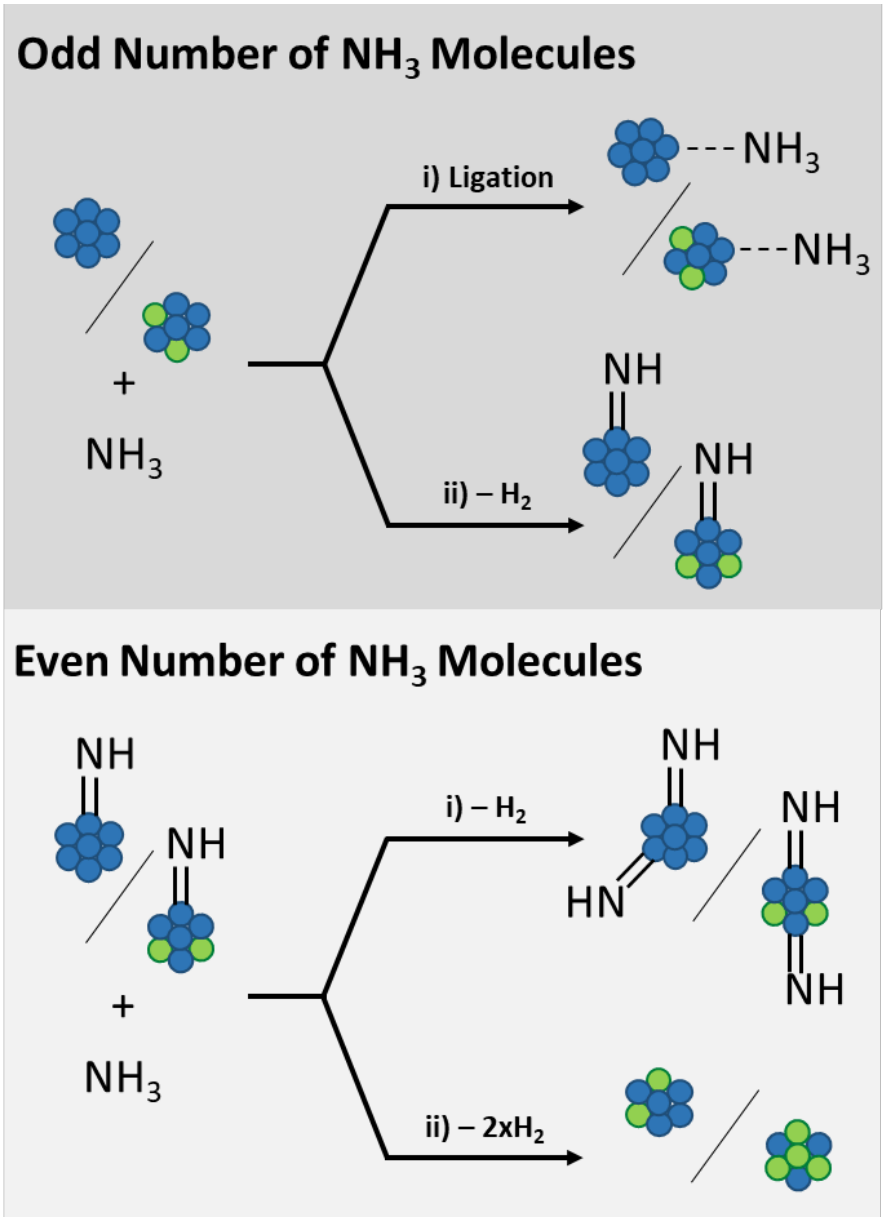

Figure 18: Possible pathways in the reaction of NH_3 with tantalum clusters. In general, ammonia can either adsorb molecularly (i) ligation) or be activated. When an activation takes place, the formed product depends on the amount of NH_3 molecules present. An odd number of NH_3 molecules can only evolve one hydrogen molecule per ammonia molecule and results in an imine formation. An additional H_2 molecule can be released with an even number of NH_3 molecules. This results in the formation of dinitrides. Tantalum atoms are given in blue, nitrogen atoms in green. Taken from [14].

Recent studies of more realistic systems have shown that platinum is a prominent metal used for the conversion of ammonia to different nitrous compounds [9, 99]. Thereby, platinum is deposited on alumina- and zeolite supports. Due to the complexity of these systems, knowledge about the active sites is however missing. Again, studies of model systems can help gaining a fundamental understanding of the activation process. Theoretical analysis of possible adsorption processes was performed by *Daramola* and *Botte* [11, 12]. While *Koszinowski* et al. have performed first gas phase experiments of the platinum cation and cationic clusters in the interaction with NH_3 under single-collision conditions [13], reactivity under multi-collision conditions has not been investigated thoroughly yet. To further elucidate this system, preliminary studies on the adsorption properties of ammonia on platinum clusters under multi-collision conditions have been performed within this dissertation and are discussed in Section 6.

4.3 Reactivity with Nitrogen

The activation of nitrogen is of particular interest for efficient ammonia production, which has to be achieved in order to use ammonia as an alternative fuel [100]. Again, the interaction of a catalyst with nitrogen can take place via two different pathways. Either nitrogen adsorbs molecularly to the catalyst or an activation takes place. Small tantalum clusters have been shown to activate nitrogen by cleaving the strong N≡N triple bond to form dinitrides (see Figure 19) [101, 102]. However, for clusters consisting of more than four tantalum atoms, solely molecular adsorption takes place [103]. Nitrides and dinitrides (e.g., Ta_2N^+ and $Ta_4N_2^+$) can activate further N_2 molecules [102, 104]. *Geng* et al. went one step further toward the synthesis of ammonia by first activating N_2 on the tantalum cation and Ta_2^+ clusters [105]. These activated species should then further interacted with H_2. Theory thereby outlines how the formation of NH_3 may occur in a possible catalytic reaction pathway. However, this has not been tested in experiments yet.

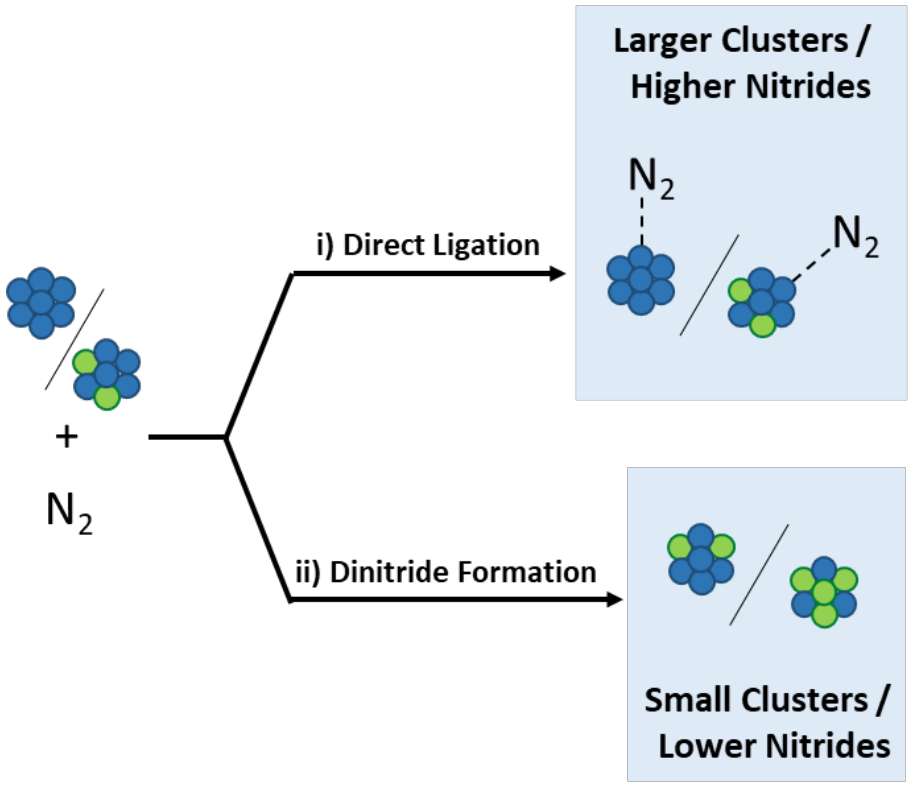

Figure 19: The interaction of cationic tantalum clusters with N_2 depends on the cluster size. While small clusters activate the N≡N triple bond, leading to its cleavage and the formation of dinitrides, molecular adsorption takes place on larger clusters. Tantalum atoms are given in blue, nitrogen atoms in green. Taken from [14].

5 Reactivity of $Ta_2O_x^+$ ($0 \leq x \leq 6$) Clusters with Methane [15]

The data presented in this section was recorded by *Jan F. Eckhard*, but has been re-evaluated and supplemented by DFT calculations during the course of this thesis. This chapter gives a general overview of the reactivity of $Ta_2O_x^+$ ($0 \leq x \leq 6$) clusters toward methane. A more detailed discussion can be found in our published article [15].

As also for other cluster sizes (Ta_x^+, x = 2 - 5) [90], the reactivity of Ta_2^+ clusters toward methane is dependent on the oxidation degree of the cluster species. In Figure 20, the reaction products from the interaction of $Ta_2O_x^+$ ($0 \leq x \leq 6$) with CH_4 are shown. Looking at the mass spectra in Figure 20, one can distinguish (besides the absence of any reactivity on Ta_2O^+) between three different scenarios. For species with low oxidation states, namely Ta_2^+ and $Ta_2O_2^+$, the dehydrogenation of methane is observed, resulting in the addition of one CH_2-moiety on Ta_2^+ and up to two CH_2-moieties on $Ta_2O_2^+$. For $Ta_2O_x^+$ with x = 3, 4, and 6, no activation of methane takes place and CH_4 adsorbs molecularly to the cluster. $Ta_2O_5^+$ is a special case, as the transfer of a single hydrogen atom can be seen on this species uniquely. *Li* et al. have determined the rate coefficients of the interaction of the first methane molecule with $Ta_2O_x^+$ (x = 0 – 4), which are listed in Table 1 together with the respective values determined in our setup [90]. Since the type of reaction and the rate coefficients agree well despite different experimental setups, it demonstrates the reproducibility of the data we obtained from our ion trap studies.

Since Ta_2^+ has already been thoroughly studied in literature [6, 90] and the activation of molecules such as methane, rather than their molecular adsorption, is of particular importance (see Section 4), this work focuses on the differences in reactivity between $Ta_2O_2^+$ and $Ta_2O_5^+$. The reaction behavior of $Ta_2O_5^+$, which is unique among tantalum compounds and exhibits the ability to perform HAT reactions, is of particular interest. Moreover, the interaction of $Ta_2O_2^+$ with the second methane molecule is investigated thoroughly, which has not been reported prior to this study [15].

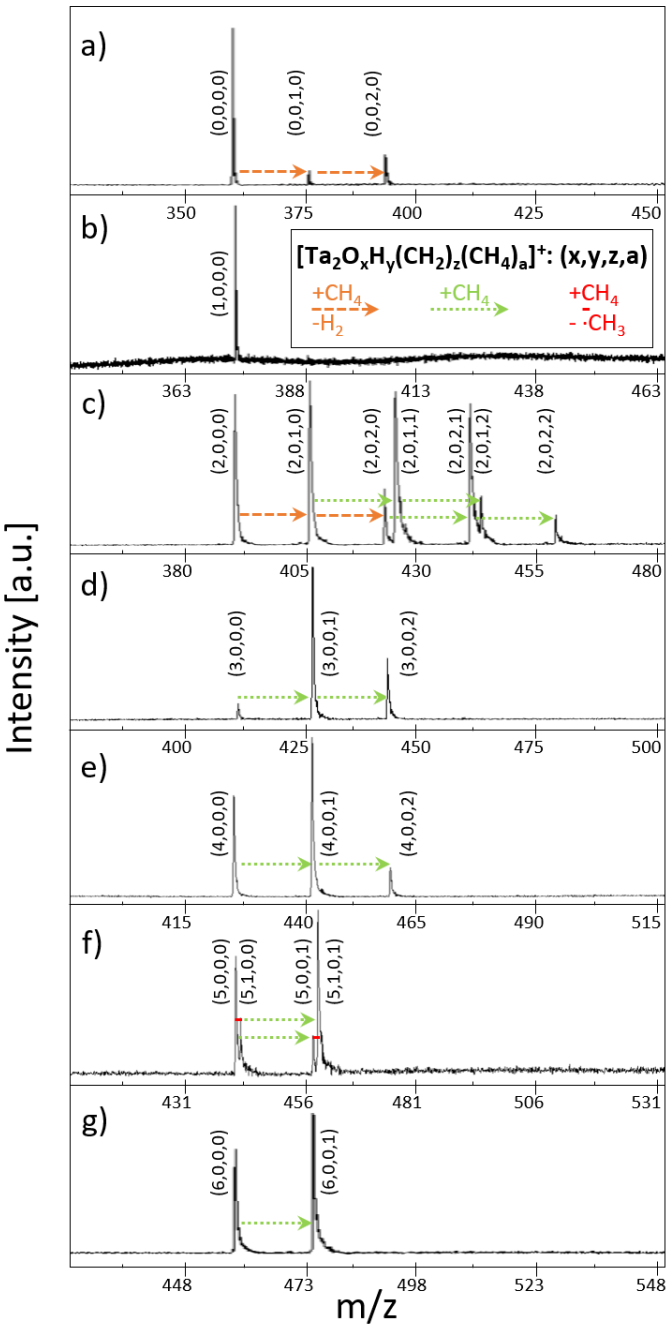

Figure 20: Mass spectra of the products in the reaction of $Ta_2O_x^+$ with CH_4. The number of oxygen atoms increases from (a) x = 0 to (g) x = 6. The dashed orange arrows indicate the addition of CH_2 (m/z = 14), the green dotted arrows show the addition of CH_4 (m/z = 16), and the solid red lines denote the addition of a single hydrogen atom (m/z = 1). While for Ta_2^+ dehydrogenation is observed and Ta_2O^+ does not show any reactivity at all, $Ta_2O_2^+$ exhibits both, the dehydrogenation and molecular adsorption of methane. The latter also occurs for $Ta_2O_x^+$ (x = 3, 4, and 6). $Ta_2O_5^+$ reveals a peculiar behavior, showing the addition of a single hydrogen atom. Taken and modified from [15].

Table 1: Monomolecular rate coefficients $k^{(1)}$, given in s^{-1}, and their respective bimolecular rate coefficients $k^{(2)}$, given in $10^{-11}cm^3s^{-1}$, for the interaction of the respective tantalum oxide cluster with the first methane molecule. For sake of clarity, free reactants and products are not explicitly mentioned in the reaction equation. If available, literature values taken from [90] are listed.

Reaction	$k_+^{(1)}$	$k_+^{(2)}$	$k_{+,Lit}^{(2)}$
$Ta_2^+ \rightarrow Ta_2(CH_2)^+$	7.66 ± 0.08	1.69 ± 0.34	1.1
$Ta_2O^+ \rightarrow Ta_2O(CH_2)^+$	No Reaction	No Reaction	0.0032
$Ta_2O_2^+ \rightarrow Ta_2O_2(CH_2)^+$	79.2 ± 4.9	24.5 ± 5.2	22
$Ta_2O_3^+ \rightarrow Ta_2O_3(CH_4)^+$	89.1 ± 0.3	54.3 ± 10.9	82
$Ta_2O_4^+ \rightarrow Ta_2O_4(CH_4)^+$	107 ± 1	13.2 ± 2.7	27
$Ta_2O_5^+ \rightarrow Ta_2O_5H^+$	102 ± 15	55.7 ± 13.8	-
$Ta_2O_5^+ \rightarrow Ta_2O_5(CH_4)^+$	55.3 ± 13.4	30.1 ± 9.4	-
$Ta_2O_6^+ \rightarrow Ta_2O_6(CH_4)^+$	52.0 ± 0.6	32.5 ± 6.5	-

5.1 Methane Dehydrogenation on $Ta_2O_2^+$

For $Ta_2O_2^+$, the mass spectra show the pure metal oxide cluster $Ta_2O_2^+$ (m/z = 394), the reaction product after one dehydrogenation reaction $Ta_2O_2(CH_2)^+$ (m/z = 408), after two dehydrogenation reactions $Ta_2O_2(CH_2)_2^+$ (m/z = 422) and the products of potential molecular adsorptions $Ta_2O_2(CH_2)(CH_4)^+$ (m/z = 410), $Ta_2O_2(CH_2)_2(CH_4)^+$ (m/z = 424), $Ta_2O_2(CH_2)(CH_4)_2^+$ (m/z = 440), and $Ta_2O_2(CH_2)_2(CH_4)_2^+$ (m/z = 454). As mentioned in Section 3.2, mass spectra recorded after varying reaction times are analyzed by integrating peaks to determine the respective abundance of species present. Different chemically plausible reaction models are tested to obtain a model that accurately describes the measured time dependence of all species. The best model, along with its respective fit, is shown in Figure 21.

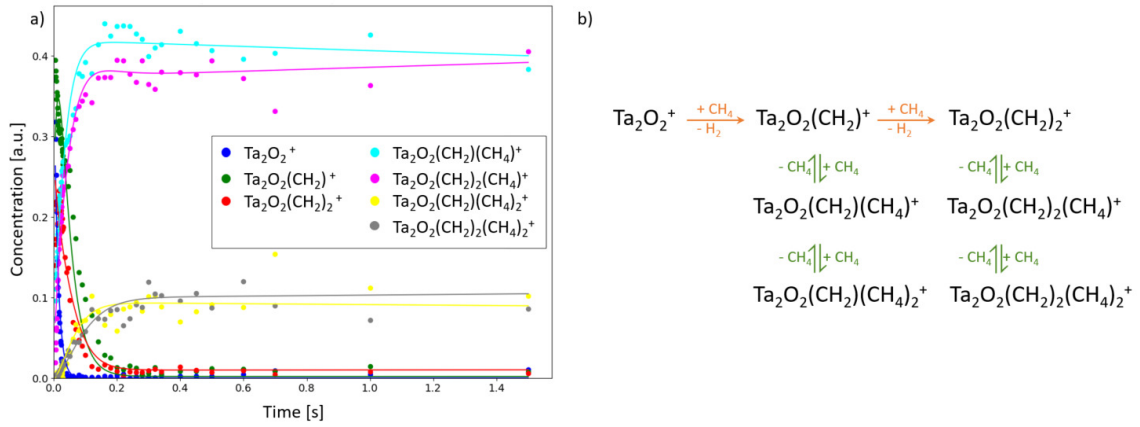

Figure 21: a) Fits obtained by kinetic simulations (lines) in comparison to the respective measured data points (dots) dependent on the storage time. b) Used model for the fits shown in a), which gives rise to the most accurate fits while being chemically plausible and as simple as possible. Molecular adsorption reactions are marked in orange, dehydrogenation steps in green. Taken and modified from [15].

It is assumed that all dehydrogenation reactions are irreversible, since the probability of the as-released hydrogen and the resulting cluster colliding again is negligibly small. From the obtained reaction models, monomolecular rate coefficients can be extracted. In order to be able to compare these values, rate coefficients are normalized to the particle density of methane. The resulting bimolecular rate coefficient is defined as:

$$k^{(1)} = k^{(2)} \cdot [CH_4] \tag{5}$$

with [CH_4] being the concentration of methane. All determined rate constants for the first two methane dehydrogenation reactions are listed in Table 2.

Table 2: Monomolecular rate coefficients, given in s^{-1}, and their respective bimolecular rate coefficients, given in $10^{-11}cm^3s^{-1}$, for the first two methane dehydrogenation reactions on $Ta_2O_2^+$ (denoted as M^+).

Reaction	$k^{(1)}_{+,CH4}$	$k^{(2)}_{+,CH4}$	$k^{(1)}_{+,CD4}$	$k^{(2)}_{+,CD4}$
$M^+ \rightarrow M(CH_2)^+$	79.2 ± 4.9	24.5 ± 5.2	26.8 ± 0.5	3.71 ± 0.75
$M(CH_2)^+ \rightarrow M(CH_2)_2^+$	8.51 ± 0.68	2.62 ± 0.57	3.35 ± 0.19	0.465 ± 0.097

It is worth noting that no $Ta_2O_2(CH_4)^+$ is observed, indicating that the first dehydrogenation reaction occurs very rapidly. As it has been reported for other systems investigated using the same setup (e.g., the oxidation of small tantalum(-oxide) cations [106] or the reaction of tantalum cations with CO_2 [107]), the stabilization of intermediates or reaction products by collisions with the He buffer gas is sometimes not fast enough so that the formation of thermodynamically less stable reaction products is favored in some cases. Furthermore, this may lead to a progression of the reaction without the possibility to detect reaction intermediates. In the present system, it is believed that the second dehydrogenation reaction also proceeds without the possibility of detecting the respective intermediate. Although $Ta_2O_2(CH_2)(CH_4)^+$ is indeed observed, including this species in the kinetic reaction model as an intermediate to the fully dehydrogenated $Ta_2O_2(CH_2)_2^+$ does not improve the quality of the fits significantly. Moreover, the fit deteriorates drastically when molecular adsorption on the cluster is removed. In contrast, it is assumed that $Ta_2O_2(CH_2)(CH_4)^+$ originates from intact CH_4 adsorption on the metal-oxide. This system was further investigated using DFT calculations. After the first dehydrogenation process, two separate reaction sites are present. Depending on which side the second methane molecule approaches from, either a second dehydrogenation or molecular adsorption takes place. Once molecular adsorption occurred, the methane molecule may then prevent the reconstruction of the species to form the CH_2 bridges necessary to provide a driving force for the dehydrogenation reaction. Therefore, no further methane dehydrogenation is observed once the addition of molecular methane has started. Moreover, a dehydrogenation of the methane molecule adsorbed to the adsorption site would include a transition state with an energy barrier of 0.44 eV above the entrance channel, which is unlikely to be overcome at room temperature (see Figure 22).

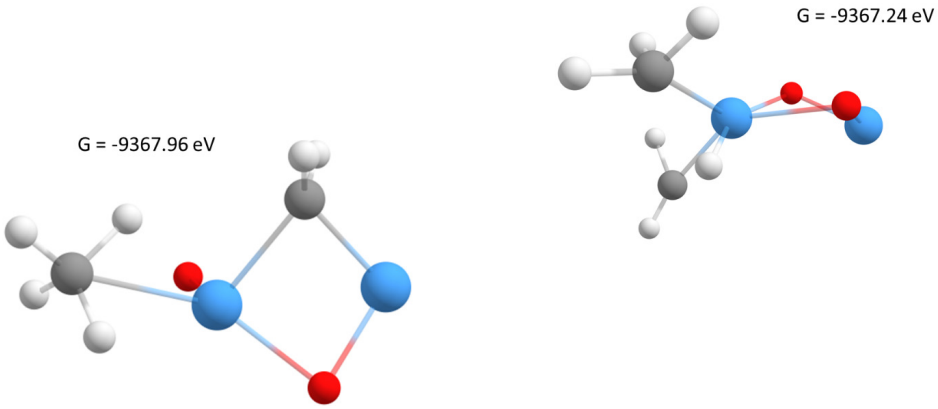

Figure 22: The adsorption of a methane molecule on $Ta_2O_2(CH_2)^+$ on the tantalum atom connected to two oxygen atoms (left) does not lead to the evolution of H_2, since during this reaction, a transition state (right) 0.72 eV over the adsorbed species (or 0.44 eV above the entrance channel) would have to be overcome. Taken from [15].

Due to the resulting steric hindrance, no further methane molecules can adsorb without quenching the dehydrogenation reaction before hydrogen can be evolved. Therefore, $Ta_2O_2(CH_2)(CH_4)^+$, $Ta_2O_2(CH_2)_2(CH_4)^+$, and $Ta_2O_2(CH_2)_2(CH_4)_2^+$ are only generated by consecutive molecular adsorption reactions on $Ta_2O_2(CH_2)_2^+$ and not due to dehydrogenation reactions on $Ta_2O_2(CH_2)(CH_4)^+$, and $Ta_2O_2(CH_2)(CH_4)_2^+$. This is consistent with the obtained kinetic models, in which the best fits are obtained with negligibly small rate coefficients for reactions in which the CH_4-adducts represent intermediates of the dehydrogenation reactions, as shown in Figure 23.

To gain additional insights into the underlying reaction mechanism, DFT calculations have been performed. In a first step, the structures of the metal oxide clusters are determined, which is shown in Figure 24. The calculated ground state structure is in good agreement with the literature reference published by *Li* et al. [90]. For this metal oxide cluster, as well as all transition states, intermediates and the final product, the doublet spin state proves to be the most stable multiplicity, while also the quartet and the sextet state have been tested. As a next step, methane is added to the cluster. Since $Ta_2O_2^+$ is symmetrical, the direction from which the first methane molecule approaches is insignificant and the probability of the interaction with methane is the same for both tantalum atoms. After adsorbing to the cluster, whereby the carbon atom of methane interacts with one tantalum atom, the first C−H bond is cleaved via a classical metal insertion. While the adsorption is exothermic with an energy gain of

a)

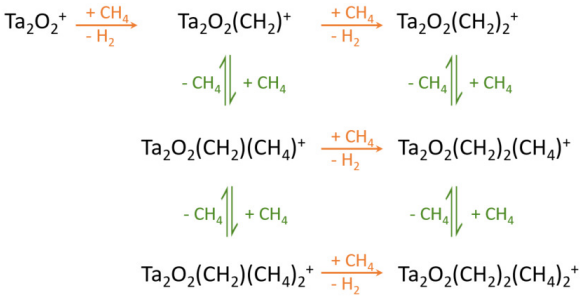

b)

Reaction	$k_+^{(1)}$	$k_-^{(1)}$	K
$Ta_2O_2^+ \rightarrow Ta_2O_2(CH_2)^+$	80.8 ± 5.0	-	-
$Ta_2O_2(CH_2)^+ \rightarrow Ta_2O_2(CH_2)_2^+$	8.86 ± 1.95	-	-
$Ta_2O_2(CH_2)^+ \leftrightarrow Ta_2O_2(CH_2)(CH_4)^+$	21.7 ± 2.0	0.506 ± 0.401	42.9
$Ta_2O_2(CH_2)_2^+ \leftrightarrow Ta_2O_2(CH_2)_2(CH_4)^+$	34.6 ± 3.2	1.14 ± 0.52	30.2
$Ta_2O_2(CH_2)(CH_4)^+ \rightarrow Ta_2O_2(CH_2)_2(CH_4)^+$	0.00 ± 2.38	-	-
$Ta_2O_2(CH_2)^+ \leftrightarrow Ta_2O_2(CH_2)(CH_4)_2^+$	7.13 ± 2.22	33.1 ± 17.3	0.22
$Ta_2O_2(CH_2)_2^+ \leftrightarrow Ta_2O_2(CH_2)_2(CH_4)_2^+$	5.37 ± 1.90	20.6 ± 8.4	0.3
$Ta_2O_2(CH_2)_2(CH_4)^+ \rightarrow Ta_2O_2(CH_2)_2(CH_4)_2^+$	0.0 ± 10.8	-	-

Figure 23: Alternative reaction mechanism tested, where dehydrogenation reactions can also take place once molecular adsorption has started. This reaction model does not increase the fit accuracy significantly and the rate coefficients (shown in b) of these dehydrogenation reactions are negligibly small. Taken and modified from [15].

about 0.30 eV, the transition state of the bond cleavage is in the energy range of the entrance channel with an energy of +0.02 eV in comparison to the bare metal-oxide cluster and a free methane molecule. After relaxation of the first transition state, the thermodynamically most stable intermediate is formed, resulting in an energy gain of 1.06 eV. However, since this species has not been detected in the experiments, it is assumed that this large free energy cannot be transferred fast enough to the He buffer gas via collisions. This results in a fast progress of the reaction. For the cleavage of the second C−H bond, two different options arise, which have already been discussed within Section 4 and can be seen in Figure 16 for the general case. In the first pathway, another mechanistically identical metal insertion takes place. The two hydrogen atoms, independently bound to the tantalum atom, can then recombine and desorb as molecular hydrogen. This metal insertion, however, involves a transition state 0.30 eV higher than the entrance channel, which is unlikely to be overcome at room temperature [6]. The second pathway involves the attack of the as-formed hydride directly on a hydrogen atom of the methyl group, forming adsorbed hydrogen, which can be evolved in a consecutive reaction step. This pathway is energetically favored over the first one with a transition state below the entrance channel. For the tantalum cation, this effect is even more pronounced, as it was reported by *Parke* et al. [88].

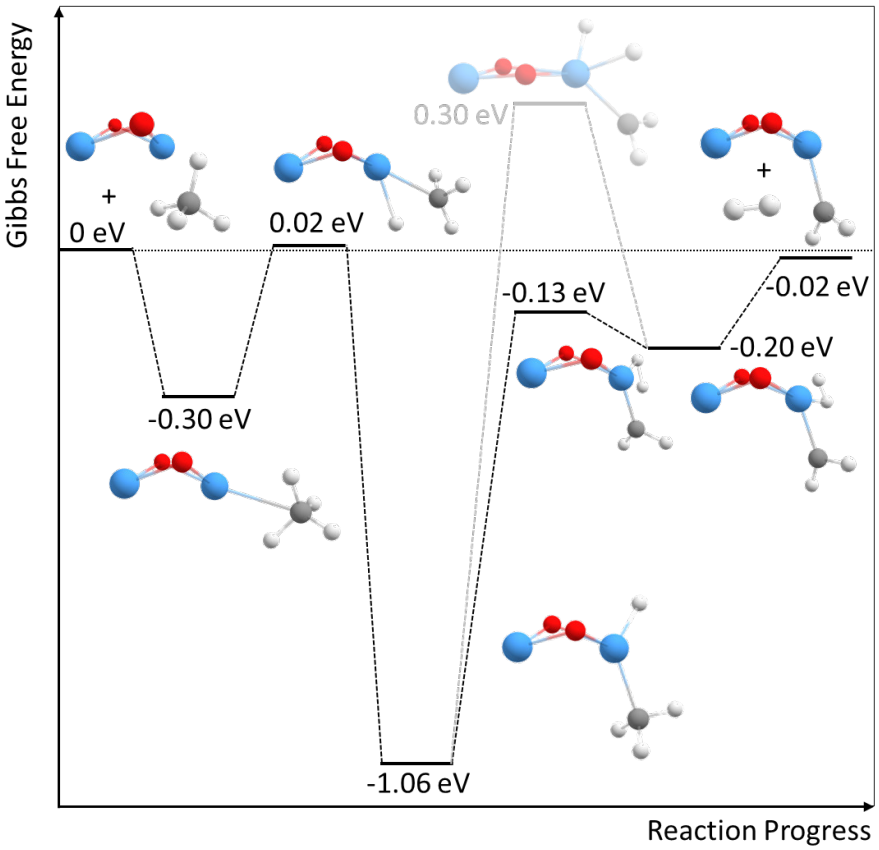

Figure 24: Normalized *Gibbs* free energy given for the reaction of $Ta_2O_2^+$ with methane (*Gibbs* free energies calculated for T = 298.15 K and p = 1 atm; $Ta_2O_2^+$ and a free methane molecule are defined as 0 eV). The transition state obtained by performing a metal insertion into the second C−H bond, leading to a higher energy in comparison to the hydride attack, is grayed-out. Tantalum atoms are shown in blue, oxygen atoms in red, carbon atoms in gray and hydrogen atoms in white. Taken from [15].

The final product $Ta_2O_2(CH_2)^+$ is isoenergetic to the reactant species in its unbridged form. However, by transforming intramolecularly as shown in Figure 25, a CH_2 bridge can be created, resulting in an energy gain of around 0.42 eV. The formation of this CH_2 bridge can supply one of the driving forces of the reaction.

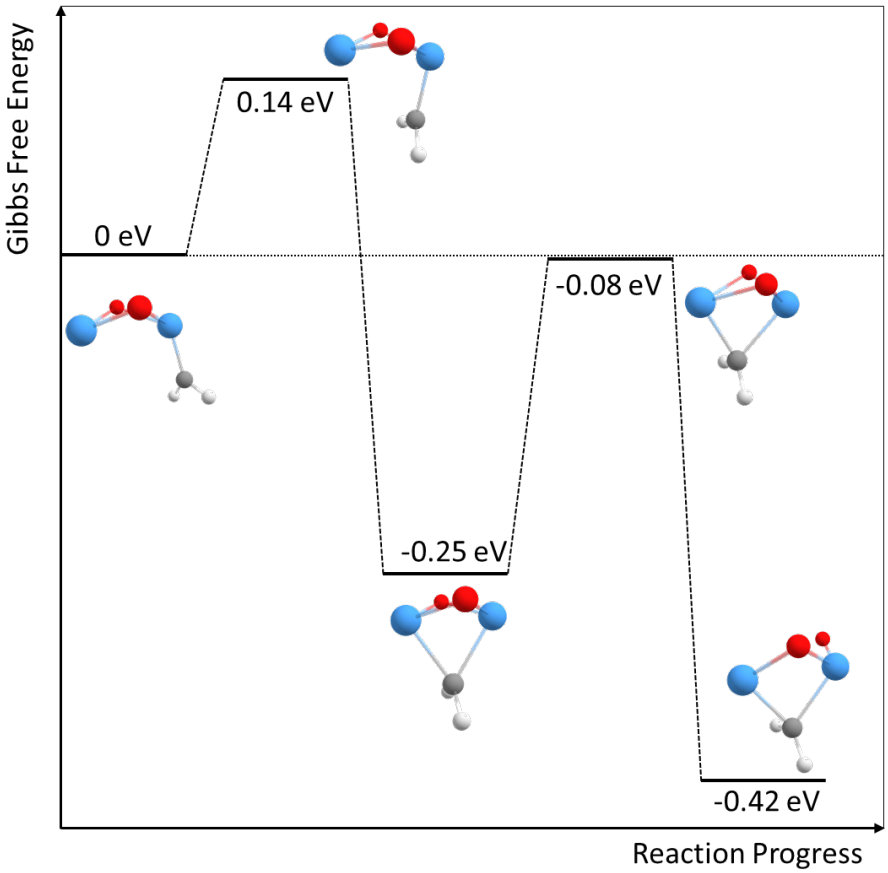

Figure 25: Normalized *Gibbs* free energies during the course of the formation of CH_2 bridges on $Ta_2O_2(CH_2)^+$ (*Gibbs* free energies calculated for T = 298.15 K and p = 1 atm; $Ta_2O_2(CH_2)^+$ in its unbridged form is defined as 0 eV). The most stable configuration involves the opening of an oxygen bridge and results in a compound 0.42 eV more stable than the initial $Ta_2O_2(CH_2)^+$. Tantalum atoms are shown in blue, oxygen atoms in red, carbon atoms in gray and hydrogen atoms in white. Taken from [15].

With these three possible reaction isomers, a multitude of interaction possibilities with the second methane molecule arises. In general, it can be said that structures exhibiting CH_2 bridging motifs are energetically more favored than the isomeric unbridged species. While all three structures can serve as reactive intermediates due to the small differences in energy, only the bridged isomer will yield the final dicarbene, since the potential energies diverge as the reaction progresses (see Figure 26).

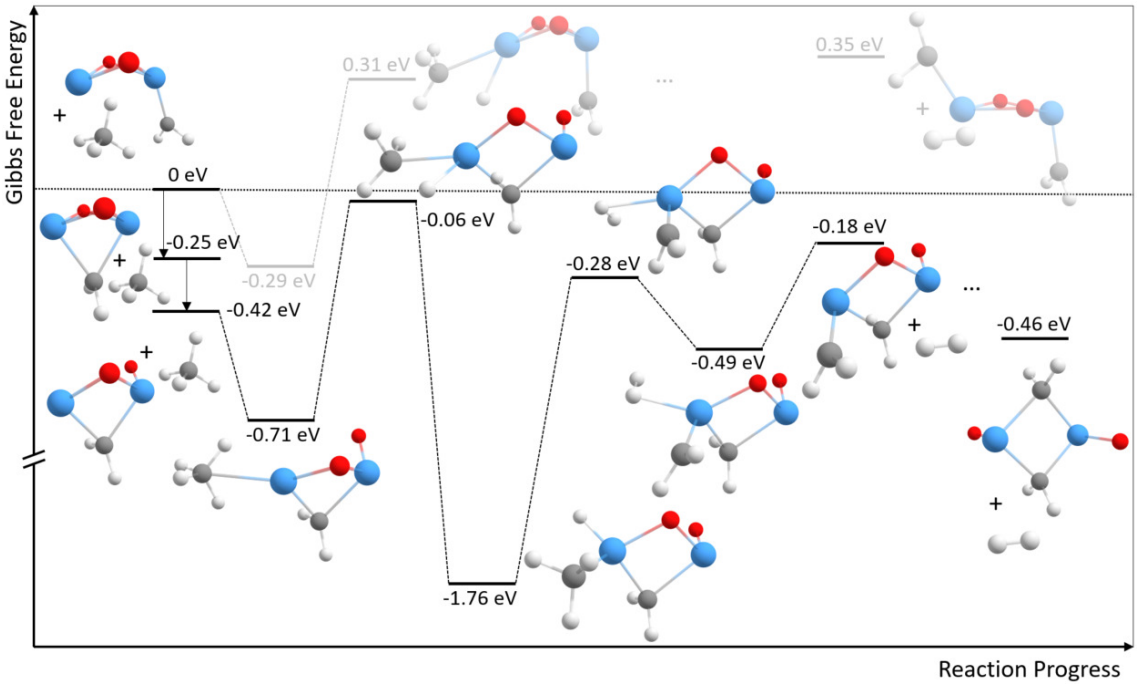

Figure 26: Normalized *Gibbs* free energies during the second dehydrogenation of methane (*Gibbs* free energies calculated for T = 298.15 K and p = 1 atm; unbridged $Ta_2O_2(CH_2)^+$) and a free methane molecule are defined as 0 eV). Reaction pathways including transition states and final products too high in energy to occur at room temperature are grayed-out. Tantalum atoms are shown in blue, oxygen atoms in red, carbon atoms in gray and hydrogen atoms in white. Taken from [15].

The activation of the second methane molecule takes place analogously to the first one. After the initial C−H bond cleavage due to metal insertion of the tantalum atom, the as-formed hydride attacks a hydrogen atom of the CH_3-moiety to form $H_{2,ads}$, which can desorb consecutively. As shown in Figure 27, energies for these reaction steps are in the same range as for the first dehydrogenation, with no transition states above the entrance channel in the case of unbridged $Ta_2O_2(CH_2)^+$. However, the rate coefficient of the second dehydrogenation is by an order of ten times smaller in comparison to the first one, which can be seen in Table 2.

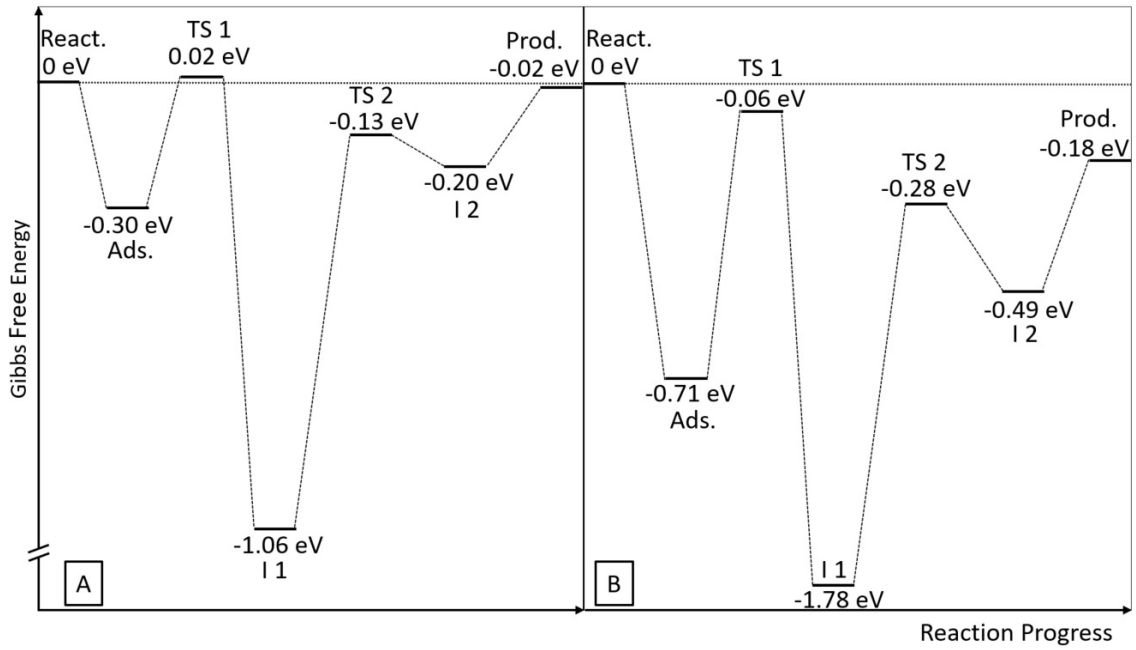

Figure 27: Comparison of the present normalized *Gibbs* free energies in the first (A) and second (B) dehydrogenation reaction of methane (*Gibbs* free energies calculated for T = 298.15 K and p = 1 atm; the respective reactants have been defined as 0 eV). Taken from [15].

As mentioned before, a transition from this unbridged state into a bridged isomer is necessary for the reaction to proceed, which might slow down the overall process. In contrast to that, when starting from the already bridged $Ta_2O_2(CH_2)^+$ compound, higher reaction barriers are present, further explaining the smaller rate coefficient. The final, unbridged $Ta_2O_2(CH_2)_2^+$ can thereafter be transformed analogously to $Ta_2O_2(CH_2)^+$ into its bridged form, resulting in an exergonic reaction and, again, representing the driving force of the dehydrogenation. As it can be seen in Figure 26, both oxygen bridges are now cleaved and replaced by CH_2 bridging motifs. Since our calculations show that these CH_2-moieties do not interact with each other and no $C-C$ bond formation can be observed (candidate structures shown in Figure 28 are in the range of 0.54 - 0.87 eV higher in energy), this bridged $Ta_2O_2(CH_2)_2^+$ isomer is most probably the final product of the dehydrogenation reactions.

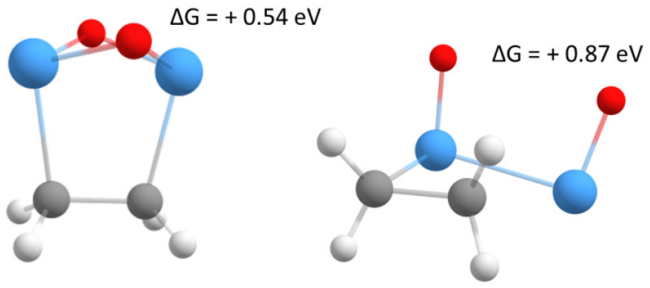

Figure 28: Two examples for candidate structures exhibiting C−C bond formation. The respective *Gibbs* free energy differences to the most stable $Ta_2O_2(CH_2)_2^+$ isomer are given. Tantalum atoms are shown in blue, oxygen atoms in red, carbon atoms in gray and hydrogen atoms in white. Taken from [15].

In this compound, both Ta atoms exhibit an oxidation state of +V and are therefore fully oxidized. Further methane molecules can only adsorb to this species, resulting in energy gains ranging from 0.20 eV to 0.46 eV, which can be seen in Figure 29.

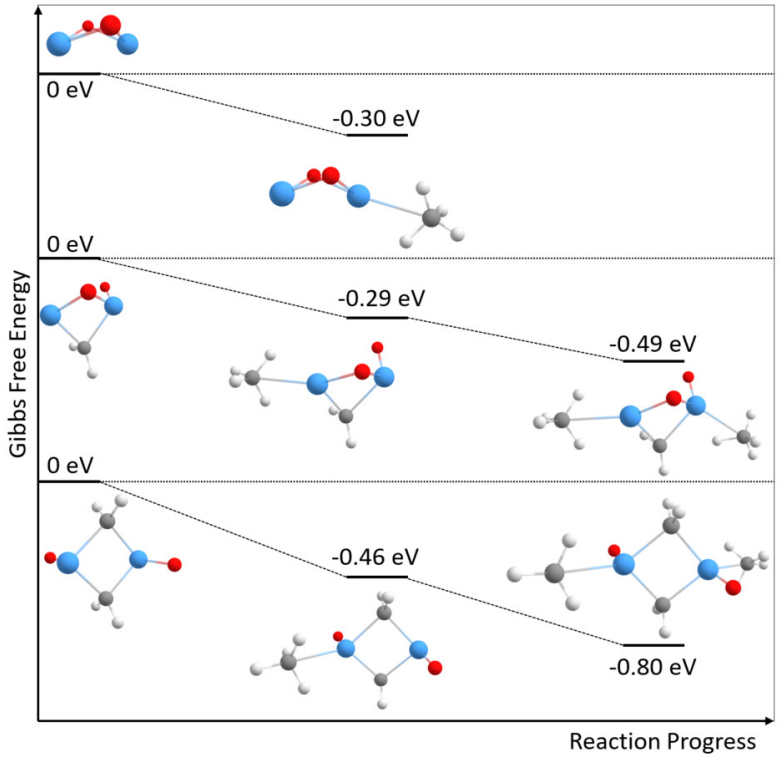

Figure 29: Normalized *Gibbs* free energies of possible adsorption reactions on different species occurring in the reactions of methane on $Ta_2O_2^+$ clusters (*Gibbs* free energies are calculated for T = 298.15 K and p = 1 atm; the respective tantalum oxide species plus free methane molecules are defined as 0 eV). Tantalum atoms are shown in blue, oxygen atoms in red, carbon atoms in gray and hydrogen atoms in white. Taken and modified from [15].

All experiments were repeated using the isotopically labeled gas CD_4. This guarantees a correct peak assignment. Since e.g., CH_4 and oxygen both have a m/z of 16 amu, their addition cannot be unambiguously disentangled by mass spectrometry. By repeating the experiments with CD_4, the recorded masses shift by m/z of +1 for H $\rightarrow$ D, +2 for $CH_2 \rightarrow CD_2$ and +4 for $CH_4 \rightarrow CD_4$ (see Figure 30), which confirms a correct peak assignment.

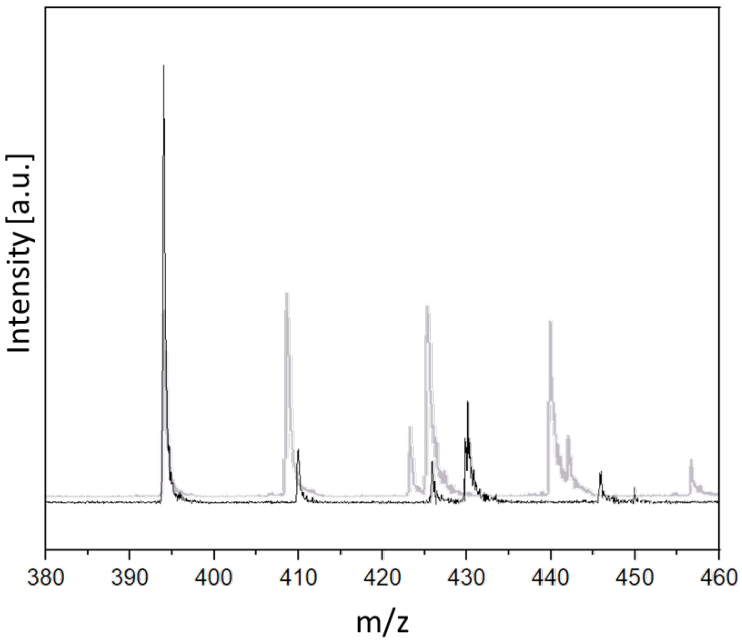

Figure 30: Comparison of the mass spectra recorded after the interaction of $Ta_2O_2^+$ with CH_4 (light gray) and CD_4 (black). The product peaks are shifted to higher m/z according for the reaction with CD_4, allowing for an unambiguous assignment of all species. Taken from [15].

For the rate coefficients, relatively high kinetic isotope effects (KIE) of 5 - 6 are obtained for both methane activation reactions (see Table 3), whereby the KIE is determined as:

$$KIE = 0.9 \cdot \frac{k_{CH4}^{(2)}}{k_{CD4}^{(2)}} \tag{6}$$

The prefactor 0.9 includes the correction for different collision cross sections of the two isotopologues. Calculated high KIE values indicate that the C−H bond cleavage is of importance in the rate-determining step.

Table 3: Bimolecular rate coefficients, given in 10^{-11}cm^{3}s^{-1}, for the first two CH_4/CD_4 dehydrogenation reactions and their respective KIEs.

Reaction	$k^{(2)}_{+,CH4}$	$k^{(2)}_{+,CD4}$	KIE
$Ta_2O_2^+ \rightarrow Ta_2O_2(CH_2)^+$	24.5 ± 5.2	3.71 ± 0.75	5.9 ± 1.7
$Ta_2O_2(CH_2)^+ \rightarrow Ta_2O_2(CH_2)_2^+$	2.62 ± 0.57	0.465 ± 0.097	5.1 ± 2.2

Using DFT, more information about this rate-determining step can be gained. Looking at the energies of the reaction progress shown in Figure 24 and Figure 26, the highest energy barriers have to be overcome during the cleavage of methane's first C−H bond. In order to determine the kinetic isotope effect from the reaction barriers obtained, one has to consider the probability of overcoming these present barriers. Therefore, the *Arrhenius* equation has to be taken into account:

$$KIE = f \cdot \frac{k^{(2)}_{CH4}}{k^{(2)}_{CD4}} = f' \cdot \frac{A_1 e^{-\frac{E_{A,1}}{kT}}}{A_2 e^{-\frac{E_{A,2}}{kT}}} = f' \cdot e^{-\frac{E_{A,1}-E_{A,2}}{kT}} \tag{7}$$

The aforementioned pre-factor f' is known to be 0.9 when comparing CH_4 with CD_4. The *Arrhenius* equation can be further simplified by defining

$$\Delta E_A = E_{A,2} - E_{A,1} \tag{8}$$

Therefore, the KIE can be written as

$$KIE = 0.9 \cdot e^{\frac{\Delta E_A}{kT}} \tag{9}$$

For the first C−H bond cleavage, an energy barrier of 0.021 eV has to be overcome, while for the C−D bond cleavage, this barrier is increased to 0.071 eV. When inserting this energy difference of 0.050 eV into Equation 9, this results in a KIE of 5.3. The C−H bond cleavage of the second dehydrogenation reaction costs 0.016 eV, while the C−D bond cleavage needs an external energy of 0.064 eV. The respective KIE determined for an energy difference of 0.048 eV is 4.8. These values are in very good agreement with the experimentally obtained KIE of 5.9 $\pm$ 1.7 for the first methane dehydrogenation, and 5.1 $\pm$ 2.2 for the second one.

5.2 The Unique Reactivity of $Ta_2O_5^+$ toward Methane

For the tantalum cation and tantalum(-oxide) clusters, the literature has so far reported on the dehydrogenation of methane, which leads to the release of molecular hydrogen and the addition of a CH_2 moiety, as well as on molecular adsorption, where intact CH_4 molecules are added to the cluster [5, 6, 14, 85–90]. When looking at the mass spectra in Figure 20.f, the addition of a single hydrogen atom can be observed besides the molecular adsorption of CH_4. In this process, a free methyl radical is released. The species present are attributed to $Ta_2O_5^+$ (m/z = 442), $Ta_2O_5H^+$ (m/z = 443), $Ta_2O_5CH_4^+$ (m/z = 458) and $Ta_2O_5HCH_4^+$ (m/z = 459). The best model and the respective kinetic fit are shown in Figure 31. As for the dehydrogenation on $Ta_2O_2^+$, it is assumed that the release of the methyl radical takes place irreversibly, while all molecular adsorption steps are modeled reversibly.

Similar to the dehydrogenation reactions referred to above, the molecularly adsorbed methane is not an intermediate of the HAT. Including this additional pathway into the kinetic model does not significantly improve the fit, while the obtained rate coefficient of this reaction approaches zero. This indicates the presence of two independent reaction pathways. Methane can either adsorb molecularly or undergo a HAT reaction.

As it can be seen when comparing the rather similar bimolecular rate coefficients of the two possible HATs listed in Table 4, the two reactions seem to not influence each other significantly. Rather one reaction type can be followed by the respective other one, resulting in the final product $Ta_2O_5HCH_4^+$.

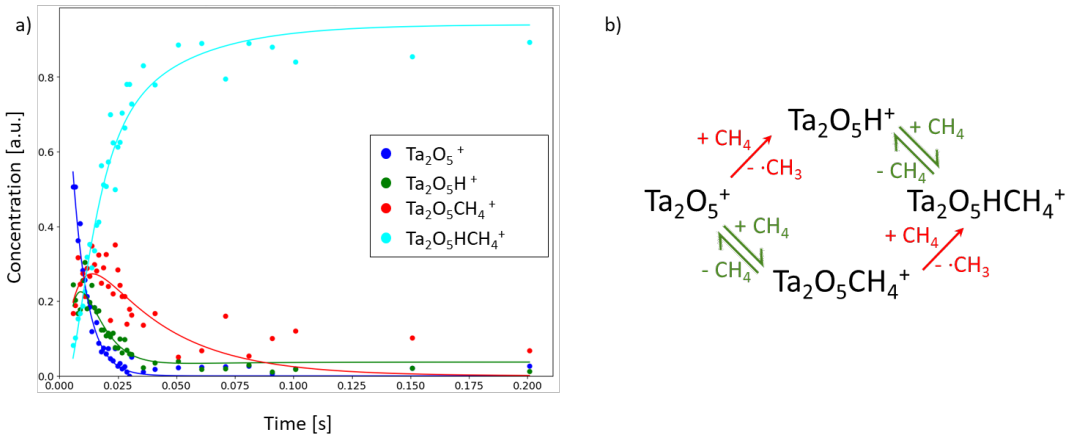

Figure 31: a) Fits obtained by kinetic simulations (lines) in comparison to the respective measured data points (dots) as a function of the storage time. b) Used model for the fits shown in a), which gives rise to the most accurate fits while being chemically plausible and as simple as possible. Molecular adsorption reactions are marked in green, hydrogen atom transfers in red. Taken and modified from [15].

Table 4: Monomolecular rate coefficients, given in s^{-1}, and their respective bimolecular rate coefficients, given in $10^{-10}cm^3s^{-1}$ for the two possible HAT reactions on $Ta_2O_5^+$ (denoted as M^+) and $Ta_2O_5CH_4^+$, respectively. Rate coefficients are given for the interaction with CH_4 and CD_4 and listed together with the KIEs.

Reaction	$k_{+,CH4}^{(1)}$	$k_{+,CH4}^{(2)}$	$k_{+,CD4}^{(1)}$	$k_{+,CD4}^{(2)}$	KIE
$M^+ \rightarrow MH^+$	10.2 ± 1.5	5.5 ± 1.4	2.13 ± 0.28	0.85 ± 0.20	5.9 ± 2.0
$MCH_4^+ \rightarrow MHCH_4^+$	3.05 ± 0.70	1.66 ± 0.50	1.01 ± 0.12	0.401 ± 0.093	3.7 ± 1.4

The experiments were repeated with isotopically labeled gas (i.e., CD_4) to confirm the assignment of the peaks. As shown in Figure 32, substituting H for the heavier isotope D leads to the expected m/z shifts. The product of the HAT can now be seen at m/z +2, the product of molecular adsorption has a m/z +20, and the final product $Ta_2O_5HCH_4^+$ is located at m/z +22. When comparing the rate coefficients for the reaction with CH_4 and CD_4, KIE values in the range of 3.7 - 5.9 are obtained for the HAT reactions (see Table 4). The values are comparable to those of the dehydrogenation reactions on $Ta_2O_2^+$, suggesting that the cleavage of the C−H/C−D bond plays an important role. This goes in line with the assumed HAT mechanism.

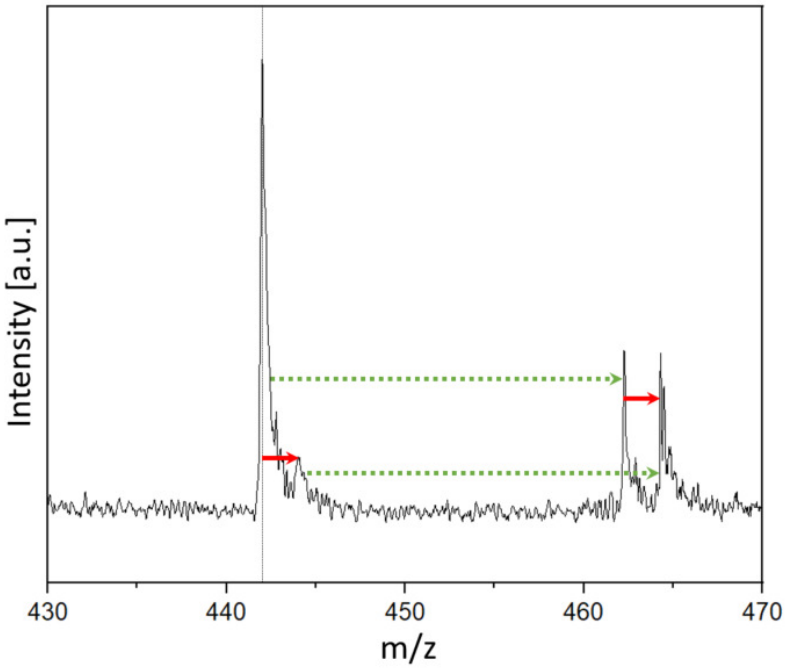

Figure 32: Mass spectrum recorded for the reaction of $Ta_2O_5^+$ with CD_4. The red arrow shows the addition of D with a m/z change of +2. The green dotted arrow shows the molecular adsorption of CD_4 with m/z of +20.

Using DFT, further insight into the underlying reaction behavior can be gained. The cationic $Ta_2O_5^+$ cluster exhibits a similar geometry (shown in Figure 33) as its anionic form [108], also fitting in line with the oxidation behavior for smaller oxides $Ta_2O_x^+$ (with x = 0 - 4) [90]. The doublet state is the most stable multiplicity, while also the quartet and sextet state have been tested. During the molecular adsorption of methane, the multiplicity of the most stable ground state does not change. However, when a single hydrogen atom is added as a radical, the overall parity changes. For these species, namely $Ta_2O_5H^+$ and $Ta_2O_5HCH_4^+$, the singlet state exhibits the lowest *Gibbs* free

energy, while also the triplet and quintet state have been tested. DFT calculations confirm the assumption of two different reaction centers for the two different types of reaction. Since $Ta_2O_5^+$ is not symmetrical, the direction from which methane approaches is important.

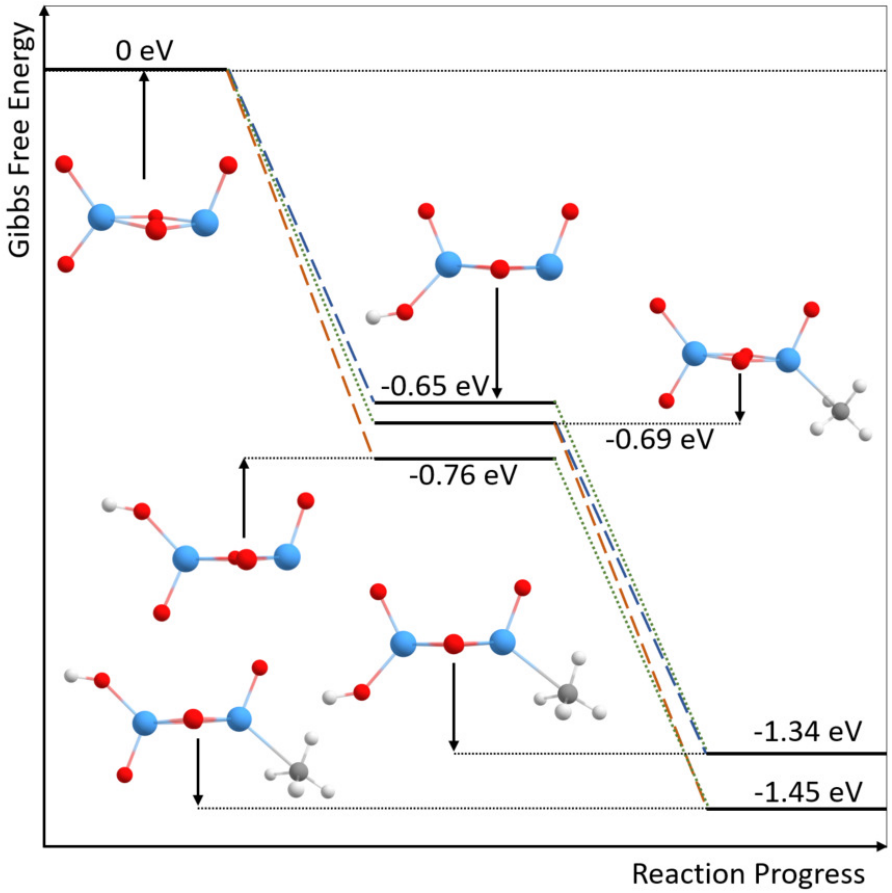

Figure 33: Normalized *Gibbs* free energies for the interaction of $Ta_2O_5^+$ with two methane molecules (*Gibbs* free energies calculated for T = 298.15 K and p = 1 atm; $Ta_2O_5^+$ and two free methane molecules are defined as 0 eV). A methane molecule can either adsorb molecularly (green dotted line) or a hydrogen atom can be transferred to the cluster (dashed lines). The blue dashed line thereby shows the hydrogen transfer to the oxygen in anti-position, the orange dashed line to the one in syn-position. Tantalum atoms are given in blue, oxygen atoms in red, carbon in gray and hydrogen in white. Taken from [15].

Besides the oxygen bridges, one tantalum atom is bound to only one end-on oxygen, the other tantalum atom has two end-on oxygen atoms connected. When the methane atom approaches the tantalum atom with one oxygen ligand, molecular adsorption onto the tantalum atom can occur. In this process, the carbon atom of methane in-

teracts with the tantalum atom. This is a reversible reaction step. When methane approaches the cluster from the other side, the carbon atom cannot interact with the tantalum atom, since the latter is sterically shielded by the two end-on oxygen atoms. Instead, the hydrogen atom of methane interacts with one of the two oxygen atoms. As shown in Figure 33, depending on the oxygen atom to which the hydrogen atom is transferred, an energy gain of 0.65 eV or 0.76 eV is achieved. A higher gain corresponds to the HAT onto the oxygen atom in syn-position. The energy gain of the molecular adsorption is in the same range. For both reaction types, no energy barriers are observed. Because of this, a KIE cannot easily be determined theoretically for the HAT reaction. However, a barrier-free process only occurs when the methane molecule approaches the oxygen atom with its hydrogen atom first. At other approach angles, the molecule has to undergo a reorientation. This can lead to changes in the H−C−H tetrahedral angle, which is associated with energy barriers. The exact height of the barrier depends on the original orientation of the methane molecule, but the barrier is generally higher for CD_4 than CH_4. This may explain the experimentally observed KIEs.

5.3 Origins of Reactivity

The question arises as to why $Ta_2O_5^+$ exhibits such peculiar reactivity. In general, it has been reported for other metal oxides that a high spin density on oxygen is a prerequisite for the occurrence of a HAT [75, 76]. Therefore, the spin density was determined for both investigated systems. As shown in Figure 34, only $Ta_2O_5^+$ exhibits oxygen atoms with high spin densities. Here, only the two oxygen atoms bound end-on to the same tantalum atom are reactive toward HAT. This explains why molecular adsorption takes place when methane approaches the cluster from the other direction and the two reaction types do not influence one another significantly. Moreover, it can be seen that the oxygen atom in syn-position has a slightly higher spin density compared to the one in anti-position. This goes in line with the higher energy gain for the respective HAT, as it was shown in Figure 33. Thus, while one of the driving forces of the dehydrogenation of methane on $Ta_2O_2^+$ is the formation of CH_2 bridges and the resulting energy gain, the high spin density of oxygen on $Ta_2O_5^+$ enables the HAT reaction.

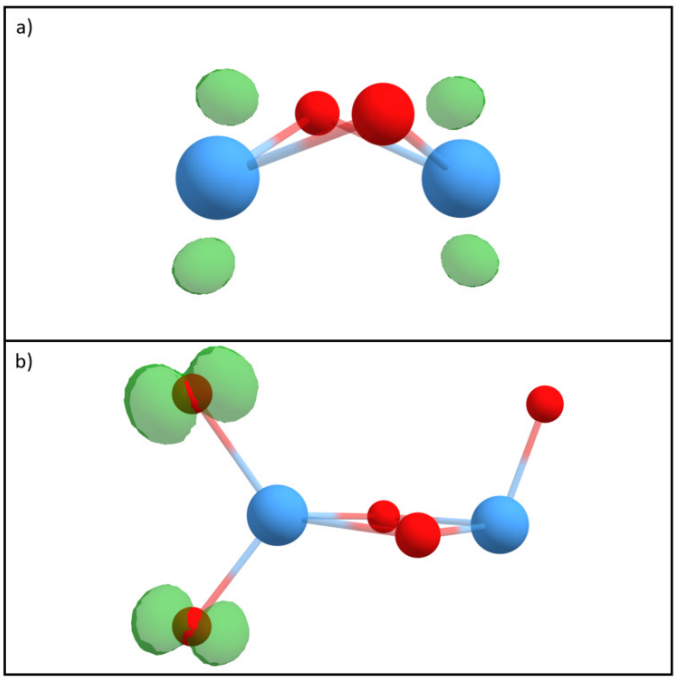

Figure 34: Comparison of the spin densities, given in green (isosurface 0.03 e/Bohr^3), on a) $Ta_2O_2^+$ and b) $Ta_2O_5^+$. For $Ta_2O_2^+$, the spin density is located on the tantalum atoms (shown in blue), while for $Ta_2O_5^+$, two of the oxygen atoms (shown in red) carry all the spin density. Taken from [15].

Furthermore, the spin density on $Ta_2O_5^+$ is investigated during the course of the reaction. As it is shown in Figure 35.a, the bare metal-oxide cluster exhibits two reaction sites, namely the Ta atom bound to one end-on oxygen atom as the site for molecular CH_4 adsorption, and the two oxygen atoms with high spin density enabling a HAT. This spin density is not influenced by the adsorbed CH_4 molecule (Figure 35.b), confirming the assumption of two independent reaction centers and explaining the similar KIEs for the two HATs listed in Table 4. Once the hydrogen atom has been transferred (Figure 35.c), the spin density on both oxygen atoms vanishes, preventing further HATs from taking place. The final product $Ta_2O_5HCH_4^+$, shown in Figure 35.d, has an occupied site for molecular CH_4 adsorption and exhibits no significant spin density on any oxygen atoms. It is therefore inactive with regard to reactions with further methane molecules.

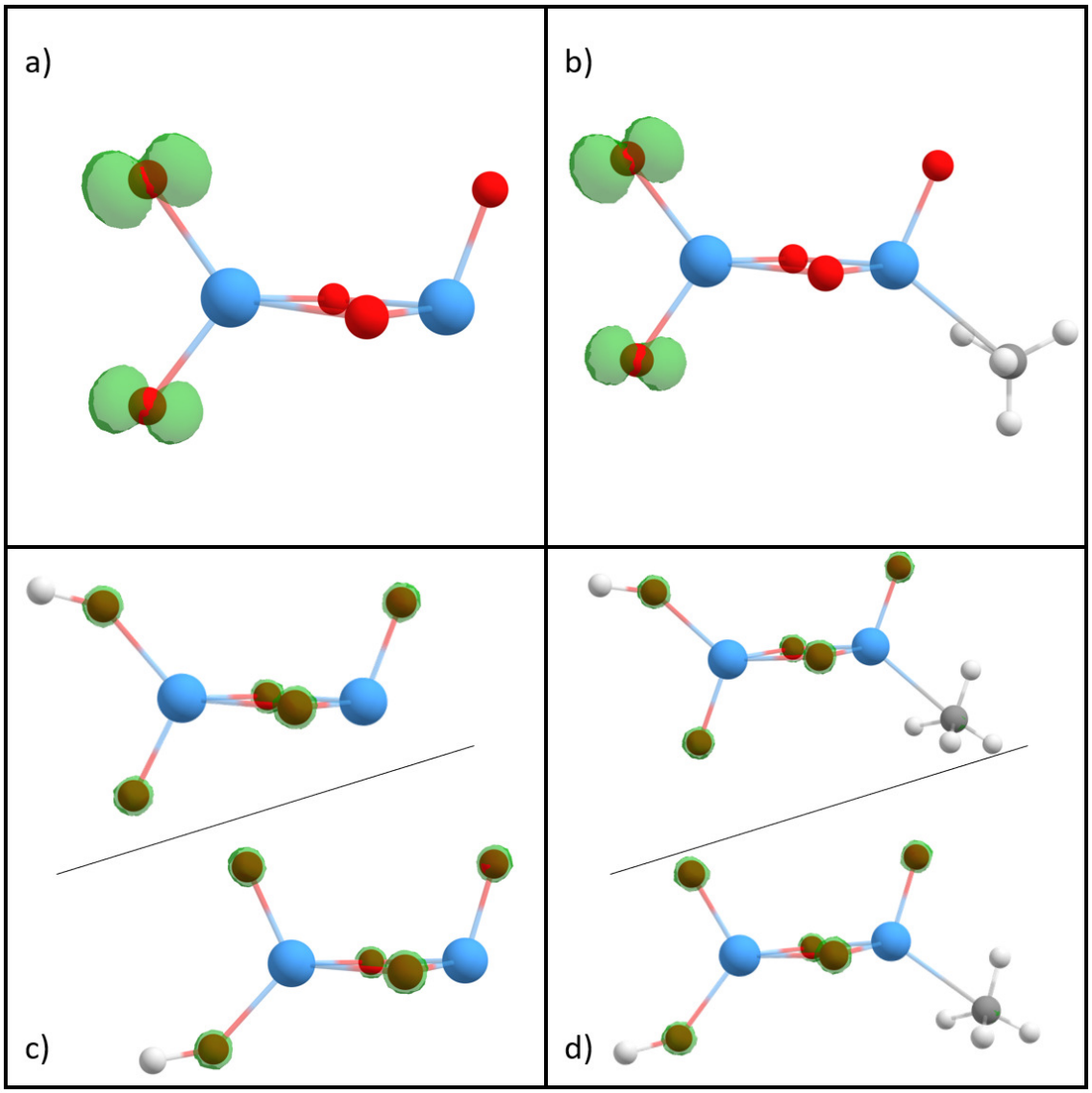

Figure 35: Changes in spin density (isosurface 0.03 e/Bohr^3; given in green) during the course of the reaction of $Ta_2O_5^+$ with two methane molecules. a) shows the bare metal-oxide cluster. On b) methane is adsorbed to the tantalum atom, which does not influence the spin density on the oxygen atoms. The spin density vanishes completely once the HAT has taken place (c) and does not further change when an additional methane molecule adsorbs to the cluster (d). Tantalum atoms are shown in blue, oxygen in red, carbon in gray and hydrogen in white. Taken from [15].

6 Studies of Platinum Clusters

6.1 Switching from Cations to Anions and Vice Versa

All data shown within this section has been recorded using the setup shown in Figure 5 with the addition of the *Faraday* Cup described within Section 3.1.5. The target is switched from tantalum to platinum and the cluster source is optimized for the production of anionic Pt clusters. The process is monitored using the picoammeter as described in Section 3. The optimized He pressure inside the cluster source equals $2.1 \cdot 10^{-1}$ mbar and an ideal pulse time of 680 ms after the flash lamp trigger is obtained. The laser is set to maximum power, which equals around 7.2 W before passing the converging lens. In order to bend the clusters in the bender, the applied voltage is switched from positive to negative voltages. While the QMF does not have to be adjusted to the polarity of the clusters per se, an applied pole bias of the respective other polarity increases the transmission by up to 15% in comparison to not applying any bias at all. Typical values range up to a maximum of $\pm$100 V, whereby the exact value is dependent on the cluster size. When the ion trap is used in guiding mode, only RF fields are applied, which do not have to be adjusted to the clusters' polarity. For the storage and subsequent precise release of the clusters, the polarity of the voltage has to match that of the clusters. In order to pulse the reaction products into the (re-)ToF-MS, the positive high voltage pulses for cationic clusters have to be changed to negative ones. Therefore, the trigger pulses are adjusted according to Figure 12 mentioned in Section 3.1.5. The cluster current of the anionic cluster beam is measured on the installed *Faraday* cup (see Figure 36.a).

The QMF is set to mass scanning mode to check for the present cluster sizes. The scan covers steps of 1 amu, ranging from 1.000 - 10.000 amu, and each mass is recorded for 100 ms. The obtained scan shows an onset in the cluster current at around 2.500 amu, which equals to Pt_{12}^-. The maximum intensity is in the range of 8.000 - 10.000 amu, which corresponds to Pt_{40}^- - Pt_{50}^-. The mass-selected cluster current for these clusters is approximately 250 pA. The mass resolution of the QMF is not sufficient to resolve individual cluster sizes in this mass regime. By applying a negative voltage to the *Faraday* cup and recording how the unselected cluster current decreases, the kinetic energy of the cluster beam is determined.

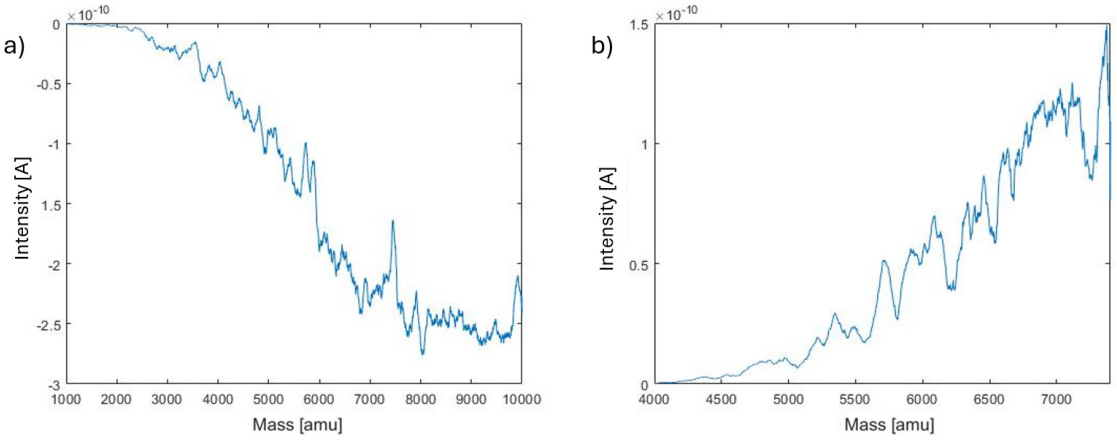

Figure 36: Cluster current measured using the picoammeter connected to the *Faraday* cup. The mass scan is performed using the QMF. a) shows the mass scan for anionic clusters, b) for cationic ones, produced under the same conditions ($2.1 \cdot 10^{-1}$ mbar He pulsed 680 ms after the flash lamp trigger, maximum laser power).

The experiment is summarized in Figure 37.a. When applying more than 70 V to the *Faraday* cup, no cluster current is measured anymore. At lower counter-voltages, the clusters arriving at the *Faraday* cup gradually decrease starting at a voltage of 20 V. This decrease corresponds with the cluster distribution (see Figure 37.b), leading to the assumption that the clusters have a kinetic energy of approximately 1 eV of per cluster atom.

a)

Applied Counter Voltage	Cluster Current
0 V	2.83 nA
10 V	2.81 nA
20 V	2.64 nA
30 V	2.28 nA
40 V	1.22 nA
50 V	0.391 nA
60 V	0.084 nA
70 V	0.008 nA

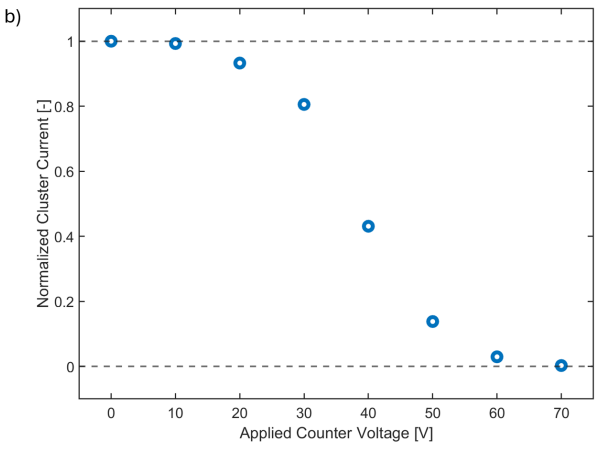

Figure 37: a) Measured cluster currents on the *Faraday* cup in dependence of the applied counter voltage (negative for anionic clusters). b) shows the respective visual representation. Values are normalized with the undeflected cluster current of 2.83 nA being 100%.

In order to analyze the clusters in the linear ToF-MS, the experiment is switched back to cationic clusters. All settings of the cluster source are kept the same. The polarity of the bender and the einzel lenses is switched, while the absolute value is kept constant. With these settings, a cationic cluster current of ≈1.2 nA is determined on the *Faraday* cup. The mass scan of the respective cationic cluster beam is shown in Figure 36.b. It can be seen that the positive clusters result in a positive ion current, while the anionic clusters resulted in a negative one. The cluster beam consists of clusters starting at 4.500 amu (≈Pt_{22}^{+}), with its maximum in the range of 7.000 - 8.000 amu (Pt_{35}^{+} - Pt_{40}^{+}), for which a mass-selected intensity of up to 150 pA is recorded. The intensity is lower than that of the optimized anionic clusters, but was later increased to the same values by fine-tuning the voltages of the einzel lenses. For the kinetic analysis, comparable results to the anionic clusters are recorded. A comparison of these characteristic values of cationic and anionic clusters can be found in Table 5.

Table 5: Comparison of anionic and cationic clusters produced under the same conditions. Mass selection is achieved using the QMF, the cluster current is measured on the *Faraday* cup.

	Anionic Clusters	Cationic Clusters
Onset	Pt_{12}^{-}	Pt_{22}^{+}
Maximum Intensity	Pt_{40-50}^{-} 250 pA	Pt_{35-40}^{+} 150 pA
Offset	16.000 (limited by QMF)	
E_{Kin}	≈1 eV/atom	

6.2 Pt_x^+ Clusters in the Linear ToF

The cationic clusters are analyzed in more detail within the linear ToF-MS above the *Faraday* cup. The QMF is set to RF-only mode, allowing a broad band of cluster sizes to pass through. Clusters arrive at the MCP after flight times of 10 - 15 μs, which is shown in Figure 38. Due to the amount of stable Pt isotopes and the large cluster sizes, resulting in broad Pt mass peaks, individual cluster sizes cannot be resolved.

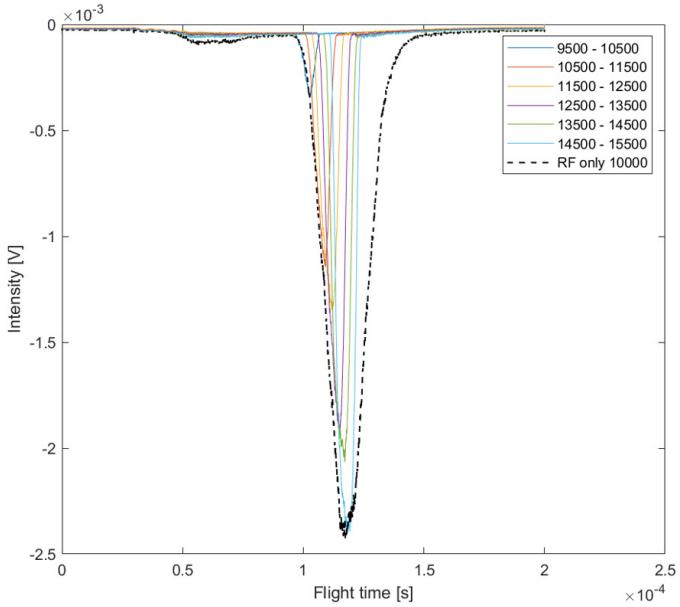

Figure 38: ToF mass spectra of cationic platinum clusters. The black dashed line represents the broad band spectrum with all cluster sizes present, while the colored lines show different mass regions, filtered with the QMF. Adding up all colored lines results in the broad band spectrum.

As a next step, the cluster beam is mass selected in the QMF prior to being analyzed in the ToF-MS. The respective regions involve 1.000 amu, which corresponds to about five sizes of Pt clusters. The individual mass-selected spectra follow the course of the broad band spectrum and thus show the individual components of the cluster current. The highest intensity results from clusters in the mass range of 14.500 - 15.500 amu, which correlates with Pt_{73}^{+} - Pt_{78}^{+}. This mass range corresponds to the upper mass limit of the QMF. With the mass information gained from the QMF, the flight times are converted into mass units. With the assumption of a constant kinetic energy for all clusters after their acceleration into the ToF-MS, the following quadratic equation for the calculation of mass units from flight times is obtained:

$$m = 2 \cdot 10^{13} t^2 - 3 \cdot 10^{t} + 124.634 \tag{10}$$

where m is the mass in amu and t the time in seconds.

The determined masses in the ToF spectrum correspond to clusters ranging from Pt_{45}^+ - Pt_{100}^+. The cluster distribution is shifted to smaller sizes by adjusting the pressure in the cluster source to $1.8 \cdot 10^{-1}$ mbar and delaying the opening of the piezo valve by 150 μs. With this approach, the smallest detectable species in the ToF-MS is Pt_{32}^+.

These clusters are then stored in the REIT. The optimized RF settings are a frequency of 140 kHz and an amplitude of 80 V (for the REIT being filled with He). The ideal DC voltages used for the storage and extraction of the clusters are dependent on the cluster size. Therefore, Pt_{40}^+ clusters are size selected in the QMF (m/z range: 7.770 - 7.850 amu) and guided into the REIT. To store the clusters in this mass range, a DC voltage of 13 V is applied to the entrance lens, while 25 V are applied to the exit lens. For the extraction, a voltage gradient starting at 20 V at the entrance lens, decreasing to 3 V on the exit lens, is chosen. Preliminary studies on the reactivity of NH_3 with cationic Pt clusters are performed in order to see if an interaction at room temperature takes place. To do this, Pt_{40}^+ clusters are stored for 500 ms with 2.5% NH_3 mixed into the buffer gas He. The storage time and the NH_3 concentration are chosen relatively high to allow a maximum number of ammonia molecules to adsorb to the clusters. A mass spectrum is recorded in the ToF-MS after the reaction (see Figure 39).

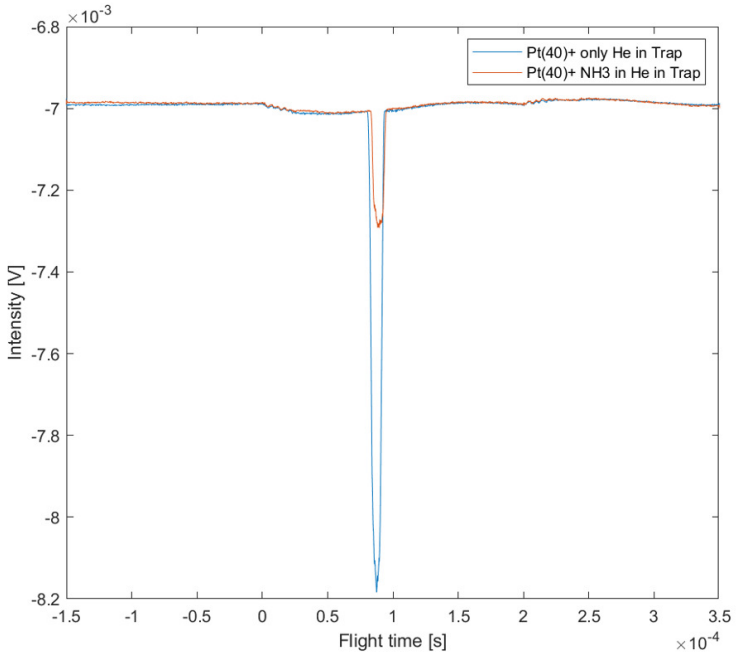

Figure 39: ToF mass spectra of Pt_{40}^+ clusters passing the REIT filled solely with He (blue) and stored for 500 ms inside the REIT filled with 2.5% NH_3 (orange).

Comparing the mass spectra of pure Pt_{40}^{+} clusters and the ones interacting with NH_3 in Figure 39, a shift of ≈0.8 ms in the flight time is recorded. This corresponds to a mass addition of approximately six ammonia molecules. Moreover, the peak is slightly broader. This can be explained by the addition of ammonia and its fragments, e.g., possibly NH after the release of H_2, as it was reported for the interaction of Pt^+ with NH_3 under single collision conditions by *Koszinowski* et al. [13]. While the resolution of the linear ToF-MS does neither allow the determination of an activation of the ammonia molecules nor a more detailed study of the reactivity, these preliminary results show that cationic platinum clusters are a promising candidate for ammonia slip catalysts, since an interaction at room temperature takes place. In order to investigate possible reaction mechanisms, it is advantageous to examine smaller clusters, since the peak broadening of the larger clusters due to the amount of platinum isotopes makes it harder to resolve the addition of single hydrogen atoms. Consequently, the composition of the cluster beam is investigated in more detail before it may be altered by passing apparatus parts like the QMF and the REIT. Hence, the linear ToF-MS located directly after the bender with its newly installed MCP detector described in Section 3.1.5 is used.

6.3 Initial Operation of the New MCP Detector

The new MCP detector is installed as described in Section 3.1.5. In order to condition the MCP plates to the high voltages, the potential has to be increased for the first time according to the following protocol:

1. Slowly increase the voltage in 100 V steps

2. Stay at the set voltage until it is stable (minimum 60 s)

3. At 1 kV, 2 kV and 2.6 kV, wait for 15 min

4. Once the final voltage (3 kV) has been reached, maintain it for 1 hr

During the whole process, the current applied by the power supply is monitored in order to check for spark formation. Moreover, the signal readout is monitored with an oscilloscope to check whether there is an increase in the baseline when high voltages are applied. If the baseline suddenly rises significantly, this indicates a short circuit between the MCP detector and the anode, possibly destroying the oscilloscope channel when further increasing the voltage. In this case, the power supply is switched off immediately and the wiring has to be checked again. Once the final voltage of 3 kV is reached, a current of 0.53 mA is observed. This is in agreement with the expected value, which is calculated as:

$$I = \frac{U}{R_{tot}} = \frac{3\ kV}{5\ M\Omega + 0.5\ M\Omega} = 0.55\ mA \tag{11}$$

whereby the resistances present can be seen in Figure 11.

After the MCP detector has been successfully conditioned to these high voltages, the signal from the residual gas particles that randomly strike the MCP is measured to determine the amplification factor of the detector. This so-called single-particle signal is shown in Figure 40. The width of the signal is approximately 50 ns, which is relatively broad. Both the single-particle signals and later the cluster signals with an amplitude above approximately 300 mV show an oscillating signal after the detected peak. This so-called ringing indicates an impedance mismatch within the detector, resulting in reflections oscillating back and forth at points with impedance changes [109] and is also observed in the recorded Ag_x^+ (Figure 42) and $Pt_x^{+/-}$ spectra (Figure 44, Figure 48). Although these oscillations partially overlap with the recorded peaks and thus alter the area under the peaks, the qualitative analysis of the peak positions performed within this work is not affected by the MCP ringing.

When a voltage difference of 3 kV is applied to the MCP detector, the impact of a single molecule results in a signal with an amplitude of 4 V. Since the used oscilloscope can handle a maximum input voltage of 10 V, lower amplifications are used in order to not put the input channel at risk when measuring stronger cluster currents. Experiments are repeated for amplification voltages of 2.7 kV and 2.4 kV. For smaller values, no single-particle signal could be determined. In order to better conserve the MCPs, further experiments are performed with an applied voltage of 2.4 kV.

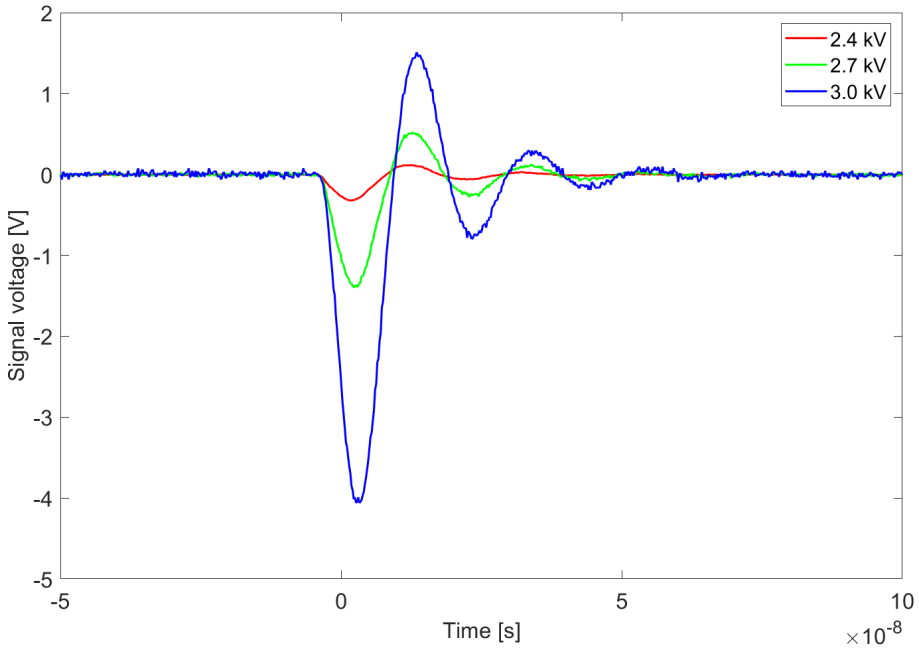

Figure 40: Comparison of the single-particle signals recorded at different amplification voltages in the MCP detector. The specified voltages denote the voltage applied between MCP_{in} and MCP_{out}.

6.4 Calibration of the Linear ToF-MS

Before performing the desired experiments, information about the flight times within the ToF-MS has to be gained. Since the cluster beam is not passing the QMF before entering the mass spectrometer, no information about the size distribution of clusters within the cluster beam is available. Due to the resolution of the ToF-MS, the broadband spectrum cannot easily be used for calibration as usual. Instead, silver spectra are measured because of the element's characteristic isotope pattern. Both stable

isotopes of Ag are distributed almost evenly (107 amu: 52%, 109 amu: 48%), which allows an unambiguous assignment of the present cluster sizes. As Ag has almost half of the mass of Pt and the mass difference between the two isotopes is 2 amu, it is possible to resolve the individual isotopes even with larger cluster sizes. The measured flight times of the three most intense signals (Ag_1^+ - Ag_3^+) are assigned to the respective masses according to Figure 41.a.

a)

Flight Time [µs]	Mass [amu]
13.28	107
13.40	109
18.71	214
18.80	216
18.88	218
22.89	321
22.95	323
23.02	325
23.09	327

b)

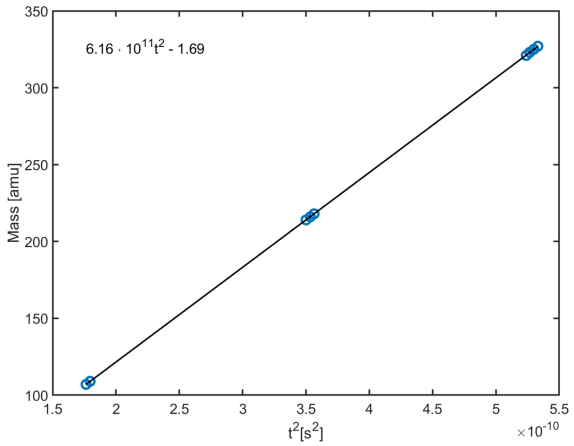

Figure 41: a) Time of flight values for the respective Ag peaks used for determining the relation between mass and time of flight. b) shows the respective visual representation, whereby mass values are plotted against the square of the corresponding flight times. The linear regression reflects the formula used for conversion.

With this information and the assumption that all clusters are singly positively charged, the following correlation between mass and flight time can be established:

$$m = 6 \cdot 10^{11} t^2 - 1.6908 \tag{12}$$

This equation is used for the axis transformation of all following spectra recorded using this linear ToF-MS with applied acceleration voltages of 4.631 kV on the repeller plate and 3.827 kV on the first plate of the extractor stage (compare Figure 7). The resulting mass spectrum of the peaks used for calibration is shown in Figure 42. The spectrum clearly shows Ag_1^+ - Ag_3^+ clusters with the respective isotopic pattern (Ag_1^+: 107 and 109 amu, Ag_2^+: 214, 216, and 218 amu, Ag_3^+: 321, 323, 325, and 327 amu).

For Ag_4^+, the signal intensity decreases drastically, only showing a small broad peak at 432 amu. The signal of Ag_5^+ is again higher, allowing a differentiation between the four most abundant isotopes of the expected six at 535, 537, 539, and 541 amu. This indicates that the mass resolution of the linear ToF-MS $\frac{m}{\Delta m}$ is approximately 300. While the isotope pattern correlates well with the expected mass spectra for these smaller cluster sizes, heavier clusters are not observed in the spectrum. Due to the high intensities, peaks with amplitudes above ≈300 mV again exhibit ringing, as discussed within Section 6.3. The intensity of the oscillating signal is thereby proportional to the one of the cluster signal.

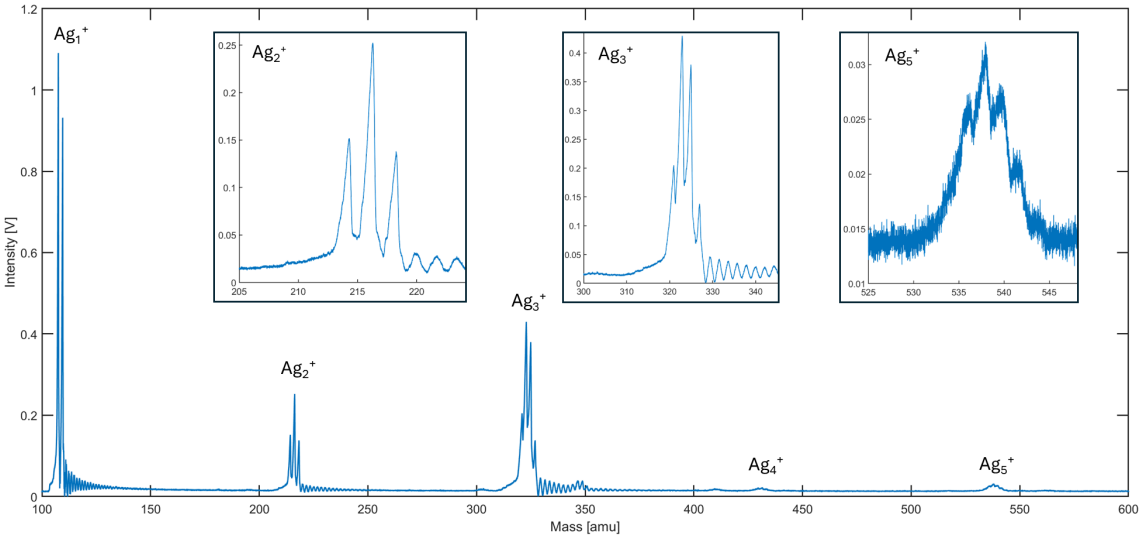

Figure 42: Mass spectrum showing the peaks of Ag_1^+ - Ag_5^+ with its isotopes.

In order to further confirm a correct peak assignment and to test the functionality of the general valve, $2.5 \cdot 10^{-5}$ mbar oxygen (measured in the bender) is pulsed into the second waiting room of the cluster source. While Ag_1^+ and Ag_2^+ are uninfluenced by the oxidation (compare Figure 43), Ag_3^+ is partially oxidized to Ag_3O^+, which results in an additional peak located at a Δm of +16 amu in respect to the unoxidized species. The oxidation product shows the same isotope pattern as Ag_3^+.

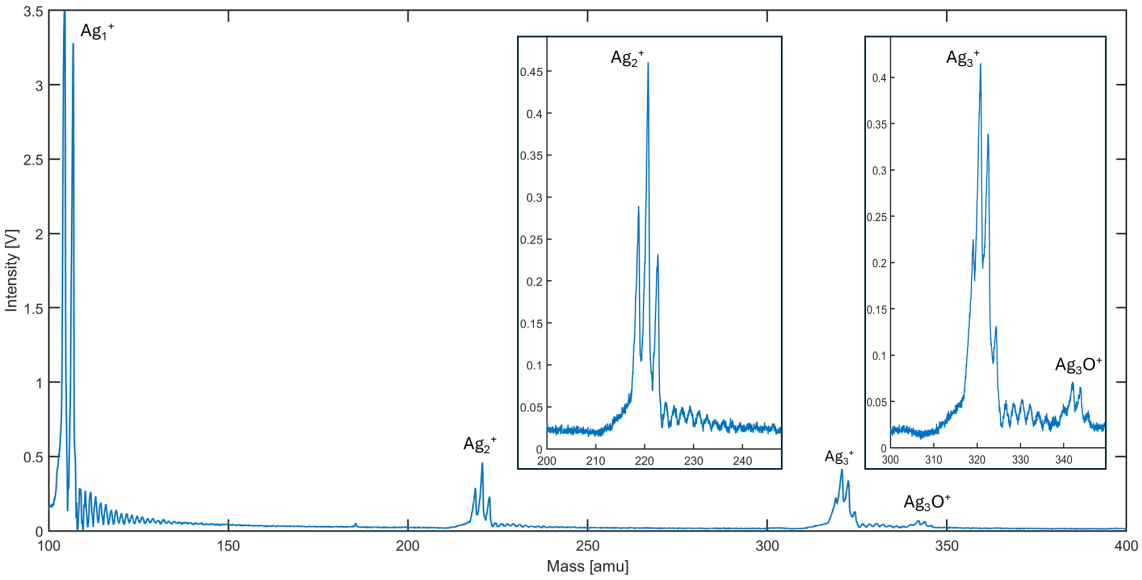

Figure 43: Mass spectrum showing Ag_1^+ - Ag_3^+ after the oxidation in the cluster source at an oxygen pressure of 2.5 · 10^{-5} mbar (measured in the bender). While the cation and the dimer ion are not oxidized, a small fraction of Ag_3O^+ is formed.

6.5 Platinum Cations and Their Interaction with NH_3

The target is switched to platinum while the acceleration voltage is kept the same. The timing of the ion withdrawal into the ToF-MS is set to 30 μs after the laser shot. The cluster production parameters are as discussed previously in Section 6.1. With these settings, mainly the platinum cation and a small fraction of Pt_2^+ - Pt_3^+ reaches the MCP detector. By applying a voltage of $\pm$200 V to the deflector plates, larger cluster sizes can also be measured, which indicates that they have a higher velocity in x-direction. This needs to be corrected by the deflector plates in order to arrive at the MCP detector. The respective mass spectrum is shown in Figure 44.

While after the QMF, only large platinum clusters (> Pt_{32}^+) were obtained, the newly commissioned ToF-MS shows a distribution in which Pt_1^+ is the main component and the abundance slowly decreases up to Pt_{25}^+ as the largest cluster size. While for Pt_1^+, the isotopic pattern is clearly visible, isotope peaks already start to merge for Pt_2^+. For Pt_3^+ and higher cluster sizes, no isotopic pattern can be determined anymore. This indicates that the linear ToF-MS has a mass resolution $\frac{m}{\Delta m}$ of approximately 300. This value matches the resolution determined via the silver clusters. One possible explanation for these low resolutions might be the high cluster current. Currents of up to 25 nA (measured for Pt_x^+ clusters) are present in front of the extraction stage. Within

this concentrated cluster beam, the initial velocity distribution can be high, which can potentially lead to peak broadening and thus a decrease in resolution. Therefore, the resolution could be significantly improved by including a reflectron stage and installing a pinhole shortly before the extraction region, which allows only a small fraction of clusters focused in space to pass [67, 68]. Comparing the intensity with the mass spectrum shown in Figure 38, the signal intensity of Pt_1^+ is about ≈20 times greater than the maximum signal recorded in the old ToF. On the one hand, this is due to the better amplification of the new MCP detector. On the other hand, the cluster current did not pass any central components, which are the main source of loss of ions. Starting at Pt_5^+, additional peaks appear in the spectrum. They are always located in the center between two peaks, indicating the presence of multiply charged species. Since these doubly charged clusters account for only around 0.2% of the total cluster beam, the approximation of only taking singly charged species into account is confirmed when considering that typical experimental errors are usually much larger.

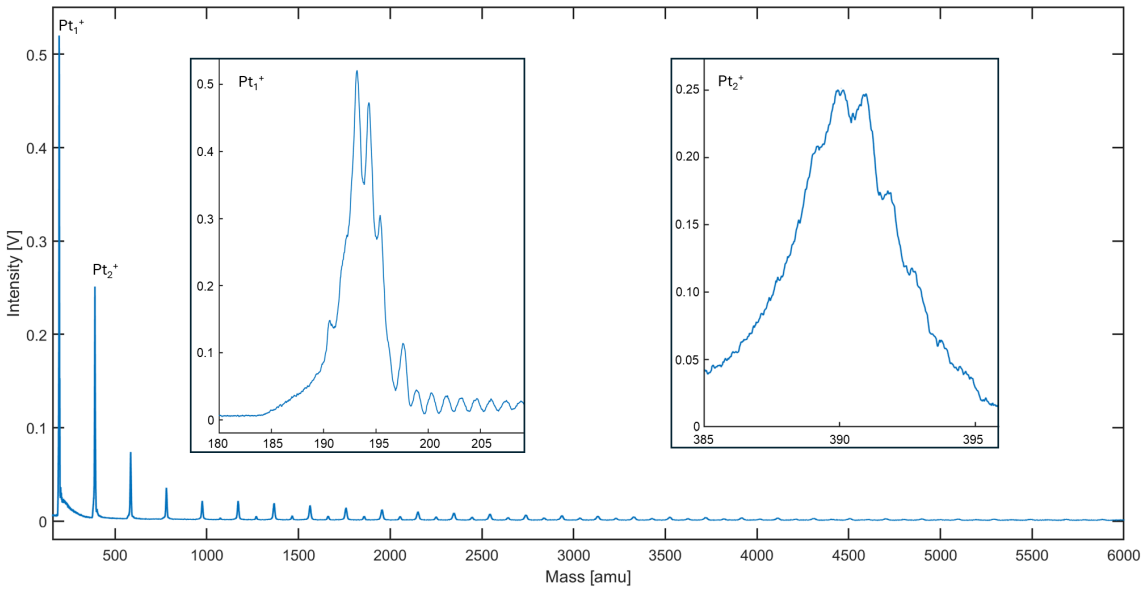

Figure 44: ToF mass spectrum of Pt_1^+ - Pt_{25}^+ clusters recorded with ±200 V applied to the deflector plates. Isotopic resolution is achieved for Pt_1^+ and Pt_2^+. Starting between Pt_5^+ and Pt_6^+, additional peaks appear in the middle between two peaks, indicating the presence of multiply charged species.

The focus of the mass spectrum can be shifted by varying the timing of the extraction, whereby higher extraction times correlate to larger clusters. As shown in Figure 45, maximum cluster sizes of $\approx Pt_{40}^{+}$ are recorded at delays of 9.98 ms. With a 100 Hz laser, these clusters arrive at the extraction stage shortly before the new laser pulse is emitted and the next cluster beam is produced. The atomic Pt cation and smaller clusters pass the chamber quickly, already arriving 10 μs after formation and vanish from the spectrum at a delay of approximately 140 μs. The absolute intensity of the clusters with masses of up to 2.500 amu is significantly smaller than for the larger clusters. This might explain why neither the atoms nor small clusters were observed after the bender and the QMF, since this small fraction of the cluster beam might have been lost on the way. For larger clusters, the intensity decreases again, while no clusters above masses of 8.000 amu could be observed. Moreover, this experiment shows that the clusters are distributed over a relatively long cluster beam, with their position depending on their masses. Since the bender is used in a pulsed manner, only a certain size regime is bent and can therefore enter the QMF. This further explains the mass distribution discussed in Section 6.2, where no optimization for clusters smaller than Pt_{32}^{+} could be achieved. In order to use all cluster sizes in future experiments, the cluster source has to be further optimized to get a more time-focused cluster beam.

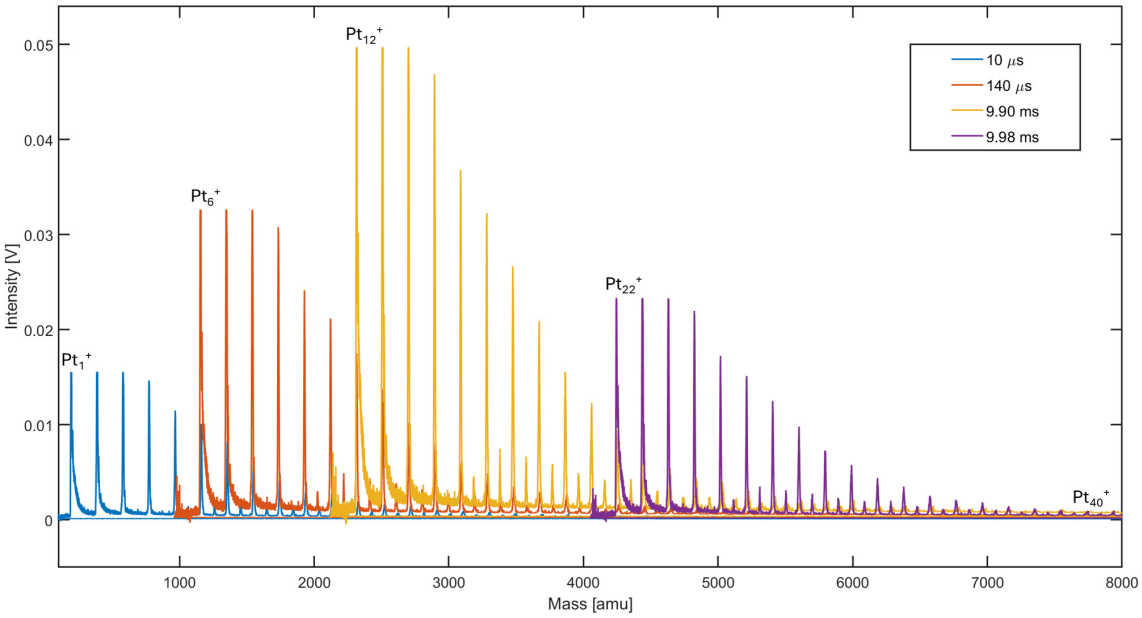

Figure 45: Mass spectra of Pt cluster cations at different extraction delays into the ToF-MS. The extraction delays are referenced to the laser shot. Small delays correlate with the detection of the Pt cation and small clusters, longer delays of up to 9.98 ms with large clusters of masses up to 8.000 amu.

When starting the experiment after not using the laser vaporization cluster source for more than 8 h, additional peaks after Pt_1^+ - Pt_3^+ become visible for a short time (see Figure 46). With a mass of +12 amu in comparison to the bare metal peak, this is ascribed to the formation of platinum carbides. This indicates the adsorption of carbonaceous species on the metal target over time. Since it is unlikely that higher cluster sizes are not influenced by these contaminants, the absence of a carbide peak is attributed to signal intensities below the detection limit. The intensity of the present carbide peaks decreases as the cluster source's runtime increases. After approximately 4 min, the peak vanishes and only pure metal clusters are produced. Interrupting the experiment for shorter times (up to 4 h) does not lead to a measurable adsorption of contaminants.

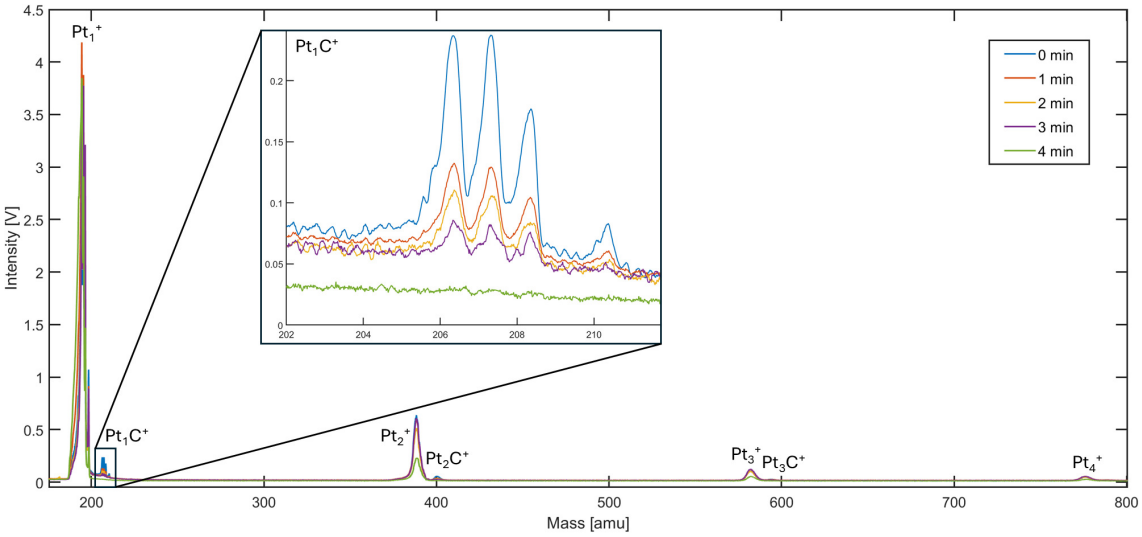

Figure 46: Mass spectrum recorded directly after turning on the cluster source for the first time of the day (blue). Pt_1^+ - Pt_3^+ show carbon contamination. A new spectrum is recorded every minute. After 4 min of cluster generation, no carbide peak is visible anymore.

After the cluster source is operated long enough so it produces solely pure metal clusters, $2.5 \cdot 10^{-5}$ mbar NH_3 (measured in the bender) are added to its second waiting room. The optimal timing for the extraction of the platinum atom into the ToF-MS is shifted from 10 μs to 25 μs, which indicates an interaction of the clusters with the added gas. This is confirmed by the recorded mass spectrum (Figure 47), which shows an additional peak with a mass of +17 amu for Pt_1^+ and Pt_2^+. This is attributed

to the addition of NH_3. It cannot be distinguished between molecular adsorption and an interaction leading to the activation of the ammonia molecule. *Koszinowski* et al., however, reported a possible activation of NH_3 on the platinum cation via the release of H_2 under single-collision conditions [13]. The absence of the corresponding NH-peak in Figure 47 could be due to multi-collision conditions in the cluster source, which lead to a different reaction behavior. Alternatively, the individual species may not be resolvable with the used linear ToF-MS. Further reaction studies of this system have to be carried out using the REIT to elucidate the underlying reaction mechanism. Reaction products are then analyzed using the re-ToF-MS to ensure proper mass-resolution. The signal of $PtNH_3^+$ shows the same width and general shape as the bare platinum cation, confirming the peak assignment. For higher cluster sizes, no product of the interaction with ammonia is observable, which might, however, be due to the inferior signal of the bare metal cluster.

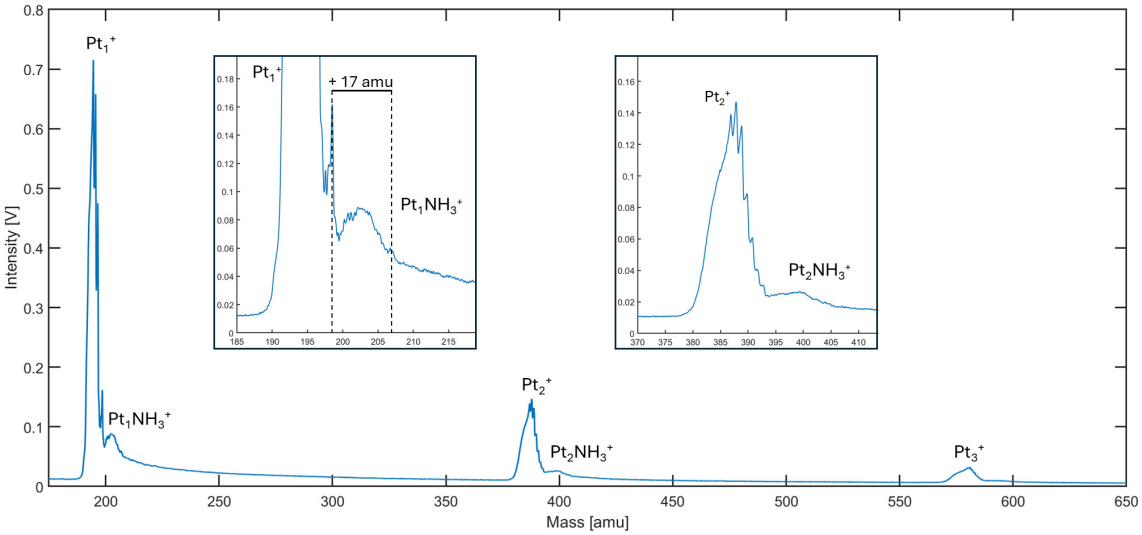

Figure 47: ToF mass spectrum recorded for the interaction of Pt_1^+ - Pt_3^+ with ammonia. While an addition of one NH_3 molecule takes place on the platinum cation and Pt_2^+, no interaction is observable for Pt_3^+ and higher cluster sizes.

As an outlook, the cluster source is switched back to anionic clusters. With all parameters kept the same except for the polarity of necessary voltages being altered, only Pt_1^- - Pt_4^- can be observed in the ToF-MS (Figure 48). While the intensity of the atomic anion is approximately three times higher than the one for the cation shown in Figure 44, the resolution is worse. However, the general shape of the isotopic pattern

of Pt_1^- can be resolved. For Pt_2^-, no splitting into the respective isotope peaks can be seen. The peaks are slightly distorted, indicating that the clusters are not fully focused onto the MCP detector. In order to adjust the space focus, the ratio between the extraction voltages has to be adjusted.

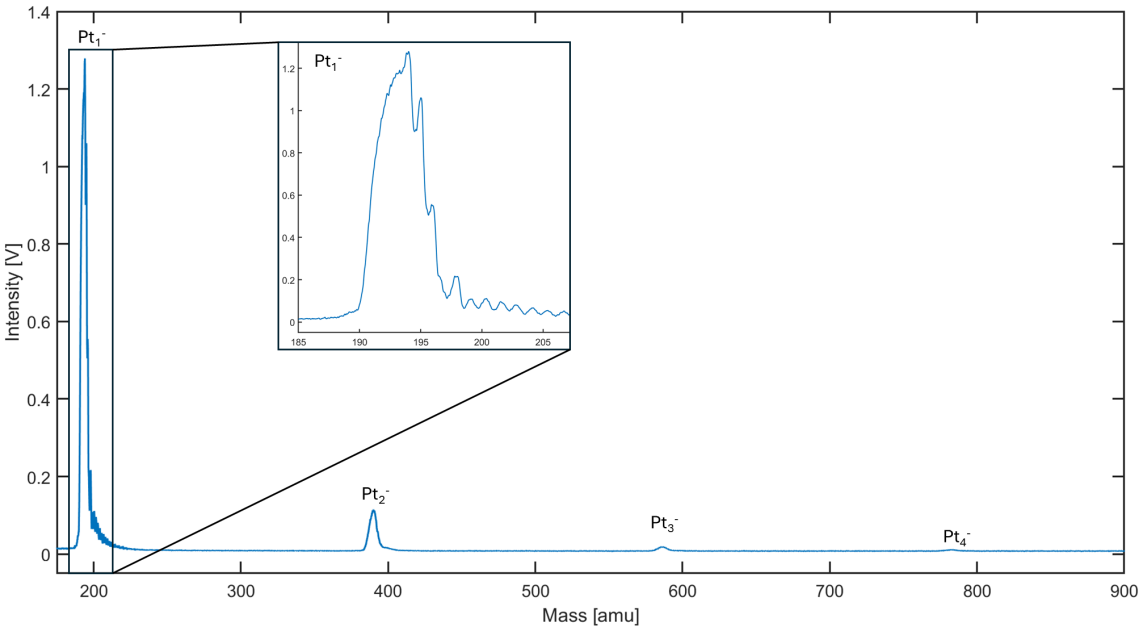

Figure 48: ToF mass spectrum of the anionic platinum species. Using the parameters from previous experiments with cationic clusters, only Pt_1^- - Pt_4^- clusters are produced, and the measured resolution is worse than that in the respective cationic spectra.

7 Conclusion and Outlook

In this thesis, the reactivity of tantalum- and platinum(oxide) clusters toward methane, ammonia and N_2 is discussed. In a first step, it is shown how gas phase experiments can be used to benchmark a system. Reviewing literature on the reactivity of tantalum(-oxide) clusters in the interaction with these small molecules provided a fundamental understanding of underlying reaction mechanisms (see Section 4, [14] and references therein). It is shown that the reactivity of clusters is strongly dependent on their size and oxidation state. These molecules can either adsorb to the clusters molecularly or be activated. The activation of methane is achieved by small tantalum clusters via a metal insertion mechanism, which can lead to the release of hydrogen, leaving behind a CH_2-moiety. The amount of methane molecules that can be activated by a single cluster is dependent on the cluster size. It is believed that the electrons localized in the Ta$-$Ta σ-bond are responsible for the C$-$H bond activation. On the tantalum atom, C$-$C coupling is enabled, which is different to the reaction of other Ta clusters with the exception of $Ta_2O_8^+$. Analogously to the insertion of tantalum into the C$-$H bond, the N$-$H bond in ammonia is also activated by the same mechanism. This leads to the formation of an imine and the release of hydrogen. It is reported that the amount of activatable NH_3 molecules depends on the number of empty d- and p-orbitals in the cluster and thus on the cluster size, charge, and oxidation state. Once these orbitals are filled, no direct interaction between the electrons of the lone pair of NH_3 and the cluster is possible and further molecules can only adsorb to the compound. Cluster size also critically influences the activation of N_2. Only small tantalum clusters (up to four atoms) are capable of activating the strong N$\equiv$N triple bond, forming highly stable dinitrides. During this process, N_2 first coordinates end-on to one tantalum atom, after which it is bent toward a neighboring one. For larger clusters, energy barriers for the tilting become too high and nitrogen only adsorbs molecularly. A reason for this might be the possibility of double and triple coordination of N_2 at a single tantalum atom in these larger species, allowing for the adsorption of more nitrogen molecules in closer proximity. This might result in a N_2-N_2 cooperativity, leading to a significant energy advantage that would have to be overcome in clusters with more than five tantalum atoms.

Based on this literature review, this thesis shows that the oxidation of tantalum compounds also has a strong influence on their ability to activate methane. On $Ta_2O_x^+$ ($0 \leq x \leq 6$), the reaction mechanism changes from methane dehydrogenation reactions for low degrees of oxidation to molecular adsorption for highly oxidized species (see Section 5 and [15]). An exception is $Ta_2O_5^+$, where a HAT occurs. There, the hydrogen atom of methane interacts directly with the oxygen atom of the cluster, releasing a CH_3-radical. The experimentally observed reactivity is supported by DFT calculations, which show that the reason for this reaction behavior, unusual for Ta compounds, is the high spin density on oxygen, which is a typical reactivity feature in metal oxides. DFT calculations also identify the formation of CH_2 bridges as a possible driving force for the methane activation on $Ta_2O_2^+$, whereby the cleavage of the first $C-H$ bond is the rate-determining step. The mechanism of the subsequent activation of a second methane molecule was found to take place analogously, after which methane dehydrogenation stops.

Furthermore, preliminary studies on the interaction of platinum clusters with NH_3 were conducted, which are presented in Section 6. The newly installed *Faraday* cup allows for an optimization of the clusters' flight paths through the acceleration stage of the ToF-MS. It has been shown that trigger pulses for HV-pulse generation and the voltages of the einzel lenses can be adjusted in such a way that it becomes possible to switch between anionic and cationic cluster species. It was found that clusters of both charge states with a kinetic energy of approximately 1 eV per atom are formed in the cluster source, which could be detected using mass spectrometry. A newly installed linear ToF-MS with a z-stack MCP detector in a configuration that allows for detection of both charge states was calibrated using Ag_x^+ clusters. Measurements of platinum clusters reveal contamination by carbonaceous species, which can be removed by laser illumination for several minutes. Cationic platinum species were found to interact with ammonia. This is demonstrated for the reaction of the atomic cation and small clusters directly in the cluster source, while for larger clusters, this reaction occurred in the REIT. These experiments performed under multi-collision conditions revealed first differences from the results found in literature for single-collision conditions [13]. While H_2 is eliminated on the platinum cation, as reported by *Koszinowski* et al., adsorbed NH_3 appears to be stabilized under the conditions applied in this work.

These preliminary results show promising interactions of platinum (cluster) cations and ammonia. Precise kinetic information may be obtained from further ion trap reactivity studies. Reactivity experiments of both charge states can be performed and compared. Gained information can be linked with geometry information from existing TIED studies of anionic platinum clusters [39]. These studies show the transition between different geometric motifs with increasing cluster size, i.e., from a planar structure reported for Pt_6^- - Pt_7^- over an amorphous-like structure for Pt_7^- - Pt_9^-, to tetrahedral structures for Pt_9^- - Pt_{11}^-. Finally, structures based on hcp fragments emerge (found for Pt_{12}^- and Pt_{13}^-). Focusing on the reactivity of species at these junctures of geometric transitions (planar $\rightarrow$ amorphous $\rightarrow$ tetrahedral $\rightarrow$ hcp) could contribute to elucidating structure-reactivity relationships that might be applicable to more realistic systems [8]. Another key objective is to investigate both bare metal and oxidized cluster species, as the oxidation state reportedly influences the adsorption energies and reaction pathways [15]. For Pt-based surfaces, especially under oxygen-rich conditions, altered activities with regard to the ammonia oxidation reaction were reported [9]. The origins of these reactivities may be elucidated using gas phase model systems. For applied catalysts, the goal is to perform ammonia slip catalysis under realistic conditions without producing NO_x as a side product to N_2. Targeting cluster sizes at the transitions of geometric motifs and comparing both metallic and oxidic forms, supplemented by theoretical calculations of the systems, could here be used to benchmark structures of intermediates and reaction products, and kinetic data of active clusters in the gas phase. Hereby, a methodology similar to that used for the interaction of tantalum clusters with methane could be applied [14]. This way, knowledge about determined key properties influencing reactivity and selectivity may be transferable to more applied systems.

Li-doped MgO is an example of an applied bulk catalyst used for methane activation [110]. According to the mechanism proposed by *Wang* and *Lundsford*, the high spin density in form of a radical state on $Mg-O^{*-}$ enables a HAT, leading to the deactivated Mg−OH [74]. The main disadvantage of this system is the elevated reaction temperatures around 1.000 K, which are connected to higher costs and a faster degradation of the catalyst [110–112]. Since $Ta_2O_5^+$ showed a similar reaction behavior with a comparable potential driving force in our gas phase studies at room temperature, tantalum bulk compounds might be a promising candidate for performing methane conversion reactions at lower temperatures. A possible candidate for enabling this reaction could

be the stable bulk tantalum pentoxide [113]. To activate this compound, oxygen radical centers would have to be created in order to adjust the electronic structure so that it resembles that of $Ta_2O_5^+$. In MgO, this might be achieved by Li-doping, although this is controversial [110]. Moreover, the deactivation of the catalyst by forming unreactive $Ta-OH$ has to be prevented. In the case of the used Li-doped MgO catalyst, this is achieved by $Mg-OH$ reacting with present oxygen to arrive back at its reactive state [110]. For this reaction step, elevated temperatures are needed. Therefore, the proposed tantalum system may only be catalytically active if an efficient H_2 evolution is achieved additionally to a successful methane activation, which could for example be realized by introducing a suitable co-catalyst.

In summary, this thesis addresses how cluster size, oxidation state, and electronic structure influence the activation pathways of methane, ammonia, and N_2 on tantalum and platinum clusters, including their oxides. By using the presented gas phase model system to study these ion-molecule reactions, a step has been taken to a fundamental understanding of the reactivity, selectivity, and kinetics of the reaction systems. This may contribute to the future development of tailor-made catalysts with minimized environmental impact, which could for example be used in methane reforming or ammonia slip catalysis.

References

(1) Schwarz, H. *Angew. Chem., Int. Ed.* **2011**, *50*, 10096–10115.

(2) Tang, P.; Zhu, Q.; Wu, Z.; Ma, D. *Energy Environ. Sci.* **2014**, *7*, 2580–2591.

(3) Choudhary, T. V.; Choudhary, V. R. *Angew. Chem., Int. Ed.* **2008**, *47*, 1828–1847.

(4) Franchi, G.; Capocelli, M.; de Falco, M.; Piemonte, V.; Barba, D. *Membranes* **2020**, *10*, 10/1–20.

(5) Eckhard, J. F.; Masubuchi, T.; Tschurl, M.; Barnett, R. N.; Landman, U.; Heiz, U. *J. Phys. Chem. C* **2018**, *122*, 25628–25637.

(6) Eckhard, J. F.; Masubuchi, T.; Tschurl, M.; Barnett, R. N.; Landman, U.; Heiz, U. *J. Phys. Chem. A* **2021**, *125*, 5289–5302.

(7) Levin, N.; Lengyel, J.; Eckhard, J. F.; Tschurl, M.; Heiz, U. *J. Am. Chem. Soc.* **2020**, *142*, 5862–5869.

(8) Marchuk, V.; Huang, X.; Grunwaldt, J.-D.; Doronkin, D. E. *Catal. Sci. Technol.* **2023**, *13*, 2946–2965.

(9) Marchuk, V.; Sharapa, D. I.; Grunwaldt, J.-D.; Doronkin, D. E. *ACS Catal.* **2024**, *14*, 1107–1120.

(10) Grünert, W.; Kleist, W.; Muhler, M., *Catalysis at Surfaces*; Walter de Gruyter GmbH & Co KG: 2023.

(11) Daramola, D. A.; Botte, G. G. *Comp. Theor. Chem.* **2012**, *989*, 7–17.

(12) Daramola, D. A.; Botte, G. G. *J. Colloid Interface Sci.* **2013**, *402*, 204–214.

(13) Koszinowski, K.; Schröder, D.; Schwarz, H. *J. Phys. Chem. A* **2003**, *107*, 4999–5006.

(14) Siegele, F.; Tschurl, M.; Schooss, D.; Heiz, U. *ChemPhysChem* **2024**, e202400513.

(15) Siegele, F.; Eckhard, J. F.; Masubuchi, T.; Goddard, G.; Schooss, D.; Sharapa, D. I.; Studt, F.; Tschurl, M.; Heiz, U. *Chem. Eur. J.* **2025**, *31*, e202500545.

(16) Fadhel, A. Z.; Pollet, P.; Liotta, C. L.; Eckert, C. A. *Molecules* **2010**, *15*, 8400–8424.

(17) *Catalysis: An Integrated Approach to Homogeneous, Heterogeneous and Industrial Catalysis*; Moulijn, J. A., Ed.; Studies in surface science and catalysis, Vol. 79; Elsevier: Amsterdam, 1993.

(18) Zaera, F. *Coord. Chem. Rev.* **2021**, *448*, 214179–214194.

(19) Zaera, F. *Chem. Rev.* **2022**, *122*, 8594–8757.

(20) Delrieux, T.; Sharma, S.; Maurer, F.; Dolcet, P.; Lausch, M.; Zimina, A.; Cárdenas, C.; Lott, P.; Casapu, M.; Sheppard, T. L.; Grunwaldt, J.-D. *React. Chem. Eng.* **2024**, *9*, 2868–2881.

(21) Wang, B.; Yu, Z.; Chen, S.; Da Roit, N.; Schild, D.; Zimmermann, M.; Wang, Y.; Behrens, S. *Angew. Chem.* **2025**, *137*, e202423273.

(22) Schlangen, M.; Schwarz, H. *Catal. Lett.* **2012**, *142*, 1265–1278.

(23) Bakker, J. M.; Mafuné, F. *Phys. Chem. Chem. Phys.* **2022**, *24*, 7595–7610.

(24) Tawaraya, Y.; Kudoh, S.; Miyajima, K.; Mafuné, F. *J. Phys. Chem. A* **2015**, *119*, 8461–8468.

(25) Toker, Y.; Aviv, O.; Eritt, M.; Rappaport, M. L.; Heber, O.; Schwalm, D.; Zajfman, D. *Phys. Rev. A* **2007**, *76*, 053201/1–6.

(26) Lange, M.; Froese, M. W.; Menk, S.; Bing, D.; Fellenberger, F.; Grieser, M.; Laux, F.; Orlov, D. A.; Repnow, R.; Sieber, T.; Toker, Y.; von Hahn, R.; Wolf, A.; Blaum, K. *New J. Phys.* **2012**, *14*, 065007/1–16.

(27) Nagata, T.; Miyajima, K.; Mafuné, F. *J. Phys. Chem. A* **2015**, *119*, 10255–10263.

(28) Tolmachev, A. V.; Vilkov, A. N.; Bogdanov, B.; Pasa-Tolić, L.; Masselon, C. D.; Smith, R. D. *J. Am. Soc. Mass Spectrom.* **2004**, *15*, 1616–1628.

(29) Thomson, J. J. *J. Röntgen Soc.* **1914**, *10*, 41–42.

(30) Dempster, A. J. *Lond. Eding. Dubl. Philos. Mag.* **1916**, 438–443.

(31) Brodbelt, J. S. *Mass Spectrom. Rev.* **1997**, *16*, 91–110.

(32) Munson, B. *Anal. Chem.* **1971**, *43*, 28A–43A.

(33) Carrascosa, E.; Meyer, J.; Wester, R. *Chem. Soc. Rev.* **2017**, *46*, 7498–7516.

(34) Ng, C.-Y. *J. Phys. Chem. A* **2002**, *106*, 5953–5966.

(35) Meyer, J.; Wester, R. *Annu. Rev. Phys. Chem.* **2017**, *68*, 333–353.

(36) Neuwirth, D. The Design of a Ring Electrode Ion Trap with Enhanced Mass Range: Size-Dependent Oxidation of Tantalum Clusters, Ph.D. Thesis, Technische Universität München, 2015.

(37) Douglas, D. J.; Frank, A. J.; Mao, D. *Mass Spectrom. Rev.* **2005**, *24*, 1–29.

(38) Parks, J. H.; Xing, X. In *The Chemical Physics of Solid Surfaces : Atomic Clusters: From Gas Phase to Deposited*, Woodruff, D. P., Ed.; Elsevier: 2007; Vol. 12, pp 377–407.

(39) Bumüller, D.; Yohannes, A. G.; Kohaut, S.; Kondov, I.; Kappes, M. M.; Fink, K.; Schooss, D. *J. Phys. Chem. A* **2022**, *126*, 3502–3510.

(40) Gojare, S.; Bumüller, D.; Kohaut, S.; Kraft, M.; Heiz, U.; Kappes, M. M.; Fink, K.; Schooss, D. *ChemPhysChem* **2024**, *25*, e202400649.

(41) Oepts, D.; van der Meer, A.; van Amersfoort, P. W. *Infrared Phys. Technol.* **1995**, *36*, 297–308.

(42) Niedner-Schatteburg, G.; Kappes, M. M. *Chem. Eur. J.* **2021**, *27*, 15027–15042.

(43) Fielicke, A.; von Helden, G.; Meijer, G. *Eur. Phys. J. D* **2005**, *34*, 83–88.

(44) Fielicke, A.; Kirilyuk, A.; Ratsch, C.; Behler, J.; Scheffler, M.; von Helden, G.; Meijer, G. *Phys. Rev. Lett.* **2004**, *93*, 023401/1–4.

(45) Fielicke, A.; Gruene, P.; Haertelt, M.; Harding, D. J.; Meijer, G. *J. Phys. Chem. A* **2010**, *114*, 9755–9761.

(46) Engel, E.; Dreizler, R. M., *Density Functional Theory*; Springer Berlin Heidelberg: Berlin, Heidelberg, 2011.

(47) Koch, W.; Holthausen, M. C., *A Chemist's Guide to Density Functional Theory*; Wiley: 2001.

(48) Sholl, D. S.; Steckel, J. A., *Density Functional Theory: A Practical Introduction*, Second edition; Wiley: Hoboken, NJ, 2023.

(49) Gilbert, T. L. *Phys. Rev. B* **1975**, *12*, 2111–2120.

(50) Lewars, E. G., *Computational Chemistry: Introduction to the Theory and Applications of Molecular and Quantum Mechanics*; SpringerLink Bücher; Springer Science+Business Media B.V: Dordrecht, 2011.

(51) Smalley, R. E. *Laser Chem.* **1983**, *2*, 167–184.

(52) Heiz, U.; Vanolli, F.; Trento, L.; Schneider, W.-D. *Rev. Sci. Instrum.* **1997**, *68*, 1986–1994.

(53) Masubuchi, T.; Eckhard, J. F.; Lange, K.; Visser, B.; Tschurl, M.; Heiz, U. *Rev. Sci. Instrum.* **2018**, *89*, 023104/1–10.

(54) Habets, A. H. M.; Techinsche Hogeschool Eindhoven *Supersonic Expansion of Argon into Vacuum* **1977**, 1–179.

(55) Lengyel, J.; Levin, N.; Ončák, M.; Jakob, K.; Tschurl, M.; Heiz, U. *Chem. Eur. J.* **2023**, *29*, e202203259.

(56) Liebl, H., *Applied Charged Particle Optics*; Springer Berlin / Heidelberg: Berlin, Heidelberg, 2008.

(57) Heddle, D. W. O., *Electrostatic Lens Systems*, 2nd ed.; Institute of Physics Publishing: Bristol, 2000.

(58) Aberth, W. H.; Schnitzer, R.; Engesser, F. C. *Rev. Sci. Instrum.* **1974**, *45*, 1289–1290.

(59) Zeman, H. D. *Rev. Sci. Instrum.* **1977**, *48*, 1079–1085.

(60) Mahaffy, P. R.; Lai, K. *J. Vac. Sci. Technol. A* **1990**, *8*, 3244–3246.

(61) Miller, P. E.; Denton, M. B. *J. Chem. Educ.* **1986**, *63*, 617–623.

(62) Neuwirth, D.; Eckhard, J. F.; Lange, K.; Visser, B.; Wiedemann, M.; Schröter, R.; Tschurl, M.; Heiz, U. *Int. J. Mass Spectrom.* **2015**, *387*, 8–15.

(63) Gerlich, D. In *Adv. Chem. Phys. 2007*, pp 1–176.

(64) Goebbert, D. J.; Meijer, G.; Asmis, K. R.; Iguchi, T.; Watanabe, K. In *AIP Conf. Proc.* AIP: 2009, pp 22–29.

(65) Westergren, J.; Grönbeck, H.; Kim, S.-G.; Tománek, D. *J. Chem. Phys.* **1997**, *107*, 3071–3079.

(66) Wiley, W. C.; McLaren, I. H. *Rev. Sci. Instrum.* **1955**, *26*, 1150–1157.

(67) Boesl, U. *Mass Spectrom. Rev.* **2017**, *36*, 86–109.

(68) Boesl, U.; Weinkauf, R.; Schlag, E. W. *Int. J. Mass Spectrom.* **1992**, *112*, 121–166.

(69) Chassela, O. B.; Grigoreiv, A.; Fedorov, A.; André, N.; Le-Comte, E.; Rouzaud, J.; Spezzigu, P. *ICSO* **2018**, *2018*, 1118030/1–7.

(70) Tao, J.; Perdew, J. P.; Staroverov, V. N.; Scuseria, G. E. *Phys. Rev. Lett.* **2003**, *91*, 146401/1–4.

(71) Weigend, F.; Ahlrichs, R. *Phys. Chem. Chem. Phys.* **2005**, *7*, 3297–3305.

(72) Grimme, S.; Antony, J.; Ehrlich, S.; Krieg, H. *J. Chem. Phys.* **2010**, *132*, 154104/1–7.

(73) Eichkorn, K.; Weigend, F.; Treutler, O.; Ahlrichs, R. *Theor. Chem. Acc.* **1997**, *97*, 119–124.

(74) Wang, J. X.; Lunsford, J. H. *J. Phys. Chem.* **1986**, *90*, 5883–5887.

(75) Feyel, S.; Döbler, J.; Schröder, D.; Sauer, J.; Schwarz, H. *Angew. Chem., Int. Ed.* **2006**, 4681–4685.

(76) Dietl, N.; Schlangen, M.; Schwarz, H. *Angew. Chem., Int. Ed.* **2012**, *51*, 5544–5555.

(77) Weisshaar, J. C. *Acc. Chem. Res.* **1993**, *26*, 213–219.

(78) Li, J.; Zhou, S.; Zhang, J.; Schlangen, M.; Weiske, T.; Usharani, D.; Shaik, S.; Schwarz, H. *J. Am. Chem. Soc.* **2016**, *138*, 7973–7981.

(79) Li, J.; Zhou, S.; Zhang, J.; Schlangen, M.; Usharani, D.; Shaik, S.; Schwarz, H. *J. Am. Chem. Soc.* **2016**, *138*, 11368–11377.

(80) Blomberg, M. R. A.; Siegbahn, P. E. M.; Svensson, M. *J. Am. Chem. Soc.* **1992**, *114*, 6095–6102.

(81) Li, J.; Zhou, S.; Schlangen, M.; Weiske, T.; Schwarz, H. *Angew. Chem.* **2016**, *128*, 13266–13269.

(82) Geng, C.; Li, J.; Weiske, T.; Schlangen, M.; Shaik, S.; Schwarz, H. *J. Am. Chem. Soc.* **2017**, *139*, 1684–1689.

(83) Schwarz, H. *Angew. Chem., Int. Ed.* **2003**, *42*, 4442–4454.

(84) Irikura, K. K.; Beauchamp, J. L. *J. Phys. Chem.* **1991**, 8344–8351.

(85) Irikura, K. K.; Goddard, W. A. *J. Am. Chem. Soc.* **1994**, *116*, 8733–8740.

(86) Buckner, S. W.; MacMahon, T. J.; Byrd, G. D.; Freiser, B. S. *Inorg. Chem.* **1989**, *28*, 3511–3518.

(87) Sändig, N.; Koch, W. *Organometallics* **1997**, *16*, 5244–5251.

(88) Parke, L. G.; Hinton, C. S.; Armentrout, P. B. *J. Phys. Chem. C* **2007**, *111*, 17773–17787.

(89) Zhou, S.; Li, J.; Schlangen, M.; Schwarz, H. *Angew. Chem., Int. Ed.* **2016**, *55*, 7257–7260.

(90) Li, Q.; Liu, Q.-Y.; Zhao, Y.-X.; He, S.-G. *JACS Au* **2024**, *4*, 1824–1832.

(91) Girard, J. W.; Cavataio, G.; Lambert, C. K. *SAE Transactions* **2007**, *116*, 182–186.

(92) Li, Y.; Armor, J. N. *Appl. Catal. B* **1997**, *13*, 131–139.

(93) Dean, A. M.; Hardy, J. E.; Lyon, R. K. *Symp. Combust.* **1982**, *19*, 97–105.

(94) Blagojevic, V.; Lavrov, V. V.; Koyanagi, G. K.; Bohme, D. K. *Int. J. Mass Spectrom.* **2019**, *435*, 181–187.

(95) Koyanagi, G. K.; Cheng, P.; Bohme, D. K. *J. Phys. Chem. A* **2010**, *114*, 241–246.

(96) Arakawa, M.; Ando, K.; Fujimoto, S.; Mishra, S.; Patwari, G. N.; Terasaki, A. *Phys. Chem. Chem. Phys.* **2018**, *20*, 13974–13982.

(97) Blagojevic, V.; Lavrov, V. V.; Koyanagi, G. K.; Bohme, D. K. *Int. J. Mass Spectrom.* **2017**, *413*, 81–84.

(98) Kaya, T.; Kobayashi, M.; S., H.; S. H. *Chem. Phys. Let.* **1991**, *186*, 431–435.

(99) Ma, H.; Schneider, W. F. *ACS Catal.* **2019**, *9*, 2407–2414.

(100) Shamiri, A.; Aliabadi, N. *Chem. Eng. J. Adv.* **2021**, *8*, 100177/1–13.

(101) Fries, D. V.; Klein, M. P.; Straßner, A.; Huber, M. E.; Luczak, M.; Wiehn, C.; Niedner-Schatteburg, G. *J. Phys. Chem.* **2023**, *159*, 164303/1–17.

(102) Fries, D. V.; Klein, M. P.; Steiner, A.; Prosenc, M. H.; Niedner-Schatteburg, G. *Phys. Chem. Chem. Phys.* **2021**, *23*, 11345–11354.

(103) Fries, D. V.; Klein, M. P.; Straßner, A.; Huber, M. E.; Niedner-Schatteburg, G. *J. Phys. Chem.* **2023**, *159*, 164306/1–14.

(104) Geng, C.; Li, J.; Weiske, T.; Schwarz, H. *Proc. Natl. Acad. Sci. U.S.A.* **2019**, *116*, 21416–21420.

(105) Geng, C.; Li, J.; Weiske, T.; Schwarz, H. *Proc. Natl. Acad. Sci. U.S.A.* **2018**, *115*, 11680–11687.

(106) Eckhard, J. F.; Neuwirth, D.; Panosetti, C.; Oberhofer, H.; Reuter, K.; Tschurl, M.; Heiz, U. *Phys. Chem. Chem. Phys.* **2017**, *19*, 5985–5993.

(107) Levin, N.; Margraf, J. T.; Lengyel, J.; Reuter, K.; Tschurl, M.; Heiz, U. *Phys. Chem. Chem. Phys.* **2022**, *24*, 2623–2629.

(108) Zhai, H.-J.; Zhang, X.-H.; Chen, W.-J.; Huang, X.; Wang, L.-S. *J. Am. Chem. Soc.* **2011**, *133*, 3085–3094.

(109) Schletti, R.; Wurz, P.; Scherer, S.; Siegmund, O. H. *Rev. Sci. Instrum.* **2001**, *72*, 1634–1639.

(110) Schlögl, R. *Angew. Chem., Int. Ed.* **2015**, *54*, 3465–3520.

(111) Qian, K.; You, R.; Guan, Y.; Wen, W.; Tian, Y.; Pan, Y.; Huang, W. *ACS Catal.* **2020**, *10*, 15142–15148.

(112) Sarkas, H. W.; Arnold, S. T.; Hendricks, J. H.; Kidder, L. H.; Jones, C. A.; Bowen, K. H. *Z. Phys. D* **1993**, *26*, 46–50.

(113) Fairbrother, F., *The Chemistry of Niobium and Tantalum*; SpringerLink Bücher; Elsevier Pub. Co.: 1967.

(114) Cheng, N.; Stambula, S.; Wang, D.; Banis, M. N.; Liu, J.; Riese, A.; Xiao, B.; Li, R.; Sham, T.; Liu, L.; Botton, G. A.; Sun, X. *Nat. Commun.* **2016**, *2018*, 13638/1–9.

(115) Courtois, C.; Eder, M.; Schnabl, K.; Walenta, C. A.; Tschurl, M.; Heiz, U. *Angew. Chem. Int. Ed.* **2019**, *58*, 14255–14259.

Acknowledgments

I would like to express my deepest gratitude to everyone who supported me during the course of my dissertation.
First and foremost, I would like to thank Ueli Heiz for giving me the opportunity to work in such an inspiring research environment. By inviting me to join his chair as a doctoral student, he made my contribution to this project possible.
I am profoundly grateful to my supervisor, Martin Tschurl, for his continuous support, insightful advice, and constructive feedback. He is an exceptional motivator who always helped me to see the positive, even when the work consisted of tasks such as descaling water connections.
Special thanks go to Kevin Bertrang and Tobias Hinke, who originally invited me to the chair to join their project for my Master's thesis. Their trust and encouragement to pursue my own project contributed significantly to my decision to embark on a PhD.
I am also grateful to Dima, who taught me how to perform DFT calculations. He introduced me to the magic of theoretical chemistry and inspired me with his enthusiasm for computational work, never once responding impatiently to my countless questions.
My sincere thanks go to the electrical and mechanical workshop for their exceptional work in manufacturing important components for my experimental setup.
I would also like to thank everyone who took the time to proofread this dissertation and provided feedback. Their contributions have been instrumental in improving the clarity and quality of this work. In addition, I would like to thank my colleagues and fellow researchers at the chair, whose work- and non-work-related discussions have enriched my research. It was always a pleasure to come to the lab, and their company made the research process even more enjoyable. I am confident that the friendships formed during this project will continue outside of it.
Finally, I would like to express my heartfelt gratitude to my family and friends for their unfailing encouragement and understanding during this journey. Their love and support have always been a source of strength to me.

Appendix

Licenses

In this work, two own publications have been presented and discussed as results of this dissertation:

Manuscript 1 [14]:

Authors	Flora Siegele, Martin Tschurl, Detlef Schooss, Ueli Heiz
Title	Activation of CH_4, NH_3, and N_2 by Tantalum Ions, Clusters and Their Oxides: What Can be Learnt from Studies of Ions in the Gas Phase
Journal	ChemPhysChem
DOI	doi.org/10.1002/cphc.202400513

Manuscript 2 [15]:

Authors	Flora Siegele, Jan F. Eckhard, Tsugunoske Masubuchi, George Goddard, Detlef Schooss, Dmitry I. Sharapa, Felix Studt, Martin Tschurl, Ueli Heiz
Title	From C$-$H Bond Insertion to Hydrogen Atom Transfer: Tuning the Reaction Mechanisms of Methane Activation by the Oxidation of Ta_2^+
Journal	Chemistry - A European Journal
DOI	doi.org/10.1002/chem.202500545

Technical Drawings

Technical drawings of the newly installed components are given on the following pages.

***Faraday* Cup (85):** The flange, rods and the *Faraday* cup itself are made of stainless steel. All modification of bought products was done by the in-house mechanical workshop. Ceramic components are used for electrical insulation. An electrical connection between the bayonet plug-in connector and the *Faraday* cup is achieved using capton insulated copper wire with 2 mm diameter.

MCP Detector (86): The flange and rods are made of stainless steel. All modification of bought products was done by the in-house mechanical workshop. The MCP plates are mounted onto a ceramic plate. Electrical connections between the anode and the bayonet plug-in connector, as well as between MCP_in and the bayonet plug-in connector are achieved using capton insulated copper wires with 3 mm diameter.

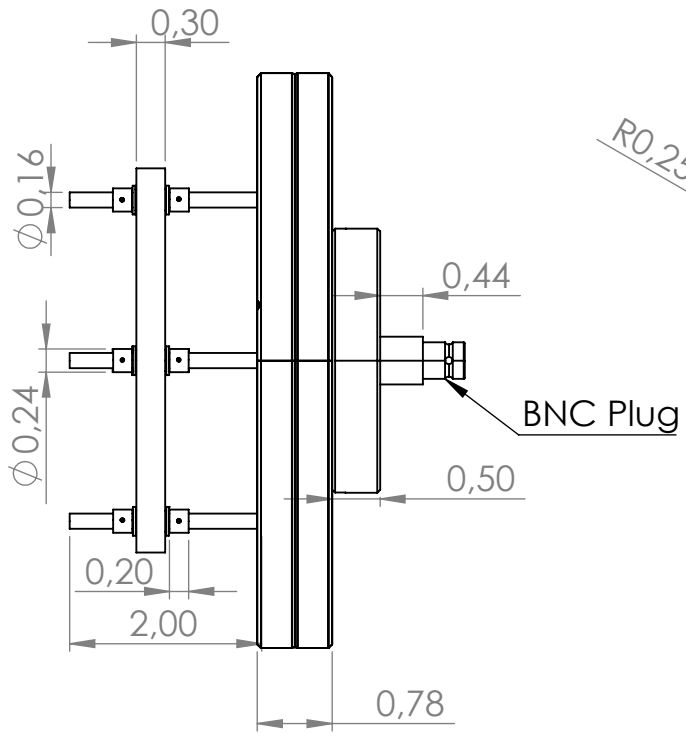

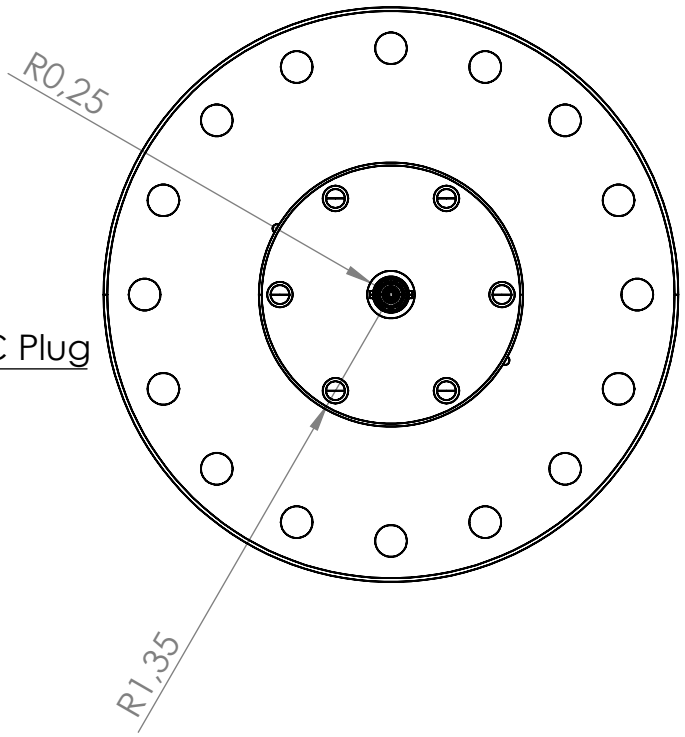

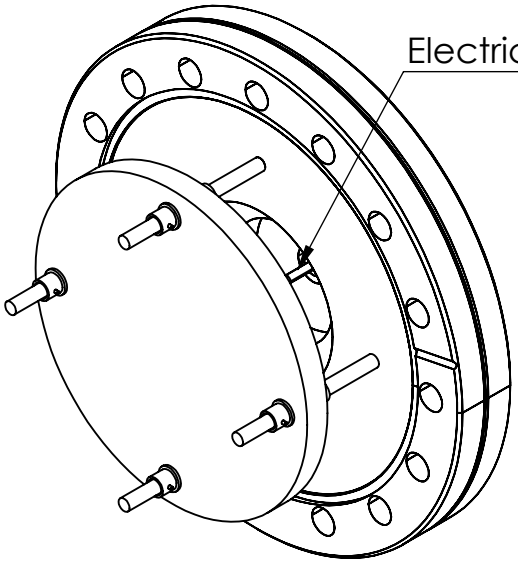

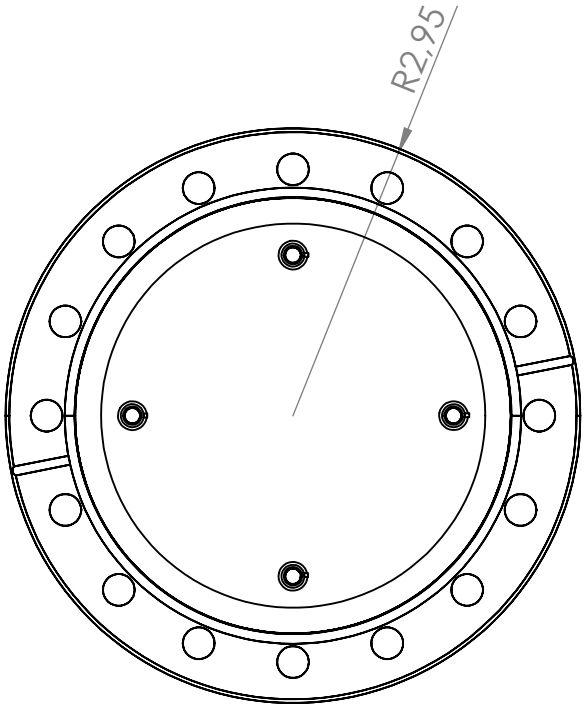

Material:	Name:	
Stainless Steel	Faraday Cup	A4
	Scale: 1:2	

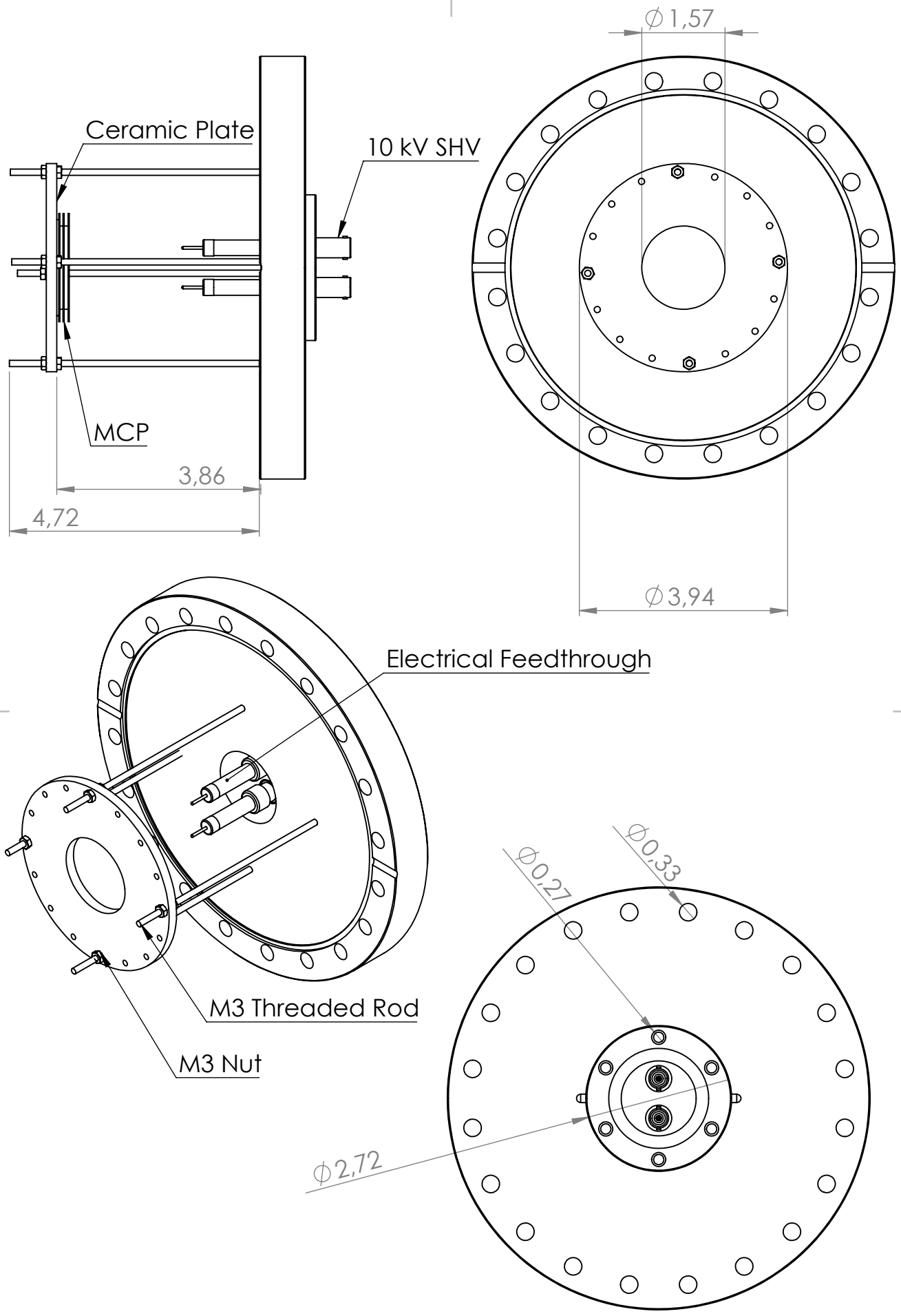

Material:	Name:	
Stainless Steel	MCP on Flange	A4
	Scale: 1:2.5	BLATT 1 VON 1